University of
Strathclyde
Engineering

Novel Diode Laser Absorption Techniques for Combustion Diagnostics

Gordon S. Humphries

Department of Electronic and Electrical Engineering

Centre for Microsystems & Photonics

and

Department of Chemical and Process Engineering

A thesis submitted to the Department of Electronic and Electrical Engineering
at the University of Strathclyde for the degree of Doctor of Philosophy

February 2017

Declaration of Authenticity & Author's rights

This thesis is the result of the author's original research. It has been composed by the author and has not been previously submitted for examination which has led to the award of a degree.

Signed:

Date:

Abstract

In-situ optical techniques offer one of the most attractive options for measuring species concentration and spatial distribution profiles in reacting environments, such as flames. The generally non-intrusive nature and spatial resolution of these techniques are now preferred over on extractive sampling, followed by analysis using techniques such as gas chromatography. In this thesis two laser absorption measurement techniques are applied to measure the soot distribution, and acetylene concentration profiles in a flat-flame burner.

The in-situ measurement of the distribution of particulate matter in flames is a key step in understanding the mechanism of its formation. Most in-situ measurement systems for this purpose are based on laser induced incandescence where particles are heated using high power laser sources and the increased incandescence emission of the soot particles is detected. However as the soot cools by heat transfer to the surrounding gas, following laser heating, the pressure of the gas is increased creating an acoustic effect. Photoacoustic detection has been applied to quantify low concentrations of particulate matter in ambient air but there have been few applications of photoacoustic detection to the in-situ measurement of particulate matter formation in combustion processes. A novel simple approach using a modulated continuous wave diode laser is presented in this thesis. The measurements taken using this new technique are compared to measurements of the visible emission from the flame, and previous soot distribution measurements using laser induced incandescence.

Absorption spectroscopy using near-infrared tunable diode lasers has been applied to measure species in several harsh environments such as aero-engine exhaust plumes, flames, and other industrial processes. Simple single pass absorption techniques are not always suitable for this purpose due to the low absorption of the target species, either due to low concentration or weak absorption line-strength at high temperatures.

One method to increase the sensitivity of such techniques is by using cavity enhanced methods which increase the effective path length of the laser through the absorbing medium. One such cavity enhanced method is Cavity Ring-Down Spectroscopy (CRDS). CRDS uses a cavity constructed of highly reflecting mirrors, laser light is then coupled into this cavity and absorption measurements can be evaluated from the decay rate of light from the cavity. The design and, novel application of continuous wave CRDS to measure the concentration profile of acetylene in the flat-flame burner is presented. Difficulties in deriving an absolute acetylene concentration from the measured ring-down times were encountered due to the large number of interfering features. Serveral fitting and extraction techniques are applied and compared to attempt to overcome these difficulties.

Table of Contents

Declaration of Authenticity **i**

Abstract **ii**

Table of Contents **iv**

1 Introduction **1**

1.1 Motivation 1
1.2 Soot Formation 2
1.3 Combustion Diagnostics Overview 5
  1.3.1 Ex-Situ Techniques 5
  1.3.2 In-Situ Techniques 6
1.4 Laser Diagnostic Techniques 7
  1.4.1 Laser Absorption Measurements 7
  1.4.2 Laser Induced Fluorescence 8
  1.4.3 Laser Induced Incandescence 8
  1.4.4 CARS Spectrometry 9
1.5 Thesis Aims and Objectives 9
1.6 Thesis Overview 9

2 Principles of Diode Laser Spectroscopy **11**

2.1 Introduction 11
2.2 Molecular Spectroscopy 12
2.3 Absorption Spectra 15
2.4 Modelling Spectral Absorption Features 16
  2.4.1 The HITRAN and HITEMP Databases 17
  2.4.2 Spectral Line Intensity 17
  2.4.3 Spectral Broadening 18
  2.4.4 The Voigt Profile 20
  2.4.5 Concentration 22
2.5 Model of Expected Flame Spectrum 24
2.6 Cavity Enhanced Absorption spectroscopy 25
  2.6.1 Cavity Ring-Down Spectroscopy 25
  2.6.2 Phase-Shift CRDS 26
  2.6.3 Integrated Cavity Output Spectroscopy 26
  2.6.4 Off-Axis Cavity Enhanced Absorption Spectroscopy 26

2.7 Summary 27

3 Porous-Plug Burner Overview and Soot Distribution Measurements 28

3.1 Introduction 28
3.2 Burner Design 30
3.3 RGB Image Analysis of Flame Emission 33
  3.3.1 Comparison to Laser Induced Incandescence (LII) 40
3.4 Measurement of Soot Distribution by the Photoacoustic Effect 42
  3.4.1 Experimental set-up for photoacoustic soot measurement 43
  3.4.2 Comparison of photoacoustic and LII soot measurements. 46
  3.4.3 Calibration of acoustic signal 48
  3.4.4 Review of the photoacoustic measurement technique 51
3.5 Temperature estimation using laser induced fluoresce of OH 52
3.6 Summary 53

4 Continuous-Wave Cavity Ring Down Spectrometer Design 54

4.1 Introduction 54
4.2 Cavity Ring-Down Spectroscopy Theory 55
4.3 Optical Cavity Theory 57
  4.3.1 Frequency Response of Optical Cavities 57
  4.3.2 Cavity Stability 60
  4.3.3 Transverse Electromagnetic Modes 64
  4.3.4 Mode-Matching 67
4.4 Modes of Operation for cw-CRDS 68
  4.4.1 Optical Switches in cw-CRDS 70
4.5 The use of Pulsed versus CW Laser Sources 71
4.6 Initial cw-CRDS Spectrometer Design 72
  4.6.1 Optical Cavity 72
  4.6.2 Laser Source 73
  4.6.3 Mode Matching Optics 74
  4.6.4 Optical Switch and Trigger Electronics 75
  4.6.5 Control and Data Acquisition 76
  4.6.6 Optical Alignment Procedure 78
4.7 Spectrometer Performance Evaluation 79
4.8 Summary 82

5 cw-CRDS Combustion Measurements 84

5.1 Introduction 84
5.2 cw-CRDS Spectrometer Adaptation to In-Situ Flame Measurements . . . 85

5.3 1535 nm Laser Wavelength Characterisation 88
5.3.1 Initial Measurements of The P17e Acetylene Feature 91
5.4 Refinement of Spectrometer Design to Improve In-Situ Flame measurements 92
5.4.1 Semiconductor Optical Amplifier 94
5.4.2 Trigger Electronics 95
5.4.3 Signal Normalisation Using Two Wavelength Approach 96
5.5 Spectrometer Performance Evaluation 99
5.5.1 Cavity Mode Structure 102
5.5.2 Ring-down time vs. Height above burner 105
5.5.3 Initial Equivalence Ration Comparison. 110
5.6 Determination of Absolute Acetylene Concentration Profiles 111
5.6.1 Extraction of Acetylene Spectra 111
5.6.2 Fitting of Model Spectra 117
5.6.3 Acetylene Concentration Profiles 121

6 Conclusions and Further Work 125
6.1 Overall conclusions 125
6.1.1 Project Aims and Objectives 125
6.1.2 Evaluation of Porous-Plug Burner. 126
6.1.3 Development of cw-CRDS Spectrometer 127
6.1.4 cw-CRDS Performance in Laminar Flames 128
6.1.5 Recovery of Acetylene Concentration Profiles 129
6.1.6 Summary of Conclusions 131
6.2 Further Work 131
6.2.1 High Temperature Spectroscopy 131
6.2.2 Application of cw-CRDS to Low Pressure Flames 132
6.2.3 Other Cavity Enhanced Techniques 133
6.2.4 Photoacoustic Soot Detection With Fibre Lasers 134
6.2.5 cw-Laser Induced Incandescence 135

References 136

Publications 144

1 Introduction

1.1 Motivation

Despite the ever increasing prevalence of alternative sources, combustion of hydrocarbon fuels continues to be the most common method of energy generation across a wide range of applications globally, from its use in food preparation, through to large scale electrical power generation. Over the last few decades there has been a strong focus on the detrimental effects to the environment arising from our reliance on combustion which has lead to a strong drive towards the development of a reliable alternative. Whilst these alternative methods of energy generation continue to become more commonplace and economically viable over time, combustion will still remain a key component of our energy generation portfolio for many years to come [1], and therefore there is a pressing need to increase the efficiency of existing combustion systems in order to reduce the quantity of environmentally harmful emissions. A key step towards this goal is to develop a better understanding of fundamental combustion processes and the complex chemical mechanisms that contribute to the formation of pollutants, particularly when fuels undergo incomplete combustion, which can lead to the formation of impure carbon particulate pollutants, commonly known as soot [2].

The emission of particulate soot from combustion is thought to be one of the largest human-related contributions towards global climate change. Recently research efforts [3] have highlighted the absorption of solar radiation by soot particles as the primary mechanism by which soot contributes to global warming. It is by this mechanism that soot can also increase the melt-rate of ice in the polar regions by changing the albedo of the snow cover [4]. Soot, when inhaled, also poses a major risk to public heath as it is a known carcinogen and can be a contributory cause in the development of heart disease respiratory illnesses such as asthma and bronchitis.

From a purely environmental and health protection standpoint, the assumption could be made that combustion processes should be designed in such a way that the emission of soot is minimised (e.g. by moving towards complete combustion conditions). However, there are a variety of situations, such as furnaces, where the production of soot is beneficial as the radiative heat transfer from the particulate matter can increase the efficiency of the process, but emission of soot is not desirable, and therefore should be oxidised downstream. Other processes can also be designed to produce soot as an end product which can be used as a feed stock for other processes [5].

The mechanism by which soot particles are formed during combustion is highly complex comprising of a number of intermediate species. Significant research effort [6–8] has been devoted to the development of models for soot formation. This has highlighted a need for accurate measurement of the concentration profiles of intermediate species in simple flame geometries where combustion conditions can be well controlled, to allow for validation of the model mechanisms [9]. Acetylene, as will be discussed in section 1.2, is a key intermediate in the formation and growth of poly-aromatic hydrocarbons, and particulate soot. Due to the important role of acetylene a number of different measurement techniques have been applied to overcome the harsh conditions of the combustion enviroment, and gain accurate concentration profile data [10–13].

1.2 Soot Formation

It is not within the scope of this project to present and validate each of the different reaction pathways which comprise the full soot formation process, instead this section will provide an overview of the process highlighting a number of key species of interest for measurement. In any case, soot by its nature does not have a standard composition or structure and therefore the true formation mechanism will be unique to each individual combustion system [14].

During the early stages of the formation process the hydrocarbon fuel is broken down

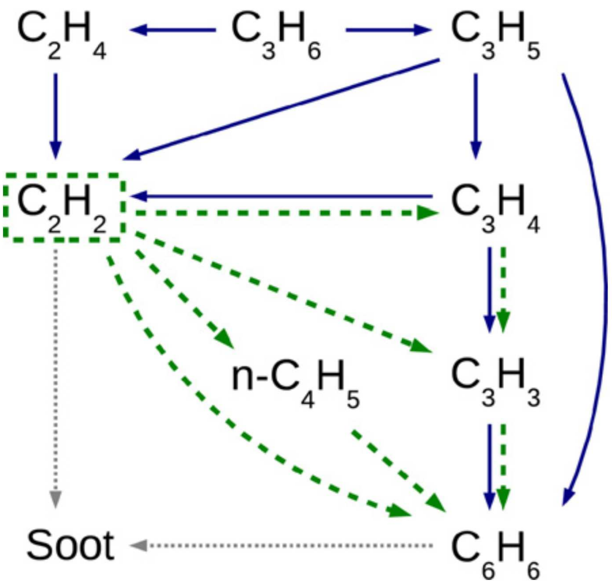

Figure 1.1: Proposed reaction pathway for initial aromatic ring formation, image reproduced from [7]

into a number of smaller molecules and several radicals. Under the correct conditions these small molecules further react and form larger molecules, eventually forming larger molecules containing a number of aromatic rings. These are collectively known as poly-aromatic hydrocarbons (PAHs). Through further reaction the PAHs begin to combine to become progressively larger, eventually forming together to become nascent soot particles [8].

Following the initial pyrolytic breakdown of the hydrocarbon fuel one of the first species to be formed is acetylene (C_2H_2) which has a key role in the formation of the first aromatic ring. Figure 1.1 shows an overview of one of the main reaction pathways thought to lead to the formation of this first ring [7], though it is important to note that there is a large number of competing reaction pathways by which this can be achieved. One such pathway is the formation of propargyl (C_3H_3) from the reaction of acetylene with the singlet methylene radical ($^1CH_2$), which then further reacts to form benzene [14].

Following its role in the formation of the first aromatic ring, it is largely accepted that acetylene continues to play a major role in the growth of the PAHs through the hydrogen abstraction/carbon addition (HACA) mechanism proposed by Frenklach et al in 1985 [15], which has formed the basis for many further soot formation models. The continuing process of acetylene addition produces species comprising of a sequentially larger number of aromatic rings. Eventually, once the PAH molecules become sufficiently large it is possible for growth to continue either by reaction with other PAH molecules or by reaction with radicals remaining from the original pyrolytic breakdown. The geometry of the PAH molecules limits growth by the HACA mechanism to a planar dimension and therefore there must be a nucleation step, allowing the PAHs to combine to form a three dimensional structure, and eventually form nascent soot particles. Numerous conflicting mechanisms have been postulated for this mechanism, with the majority of these based around the coalescence of the PAH molecules into stacked clusters followed by cross-linking into three dimensional structures. An excellent review of the formation of nascent soot was provided by Wang in 2011 [8], which highlighted several knowledge gaps.

The nascent phase of soot formation encompasses the transition from the gaseous PAH molecules to solid particles and, despite significant recent research efforts, still remains as one of the most poorly understood areas of the formation process and is therefore an area of interest for measurement. Interestingly, the optical properties of nascent soot are different from mature soot or PAHs, notably that the particles appear ‘Transparent’ [16] in the visible. It has been proposed that the particles take on a quasi-liquid like structure, and therefore posses different properties than solid particles or gaseous molecules [17]. These differences have curtailed the optical measurement of nascent soot and therefore much of the study of the nascent phase has been undertaken using extractive measurement techniques coupled with electron microscopy [18–20]. However, such methods are not always suitable, or possible in some combustion systems, and therefore there has been an effort to develop optical techniques for the quantification of nascent soot.

After nucleation the nascent particles continue to grow either through coagulation with other soot particles, or through surface growth by further reaction with PAHs [21, 22]. Although the contribution of surface reaction to the growth of the particle begins to diminish as the soot becomes more mature. As the maturation of the particles progresses the optical properties shift to that of a solid material [16], absorbing across a broad range of wavelengths, enabling a range of optical measurement techniques to be used for its quantification.

1.3 Combustion Diagnostics Overview

The complexity of the soot formation process and the high number of intermediate species has resulted in the development of a wide range of measurement techniques [23–27], each targeted at measuring either a single, or small range of species. The volume of published literature available highlights the difficulties encountered taking measurements in the harsh combustion environment. These techniques can be split into two categories [28]:

- *Ex-situ* techniques first require the extraction of a sample from the combustion system, normally using a probe, before analysing the sample at a later point.
- *In-situ* techniques analyse the species or characteristic of interest within the combustion system. This is normally achieved using optical measurement techniques.

There has been considerable debate over the advantages and disadvantages of each approach, and therefore the validity of the measurements obtained.

1.3.1 Ex-Situ Techniques

Historically ex-situ techniques have been attractive as this approach allows existing high accuracy analytical methods to be undertaken on the sample extracted from the combustion process without significant modification to the analytical process or equipment. Many of these techniques are well established in other fields and can provide much higher sensitivities and/or measure a much wider range of species than is currently achievable using an in-situ measurement approach. Some of these techniques are so commonly used in analytical chemistry that commercially produced instruments are available. However, the ex-situ approach does have several disadvantages which can lead to difficulties in the interpretation of the measurements.

The extraction procedure required for ex-situ measurements is the main source of error for these measurements, as it is critical that the extractive sample be representative of the conditions at the measurement position. This can be particularly problematic for reacting systems such as flames as the extraction procedure must ensure that the reaction is suspended during sampling, which can limit probe sampling to stable species. A further disadvantage to extractive sampling techniques is that the presence of a sample probe can disturb the structure and composition of the flame [29]. This can be due to a change in the flow-field within the flame or due to cooling of the flame by the sampling probe [28].

1.3.2 In-Situ Techniques

Due to the shortcomings of ex-situ measurements there has been a drive towards making more measurements using the in-situ approach which is generally less invasive. These measurements are generally undertaken using an optical measurement techniques measuring absorption, scattering, or emission.

It is a misconception however to assume that all optical techniques cause no perturbation to the combustion process. When the incident laser light is strongly attenuated by absorption, most notably by particulate, energy transfer can lead to heating and thermal perturbation of the flame [30]. This is particularly prevalent when the measurement technique calls for the use of high power continuous wave lasers.

1.4 Laser Diagnostic Techniques

A wide array of laser based optical diagnostic techniques have been developed since the invention of the laser in 1960 for a wide range of applications including: Aero-engine emissions [31], environmental studies [32], process control [33], and bio-medical applications [34]. This section will give a brief overview of some of the more common approaches used for combustion measurements.

1.4.1 Laser Absorption Measurements

Laser absorption operates by measuring the attenuation of a probe laser over a given path. Measurements can either made at a single wavelength [35] or, if a tunable laser source is used, a scan over a wavelength range to produce spectrally resolved absorption measurements [24], commonly known as spectroscopy. Many molecules exhibit strong absorption in the mid infra-red (MIR) spectral region, as the laser wavelength becomes resonant with the fundamental rotational and vibrational transitions of the the molecule. However, weaker overtones of these transitions can be probed in the near infra-red (NIR) region [36]. Although not described in this work spectroscopy can also be performed using a broadband optical source and spectrally resolved detection, in place of the swept wavelength approach [37].

One strategy which can be used to increase the sensitivity of laser absorption measurements is increasing the laser-gas iteration length by having multiple passes through the gas. This can be achieved by enclosing the measurement volume in an optical cavity bounded by two high reflectivity mirrors, into which the laser light is coupled. One such cavity based technique which has be used to make sensitive in-situ flame measurements is cavity ring-down spectroscopy (CRDS) [38] where pulsed laser sources are used to inject light into the cavity and absorption measurements are made from the changing cavity lifetime. CRDS measurements can also be made using continuous-wave laser sources [39], using optical resonance to couple light into the cavity. However, despite the advantages to this technique (discussed in detail in chapter 4 little progress has been made towards its use for in-situ flame measurements.

A further technique that can be used to increase the sensitivity of laser absorption measurements is photoacoustic detection. By probing absorption using an intensity modulated laser source the absorbing species, or particle is periodically heated. As the species cools to the surrounding bulk gas an acoustic wave is generated, the magnitude of which can be detected using a suitable microphone or transducer.

1.4.2 Laser Induced Fluorescence

Laser Induced Fluorescence (LIF) [40] is a further spectroscopic technique in which absorption of a probe laser source excites a molecule or atom to a higher energy level. Measurements are then undertaken as the excited species returns to a lower energy level by the emission of light. The emitted light is at a longer wavelength then the excitation light which allows the emitted light to be easily measured using collection optics and a photo detector with a suitable filter. With the use of appropriate optics the LIF technique can be used to make spatiality resolved or imaging measurements in flames and has been employed for thermometry [41, 42], and to measure a range of species, including OH and PAHs [43–45].

1.4.3 Laser Induced Incandescence

Laser Induced Incandescence (LII) is a technique which is employed to measure particulate matter in flames (i.e. soot). During a standard LII measurement a high power, short duration laser pulse is used to rapidly heat soot particles to a temperature close to the point of sublimation (≈ 4000/,K) producing increased Planck emission from the particles. This increased emission can be detected using similar collection optics to the LIF technique. Over the last 20 years LII has emerged as a promising tool for the in-situ measurement of soot in combustion systems [46].

1.4.4 CARS Spectrometry

The Coherent anti-Stokes Raman Spectroscopy (CARS) is a non linear optical technique which has found use as a method to measure the bulk gas temperature in flames [47]. Three laser beams are required to generate a CARS signal, the first two beams are known as pump Stokes beams, the third as the probe beam. When the frequency difference between the pump and Stokes beams is equal to the ro-vibrational Raman resonance of the species of interest a further coherent beam is generated. CARS spectra can be measured by changing the wavelength of the probe laser and the bulk gas temperature can be inferred from the relative intensities of the Raman resonances.

1.5 Thesis Aims and Objectives

The overriding aim of this project was to develop a continuous-wave cavity ring-down spectroscopy based measurement technique capable of the in-situ measurement of the vertical concentration profile of acetylene in a one-dimensional, laminar porous-plug burner. To achieve this aim there are several specific objectives: First an evaluation of the thermo-optic effects present in the porous-plug burner which may inhibit the use of the cw-CRDS technique. Secondly, to design and test a cw-CRDS spectrometer which is sufficiently robust to operate in-situ in the harsh flame environment. Thirdly, to apply cw-CRDS to recover the absorption spectrum of a suitable acetylene absorption feature. Finally, to apply existing spectral modelling techniques to such spectra to determine the vertical concentration profile.

1.6 Thesis Overview

This introductory chapter has provided an overview of the need to study the formation of poly-aromatic hydrocarbons, and hence the formation of particulate soot under carefully controlled experimental conditions. Acetylene has been identified as a key species in several steps of the formation process and therefore the development of a technique for its accurate in-situ measurement was chosen as the primary aim of this work. Chapter 2 provides the required background and theoretical knowledge used to infer concentration from infra-red absorption spectra, highlighting the challenges encountered by measuring acetylene at combustion temperatures. Also presented in chapter 2 is a review of a range of highly sensitive techniques for measuring optical absorption with a view to undertaking such measurements. Chapter 3 introduces the premixed ethylene-air porous-plug burner in which all measurements in this thesis were undertaken. Chapter 3 includes an evaluation of the optical perturbations which could be detrimental to optical absorption measurements. This evaluation was completed using a combination of emission measurements and a novel photoacoustic based soot measurement technique. Chapter 4 presents the theoretical considerations and the design of a cw-CRDS spectrometer for the measurement of acetylene in the porous plug burner, followed by some initial evaluation measurements. Chapter 5 presents the final design of the cw-CRDS spectrometer, and the interpretation of the acquired absorption spectra, from which acetylene concentration profiles are obtained. Finally, chapter 6 summarises the conclusions of the thesis and provides some suggestions for the direction of further work.

2 Principles of Diode Laser Spectroscopy

2.1 Introduction

During a standard laser absorption experiment the monochromatic light from the laser source, intensity, I_0 is passed through the absorbing media, and the intensity of the output light I is measured using a photo-detector. When making absorption measurements it is necessary to have either a measurement or estimation of the transmission signal in absence of the absorbing media, which will allow the measurement to be normalised. Mathematically, the attenuation of light through an absorbing medium is described using the Beer-Lambert law [36].

$$\frac{I}{I_0} = \exp\left(-Ad\right) \tag{2.1}$$

where A is the absorbance of the medium per unit length, and d is the path-length of the laser energy through the medium. Consider the case where the attenuation through the medium is due to the presence the molecular absorption of a single species. The absorbance is therefore a function of the mole fraction, temperature, and pressure of the species, integrated along the measurement path-length, as well as characteristic spectroscopic parameters. Therefore if there is sufficient knowledge of these parameters, the measurement path-length, and other transmission losses not due to the species of interest, species concentration measurements can be made using laser absorption. This work will focus, primarily on concentration measurements made by probing molecular absorption transitions in the near infra-red region.

2.2 Molecular Spectroscopy

Molecular spectroscopy is the study of the absorption of light by molecules, typically in the gas or liquid phase. There is an associated change in the internal energy of a molecule following the absorption or emission of electromagnetic energy. In atomic spectroscopy every absorption transition is due to changes to the configuration of electrons. In the more complex case of molecules, additional energy states exist which correspond to vibrations and rotations. Therefore, the absorption spectra of molecules are more complex than pure atomic spectra and can contain useful information on the molecular structure. Each of the mechanisms responsible for these changes requires a different amount of energy, and will hence correspond to a different part of the electromagnetic spectrum. According to Planck's law for the quantisation of energy, the energy required to change the internal energy of a molecule by a discrete amount, ΔE is given by

$$\Delta E = h\nu \tag{2.2}$$

where h is Planck's constant and ν is the frequency of the light being emitted/absorbed.

In this work focus is given to absorption transitions arising from molecular vibrations and rotations, which are located in the infra-red region (1-100μm). At a particular energy state the whole molecule can undergo rotation, and the atoms within the molecule can vibrate relative to one another. For an allowed transition to be observed in the infra-red region there must be a change to the dipole moment of the molecule. If we consider the vibrating atoms within the molecule as an-harmonic oscillators the relationship between potential energy with internuclear distance r can be modelled according to the Morse function,

$$E = E_d \left(1 - \exp\left[-\alpha\left(r - r_{eq}\right)\right]\right)^2 \tag{2.3}$$

where E_d is the bond dissociation energy, α is a molecular constant relating to the width of the energy well around the equilibrium distance r_{eq}. Solving the Schrödinger equation using this function shows that the molecule will have discrete energy levels with eigenvalues [36]:

$$E_{vibrational} = \left\{1 - \chi_e \left(\nu + \frac{1}{2}\right)\right\} \left(\nu + \frac{1}{2}\right) h\omega_e \tag{2.4}$$

where χ_e is the an-harmonicity constant, ω_e is the vibration frequency, and ν is the vibrational quantum number [48] which has specific selection rules which govern the allowable transitions between vibrational energy states according to:

$$\Delta\nu = \pm 1, \pm 2, \pm 3... \tag{2.5}$$

The relative energy required to transition between energy states is related to the population of the initial state according to the Boltzmann distribution. The fundamental transitions between $\nu = 0 \rightarrow \nu = 1$ exhibit absorption in the mid-infrared region (3–8μm) whilst the first transitions $\nu = 0 \rightarrow \nu = 2$ exhibit weaker absorption in the near-infrared region (0.74–3μm). At elevated temperatures the population of the $\nu = 1$ state increases according to the Botlzmann distribution, and therefore absorption corresponding to transitions originating from the $\nu = 1$ state increase in strength.

The number of degrees of vibrational freedom increases with the number of atoms, and is dependent on the molecular structure (linear or non-linear). Acetylene (C_2H_2), which is the target species for this work has a linear structure. A linear molecule will have $3N - 5$ degrees of freedom, where N is the number of atoms in the molecule [36]. Therefore acetylene has 7 degrees of vibrational freedom. The symmetrical H–C≡C–H structure of acetylene means that two of these vibrational degrees of freedom have the same energy as other modes and are therefore degenerate [49], hence acetylene has 5 fundamental vibrational energy states which are shown in table 2.1. Depending on how the vibration changes the shape of the molecule the vibration can be described as asymmetric or symmetric and either a bend or a stretch.

Until this point consideration has only been given to molecular vibrations. Whilst undergoing vibration molecule will also be rotating. The timescale for such rotational

Mode	Description	Normal Mode
ν_1	Symmetric C-H stretch	$\overleftarrow{\text{H - }}\ \text{C} \equiv \text{C}\ \overrightarrow{\text{ - H}}$
ν_2	Symmetric C-C stretch	$\overleftarrow{\text{H - C}} \equiv \overrightarrow{\text{C - H}}$
ν_3	Asymmetric C-H stretch	$\overleftarrow{\text{H - }}\ \text{C} \equiv \text{C-}\overleftarrow{\text{H}}$
ν_4	Symmetric bend	$\uparrow \text{H -} \downarrow \text{C} \equiv \text{C} \uparrow \text{- H} \downarrow$ $\text{H}^{+}\text{ - C}^{-} \equiv \text{C}^{+}\text{- H}^{-}$
ν_5	Asymmetric bend	$\uparrow \text{H -} \downarrow \text{C} \equiv \text{C} \downarrow \text{- H} \uparrow$ $\text{H}^{+}\text{ - C}^{-} \equiv \text{C}^{-}\text{- H}^{+}$

Table 2.1: Fundamental vibrational modes of acetylene. ‘+’ & ‘−’ superscripts denote movement out of and and into the page respectively. [36]

motion is significantly slower than vibration. This allows for the energy structure of vibrations and rotations to be handled separately so that $E_{total} = E_{vibrational} + E_{rotational}$. Assuming the bonds between the atoms can be regarded as rigid, the energy for a rotational energy level can be according to [50]:

$$E_{rotational} = \frac{h^2}{8\pi^2 I} J\left(J+1\right) \tag{2.6}$$

where J is the rotational quantum number, and I is the moment of inertia for the rotation. For a linear polyatomic molecule such as acetylene the average moment of inertia, for rotation in all axis is

$$\sum_i m_i r_i^2 \tag{2.7}$$

where m_i is atomic mass, and r_i is the distance of the molecule's centre of mass for the i^{th} nucleus. For a rigid rotor the selection rules dictate the allowed transitions between rotational energy states to be:

$$\Delta J = 0, \pm 1 \tag{2.8}$$

The absorption features corresponding to each of the three allowed rotational states, $\Delta J = -1, 0, 1$ are denoted using P, Q, and R respectively. All absorption measurements reported in this thesis were targeted at the overtone of the P band of acetylene.

2.3 Absorption Spectra

Our consideration of absorption features until this point has been considered the transitions between energy states, and therefore considering the spectral width of each feature to be infinitely narrow, with absorption only taking place precisely at the defined wavelength for each transition. However in reality, this is not the case and the shape of each feature will follow a wider transmission function due to phenomena such as spectral broadening (discussed below). The Beer-Lambert law (equation 2.1) can be modified to include an absorption parameter $k(\nu)$ [50].

$$\frac{I}{I_0} = \exp\big(k(\nu)P_T\chi_j d\big) \tag{2.9}$$

where χ_j is the mole fraction of the absorbing species j, and P_T is the total pressure. The absorption parameter is defined using the temperature dependent line strength $S(T)$, which is defined in section 2.4.4, and a normalised function $\Phi\left(\nu - \nu_0\right)$ which relates to the line-shape of the absorption feature.

$$k(\nu) = S(T)\Phi\left(\nu - \nu_0\right) \tag{2.10}$$

This modified version of the Beer-Lambert law represents the absolute transmission function for a single absorption transition, which can be recovered experimentally by measuring the absorption (I/I_0) as the wavelength of the laser source is tuned over the transition.

2.4 Modelling Spectral Absorption Features

Following recovery of the absolute transmission function the most effective way to extract physical parameters, such as species concentration is to fit an appropriate theoretical line shape model to the recorded data using a least-squares fit algorithm. Generally, the important physical parameters in such a fit will be concentration, temperature and pressure. Some of these parameters may be known and the fewer unknown parameters included in the model will increase the accuracy and speed of the fitting process. The other parameters needed to model the line shape are spectroscopic parameters, including: line strength and broadening coefficients which can be found in spectroscopic databases, such as HITRAN and HITEMP . The spectroscopic parameters included in these databases are based on a mixture of experimental campaigns and theoretical studies. In some cases the spectroscopic parameters contained in these databases are not accurate and in such cases there may be a need to conduct detailed spectroscopic measurements, under controlled conditions to verify the parameters.

2.4.1 The HITRAN and HITEMP Databases

The HITRAN [51] and HITEMP [52] databases provide spectral parameters for a number of different molecules. HITRAN has been compiled based on its application to measurements undertaken under atmospheric conditions, and therefore several high temperature bands and transitions are not necessarily included. This is particularly relevant to this work as the temperatures encountered during combustion measurements are much higher. The inadequacies of HITRAN at elevated temperatures lead to the establishment of an analogous database HITEMP, which includes transitions that occur at elevated temperatures ($> 1000\,\mathrm{K}$). The 2008 version of the HITRAN database contains parameters for 32 species, and the 2010 version of the HITEMP database contains parameters for 5 species.

The key parameters required to model absorption features using the McLean approximation described in this section are: vacuum wavenumber, line strength, air and self broadened HWHM, temperature dependence coefficient, lower state energy, and air pressure shift.

2.4.2 Spectral Line Intensity

The main contributions that dictate the intensity of a particular spectral feature are: the number of molecules in the lower transition state corresponding to the feature, The concentration of molecules of the absorbing species and the path-length (Cd), and the probability of absorption for the particular feature. The probability that a photon will be absorbed by the transition is dictated by solutions of the quantum mechanical wave-functions for each state in the transition, and the appropriate selection rules.

The intensity of the absorption feature id dependent on the initial population of the energy states. A transition with a highly populated initial state will have a higher intensity than a lower population equivalent state. The relative populations of two different energy states can be calculated according to the Boltzmann distribution:

$$\frac{N_{upper}}{N_{lower}} = \exp\left(\frac{-\Delta E}{kT}\right) \tag{2.11}$$

where N_{upper} and N_{lower} are the population of the upper and lower energy states, ΔE the difference in energy between the two states, T is the temperature, and k is the Boltzmann constant. Recalling equation 2.9, the intensity of the feature will increase dependent on the total number of molecules available for interaction along the path-length [36, 50].

2.4.3 Spectral Broadening

The diode laser measurement techniques used in this work include use relatively low power sources, and as such broadening due to power is considered negligible in this work. Aside from the broadening of features due to un-avoidable factors during measurement the broadening effects that dictate the measured line shape are: natural, Doppler, and collisional broadening [36].

Natural broadening is the most fundamental broadening effect and occurs due to the Heisenberg uncertainty principle which dictates that an energy state with a finite lifetime will have an associated finite energy spread, i.e. $\Delta E \Delta t \geq \hbar$. Natural broadening is homogeneous and has a Lorentzian line shape function. The contribution of natural broadening is generally much smaller than that of Doppler and collisional broadening.

The contribution of collisional broadening is most prevalent under higher pressure conditions. Due to the constant random motion of the molecules they undergo collisions with other molecules, which may or may not cause a change to the energy state. It is assumed that the average time between collisions is much greater than the collision duration. Therefore, the extent of collisional broadening is dependent on the collision rate. Collisional broadening is homogeneous and follows a Lorentzian line shape.

The normalised Lorentzian line shape Φ_L, such that $\int_\nu \Phi_L(\nu - \nu_0)\, d\nu \equiv 1$, is given by [53]:

$$\Phi_L = \frac{1}{\pi} \frac{\Gamma_L/2}{(\nu - \nu_0)^2 + \left(\Gamma_L/2\right)^2} \tag{2.12}$$

Where Γ_L is the Lorentzian FWHM and, for a component species j is given by:

$$\Gamma_L = P_T \sum_j \chi_j \Gamma_j \tag{2.13}$$

This is provided for the component species and for air in the databases. The temperature dependence of the lorentzian broadening parameter is modelled according to:

$$\Gamma_j(T) = \Gamma_j(T_0) \left(\frac{T_0}{T}\right)^n \tag{2.14}$$

n is the temperature dependence coefficient which describes the variation of broadening for each species. and T_0 is the reference temperature for which Γ_j is stated in HITRAN/HITEMP. It is not within the scope of this thesis to measure the broadening parameter for all the possible collision partners present in a combustion system that may have a contribution to the lorentzian FWHM, therefore only the provided self and air broadening parameters supplied in the databases will be used. The peak intensity of the the Lorentzian profile is related to the Lorentzian FWHM according to:

$$\Phi_L(\nu_0) = \frac{2}{\Gamma_L \pi} \tag{2.15}$$

Doppler broadening occurs due to the thermal motion, and associated spread of velocities of the absorbing molecules. This leads to the relative frequency of the incident laser energy to vary for each molecule dependent on its velocity. Molecules travelling towards the laser source will encounter higher frequencies and are said to be 'blue-shifted', whereas those molecules whose velocity is away from the laser source will encounter lower frequencies and are said to be 'red-shifted'. Therefore as the extent of Doppler broadening is dependent on each individual molecule it is inhomogeneous. If the measurement sample is assumed to have a uniform temperature distribution along the measurement path the spread of molecular velocities will follow a Maxwell distribution, and Doppler broadening will have a Gaussian line shape function.

The normalised Gaussian line shape Φ_G such that $\int_\nu \Phi_G\left(\nu - \nu_0\right) d\nu = 1$, is given by **[ref]**:

$$\Phi_G = \frac{2}{\Gamma_G}\sqrt{\frac{\ln 2}{\pi}} \exp\left[-4\ln 2\left(\frac{\nu - \nu_0}{\Gamma_G}\right)^2\right] \tag{2.16}$$

where Γ_G is the Gaussian FWHM calculated according to:

$$\Gamma_G = \nu_0\sqrt{\frac{8kT\ln 2}{mc}} = 7.1625 \times 10^{-7}\,\nu_0\sqrt{\frac{T}{m}} \tag{2.17}$$

where m is the molecular mass and c is the speed of light in a vacuum. The peak intensity of the Gaussian line shape is related to the FWHM according to:

$$\Phi_G(\nu_0) = \frac{2}{\Gamma_G}\sqrt{\frac{\ln 2}{\pi}} \tag{2.18}$$

At low pressures (below 1 atm) the Gaussian contribution of Doppler broadening will be the dominate, due to the deceased number of collisions. At higher pressures the Lorentzian contribution of the collisional broadening will be dominant. At pressures where neither the Doppler nor the collisional broadening are particularly dominant, the line shape will be a convolution of both contributions. The convolution of a Lorentzian and a Gaussian profile is known as the Voigt function.

2.4.4 The Voigt Profile

At pressures around 1 atm the line shape is best modelled using a convolution of the relative Gaussian and Lorentzian contributions known as the Voight profile Φ_V. The

i	A_i	B_i	C_i	D_i
1	-1.215	1.2359	-0.3085	0.021
2	-1.3509	0.3786	0.5906	-1.1858
3	-1.215	-1.2359	-0.3085	-0.021
4	-1.3509	-0.3786	0.5906	1.1858

Table 2.2: Coefficients for numerical approximation of Voigt line shape. [54]

convolution can be given, using the component line shape contributions according to:

$$\Phi_V = \int_{-\infty}^{+\infty} \Phi_G\left(\nu'\right) \Phi_L\left(\nu - \nu'\right) d\nu' \tag{2.19}$$

where ϕ_G and ϕ_L represent the Gaussian and Lorentzian contributions respectively. Most modelling algorithms which are based on the Voigt function make use of numerical approximations, as there is no simple analytical solution to the integral. Several examples of empirical approximations are available and here the algorithm using four generalised Lorentzians, developed by McLean et al. is used [54]:

$$\Phi_V = \frac{2\sqrt{\ln(2)}}{\Gamma_G\sqrt{\pi}} V(X,Y) \tag{2.20}$$

where

$$V(X,Y) = \sum_{i=1}^{4} \frac{C_i\left(Y - A_i\right) + D_i\left(X - B_i\right)}{\left(Y - A_i\right)^2 + \left(X - B_i\right)^2} \tag{2.21}$$

and

$$X = \frac{2\sqrt{\ln(2)}}{\Gamma_G}\left(\nu - \nu_0\right) \quad \text{and} \quad Y = \frac{\Gamma_L\sqrt{\ln(2)}}{\Gamma_G} \tag{2.22}$$

The coefficients for A_i, B_i, C_i and D_i are shown in table 2.2.

The FWHM of the Voigt profile can be estimated by [**ref olivero**]:

$$\Gamma_V = 0.5346\,\Gamma_L + \sqrt{0.2166\,\Gamma_L^2 + \Gamma_G^2} \tag{2.23}$$

The use of McLean's approximation allows for rapid computation of complex absorption spectra containing a high number of absorption features corresponding to several different species, without the need for high performance computational equipment.

2.4.5 Concentration

The main aim of the spectroscopic measurements in this work are the determination of concentration. Therefore it is assumed that there is sufficient knowledge of the temperature and pressure of the species being measured. Assuming the is sufficiently small that the linear regime of the Beer-Lambert law is satisfied concentration is related to the integrated absorbance, α by:

$$\chi_i = \frac{\alpha}{P_T S(T) d} \tag{2.24}$$

where $S(T)$ is the temperature dependent line strength which is given by:

$$\begin{aligned} S(T) = S(T_0)\frac{Q(T_0)}{Q(T)}\left(\frac{T_0}{T}\right)\exp\left[-\frac{hcE''}{k}\left(\frac{1}{T}-\frac{1}{T_0}\right)\right] \\ \times\left[1-\exp\left(\frac{-hc\nu_0}{kT}\right)\right]\left[1-\exp\left(\frac{-hc\nu_0}{kT_0}\right)\right]^{-1} \end{aligned} \tag{2.25}$$

where T_0 isn the standard reference temperature used by HITRAN and HITEMP (296 K), and E'' is the lower state energy of the transition (taken from the database). $Q(T)$ is the molecular partition function, which is also available for acetylene from HITRAN for a wide range of temperatures (70 to 3000 K).

The line intensity contained in the databases S_H has units of $\left[\text{cm}^{-1}/\left(\text{molecule-cm}^{-2}\right)\right]$ which is inconsistent with equation 2.9, where the line intensity has units of $\left[\text{cm}^{-2}/\text{atm}\right]$, therefore a conversion must be applied [31]:

$$S_H N_j = S\chi_j P_T \qquad \left[\text{cm}^{-1}/\left(\text{molecule-cm}^{-2}\right)\right][\text{molecule}] = \left[\text{cm}^{-2}/\text{atm}\right][\text{atm}] \tag{2.26}$$

where N_j is the number of molecules of species j per unit volume:

$$N_j = \chi_j N_A \frac{n_T}{V} \qquad \left[\text{molecule/cm}^3\right] = \left[\text{molecules/mole}\right] \frac{\left[\text{mole}\right]}{\left[\text{cm}^3\right]} \tag{2.27}$$

where n_T is the total number of moles, N_A is Avagadro's constant, and V is volume. A further simplification can be made by applying the ideal gas law to make the conversion a function of temperature.

$$S = S_H \frac{N_A}{RT} = \frac{7.339 \times 10^{21}}{T} S_H \tag{2.28}$$

where R is the gas constant ($82.057\,\text{atm}\,\text{cm}^{-3}\,\text{mol}^{-1}\,\text{K}^{-1}$)

The final transmission function for the model, for a single transition is thus [31]:

$$\frac{I}{I_0} = \exp\left[-P_T \chi_j d \Gamma_G S(T) \sqrt{\frac{\ln 2}{\pi}} V(X,Y)\right] \tag{2.29}$$

This transmission function can be fitted to the experimental data using an unconstrained non-linear fitting process, normally using a least-squared fit function. Again assuming that pressure and temperature are known the fitting process will iterate the calculation of the transmission function until a minimum squares error between the model and the experimental data has been achieved. In this work this was undertaken using the $fminsearch$ function in Matlab.

In most experimental spectra acquired at atmospheric pressure the broadening mechanisms the spectra will have contributions from several closely spaced transitions, which combine to give the final absorption profile. This is particularly apparent in environments, such as combustion, where there are several species with absorption bands that overlap with one another, leading to highly complex spectra. Therefore, it is usually necessary to include all features, corresponding to all species present in the wavelength region of the target absorption feature, in the model.

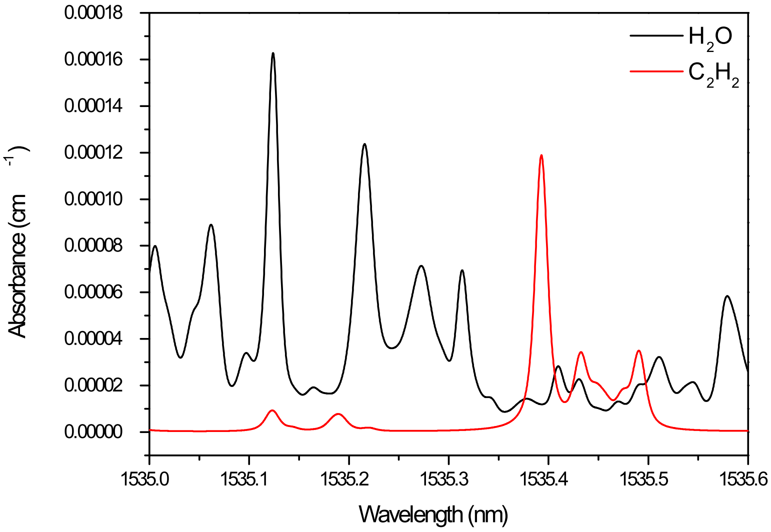

Figure 2.1: Model acetylene and water vapour spectra at expected flame conditions.

2.5 Model of Expected Flame Spectrum

Acetylene has absorption bands the mid-infrared region at 3 μm, and an the near-infrared region at $\approx 1.5\mu$m. Although the fundamental transitions in the mid-infrared exhibit much stronger absorption, this band also contains a high number of interfering strong water vapour transitions [52], which severely limits the suitability of this band for in-situ measurements in a flame. Although the near-infrared absorption band also suffers from water vapour interference there are a few features which should be accessible under combustion conditions. Wagner et al. [24, 55] demonstrated the use of the P17e absorption feature at 1535.4 nm, to make measurements of acetylene in two different burners.

Figure 2.1 shows a model spectra of acetylene using HITRAN 2008, and water using HITEMP 2010, for the conditions expected in the flames supported on the porous-plug burning, which is described in chapter 3. The input parameters for the model are; an acetylene concentration of 1.23%, a water vapour concentration of 4%, a pressure of 1 atm, and a temperature of 1600 K. The model shows that the P17e feature does have some overlap with some weak water vapour features, but is sufficiently isolated and should be a good target for in-situ measurements.

2.6 Cavity Enhanced Absorption spectroscopy

In section 2.3 a number of determinant parameters where described for the intensity of absorption features. One of these parameters was the path-length available for absorption, and therefore an increase in the path-length leads to a increase in the intensity of the recovered transmission profile and hence a corresponding increase in the sensitivity of the instrument. In practical terms it is not always convenient, or possible to have an extended path through the medium. One way to effectively achieve an extremely long path-length is to enclose the measurement volume between two suitably reflective mirrors, passing the laser energy through the absorbing medium multiple times. This is known as cavity enhanced absorption spectroscopy (CEAS), a detailed overview of the theory of coupling light into an optical cavity is presented in chapter 4, in this section a number of different CEAS techniques are briefly described [56].

2.6.1 Cavity Ring-Down Spectroscopy

During a cavity ring-down spectroscopy measurement, light is coupled into the optical cavity using either a pulsed [57] or continuous-wave source [39]. Following either the laser pulse, or attenuation of the input light the rate of decay of the intensity of light in the cavity is measured, this is known as the ring-down time. For an empty cavity the only optical losses present are due to transmission and scattering at the surface of each mirror. When an absorbing species is present in the cavity this will introduce an additional loss, reducing the ring-down time of the cavity. CRDS provides a measurement of absolute extinction and is immune to any shot variations or changes to the laser output intensity [56]. A detailed overview of CRDS using continuous wave lasers (cw-CRDS) is presented later in chapter 4.

2.6.2 Phase-Shift CRDS

Developed in 1980 by Herbelin et al [58], a variant of cw-CRDS is phase-shift CRDS (PS-CRDS). In this method the intensity of a cw source is modulated. As the light passes through the optical cavity the phase of the intensity modulation is shifted with respect to that of the input light. The ring-down time of the cavity can be determined based on a measurement of the change in phase between the light entering and exiting the optical cavity. This can be achieved using a lock-in amplifier [59].

2.6.3 Integrated Cavity Output Spectroscopy

Compared to the two above CEAS techniques, Integrated cavity output spectroscopy (ICOS) [60] is not directly based on a measurement of the cavity lifetime. Instead, the mode structure of the optical cavity is perturbed, normally by mechanical oscillation of the cavity length, and measurements are made of the cavity output integrated over a period of time. ICOS has an advantage over the other CEAS techniques described here as it does not require accurate transverse mode matching of the laser to the cavity to achieve repeatable measurements.

2.6.4 Off-Axis Cavity Enhanced Absorption Spectroscopy

A further variant of the ICOS technique is off-axis cavity enhanced absorption spectroscopy (OA-CEAS) [61]. In an OA-CEAS measurement light is introduced to the optical cavity at a slight angle to the optical axis of the cavity. Because of this deviation the light in the cavity must complete multiple passes back and forth through the absorbing medium before overlapping. The advantage of OA-CEAs is that the relatively long round-trip time within the cavity leads to the output being a quasi-continuum with little to no longitudinal mode structure. A disadvantage of this technique is that the nature of the off-axis alignment leads to a reduction in the spatial resolution of the technique.

2.7 Summary

This chapter has given an overview of the underlying absorption spectroscopy theory upon which the cw-CRDS measurements undertaken in this work are based. Section2.1 described the laser absorption measurement technique in it's simplest form, introducing the Beer-Lambert law to interpret such measurements. In section 2.2 the fundamentals of molecular spectroscopy were introduced. Particular focus was given to the rotational and vibrational transitions of acetylene were discussed. In section 2.4 a technique for modelling absorption features was introduced, which included a description of the mechanisms responsible for the broadening of absorption features, a mathematical model was presented based on the Lorentzian, Gaussian and Voigt line shape functions that allows for rapid computation of the transmission function based on parameters taken from the HITRAN and HITEMP databases, which can also be fitted to experimental measurements of the transmission function to extract concentration informations. Finally section 2.6 Presents a brief introduction to the use of optical cavities to enhance the sensitivity of laser absorption measurements, as well as a brief overview of some of the common cavity based measurement techniques.

3 Porous-Plug Burner Overview and Soot Distribution Measurements

3.1 Introduction

The key experimental component in this research work is the burner, and it is essential that the operation and conditions of the burner are understood. This chapter will present two advances in the understanding of this burner, these advances are made using measurements of visible emission from the flame, and the development of a novel photoacoustic method for measuring soot distribution. Both of these techniques are discussed in detail in sections 3.3 and 3.4 respectively, and the results of both techniques are compared to the more established laser induced incandescence technique.

The complex nature of the combustion process, and in particular incomplete combustion, can substantially increase the number of parameters that must be included in chemical kinetic modelling, requiring a high a computational load to produce accurate predictions. Incomplete combustion mechanisms are composed of numerous intermediate reactions, and several hundred chemical species, and several parameters, such as: temperature and concentration profiles of key species, are either unknown, or are neglected to reduce the computational load. This can lead to significant errors in the calculated output parameters of any particular model [62]. The simplified case of the premixed laminar flat-flame intrinsically limits the problem to a single spatial dimension, which aids in the numerical simulation of the flames. This is in contrast with the more complex case of turbulent flames, where turbulent mixing can lead to flamlets propagating in all dimensions. Therefore measurements taken in this type of burner are often used to validate and improve the understanding of incomplete combustion and refine chemical kinetic models [63].

For a number of years flat-flame burners have been widely employed, as a characterisation standard, for the development of new optical diagnostic techniques for combustion [64, 65]. This is due to the simplifying assumption that a flat-flame is one-dimensional, with conditions, such as species concentration, soot volume fraction, and temperature, varying only with height above the burner (HAB) surface. This simplification implies that there will be little variation of flame conditions in the radial direction, which greatly simplifies the experimental set-up for path-integrated measurement techniques (such as absorption spectroscopy), removing the need to apply a complex tomographic approach to achieve representative measurements [66].

To ensure comparability between research group, a commercially available flat-flame burner manufactured by McKenna Products has found wide use in combustion research. During the 2005 International Sooting Flame Workshop [67] discussions lead to the choice of the McKenna burner as a target flame and a standard set of conditions that should be used. The provision of standard flame conditions allows for meaningful comparison of the research efforts across a number of different groups and institutions.

The McKenna burner is constructed from a cylindrical stainless steel outer housing; within this housing the fuel gases are premixed before flowing through a porous plug manufactured from a sintered matrix of stainless steel. A water cooling coil serves to stabilise the surface temperature of the burner (and hence the boundary condition for the flame). In soot formation studies a cylindrical stabilisation plate manufactured from stainless steel is normally suspended above the burner surface to reduce the effect of disturbances occurring from any ambient air currents to the flame. Section 3.2 describes the flat-flame burner used in this work, highlighting the differences from the more widely used McKenna design.

Figure 3.1: 33 mm diameter porous-plug burner used for measurements (shown supporting a $\phi = 2.22$ flame).

3.2 Burner Design

The burner used for this work is shown in figure 3.1, although it is of a broadly similar design, the porous-plug burner used here differs from the standard McKenna burner as it has a plug diameter of only 33 mm. The stabilisation plate is similarly reduced in diameter from the standard 60 mm to 33 mm and is suspended 21 mm above the surface of the burner. The reduction in the diameter of the stabilisation plate is a significant change, as this will change the rate of heat transfer to the plate from the flame.

To achieve different flame conditions the fuel equivalence ratio ϕ can be varied according to equation 3.1

$$\phi = \frac{\left[\chi_{air}/\chi_{C_2H_4}\right]_{stoich}}{\chi_{air}/\chi_{C_2H_4}} \tag{3.1}$$

where χ is mole fraction and the subscript ‘stoich’ denotes the stoichiometric mole fractions required for complete combustion ($\phi = 1$). A number of flame conditions were used ranging from $\phi = 1.77$ to $\phi = 2.97$, to produce flames that produce little to no soot through to highly sooting flames. This set of flame conditions allows for the determination of the equivalence ratio at which soot formation begins to occur. The

ϕ	$\chi_{C_2H_4}$	χ_{air}	Air Flow-Rate (sl/min)	C_2H_4 (sl/min)
1.77	0.1099	0.8901	0.3445	2.790
1.92	0.1181	0.8819	0.3711	2.770
2.07	0.1262	0.8738	0.3972	2.750
2.22	0.1341	0.8659	0.4229	2.730
2.37	0.1419	0.8581	0.4482	2.710
2.44	0.1458	0.8542	0.4607	2.700
2.59	0.1534	0.8466	0.4855	2.680
2.67	0.1571	0.8429	0.4978	2.670
2.82	0.1646	0.8354	0.5220	2.650
2.97	0.1719	0.8281	0.5459	2.630

Table 3.1: Flow-rates used with porous-plug burner

flow-rates of air and ethylene used to generate these flame conditions are shown in table 3.1.

The flow-rates of air and ethylene (CP-grade) supplied to the burner are controlled using either mass-flow controllers (Cole-Palmer) or using rotameters (Roxspur) which were used for the photoacoustic measurements. Careful consideration was given to the calibration of the rotameter readings as the observed float height would be incorrect if the internal pressure was above atmospheric, due to resistance further down-stream. One potential source of significant pressure drop in the burner set-up could be the porous-plug. The pressure in the delivery line the was measured immediately down-stream of the rotameters confirming that there was no significant increase in pressure above atmospheric caused by the porous-plug. The flow measurement of the rotatmeters was checked using a bubble-flow meter, and through comparison with the mass-flow controller. A discrepancy in the rotatmeter reading for ethylene was identified and a calibration factor was applied based on the value measures using the mass-flow controller and bubble-flow meter, which were in agreement.

The burner used in this work has a further variation from the more commonly used McKenna design as it does not have the capability to use a co-flow shielding gas which. This could potentially have an adverse effect on the stability of the flame. However, precautions were taken to minimise the adverse effect of any errant air currents on the stability of the flame; the use of a extraction system which served to locally direct air currents, careful placement of any equipment which could create a disturbance (e.g. electronic equipment containing cooling fans), and temporary shielding plates placed around the burner.

An inherent feature of this burner is the accumulation of soot particulate upon the stabilisation plate, especially when operating the burner for extended periods of time. For this reason the operating time for high equivalence ratio flames ($\phi > 2.59$) was limited to 30 minutes of operation, before the flame was extinguished for $\approx$ 20 minutes to allow the stabilisation plate to cool down prior to cleaning. This posed a challenge in that the burner required 20 minutes of this running time for temperature stabilisation. A procedure was adopted that a burner was initially operated with a lean flame ($\phi \approx 1.77$) for 20 minutes following ignition as this would allow the stabilisation plate to heat to a temperature close to the flame conditions, with little accumulation of soot on the stabilisation plate. Following this initial preheating period the flow-rates of the combustion gases were reset to the required experimental conditions and the apparatus was left to stabilise for a further 5 minutes before commencing any measurements.

The validity of the flat-flame dimensionality is critical when deciding on the suitability of a particular diagnostic technique, and the accurate interpretation of measurements. The flat-flame assumption was tested by Migliorini et al. [68] for a number of different flat-flame burners constructed using a variety of plug materials, by measuring the radial soot profile of each burner. Some of the burners tested in this work (particularly those with a porous plug manufactured from stainless steel) produced flames which showed significant variations along the radial direction. This investigation highlighted the importance of testing the assumption for individual burners.

By scanning the measurement location horizontally across a single height above the burner a radial profile of soot volume fraction can be produced. Figure 3.2 shows the results of such a scan undertaken on the flat-flame burner by Dunn [69] using laser induced incandescence (LII). The LII technique is a spatially resolved technique, which uses a lens system to take point measurements from a specific location within the flame, and is therefore not influenced by the variation in optical path-length through the flame as the burner is translated. The distribution of soot is constant across the diameter of the flame which indicated that the flat-flame assumption holds true for this burner.

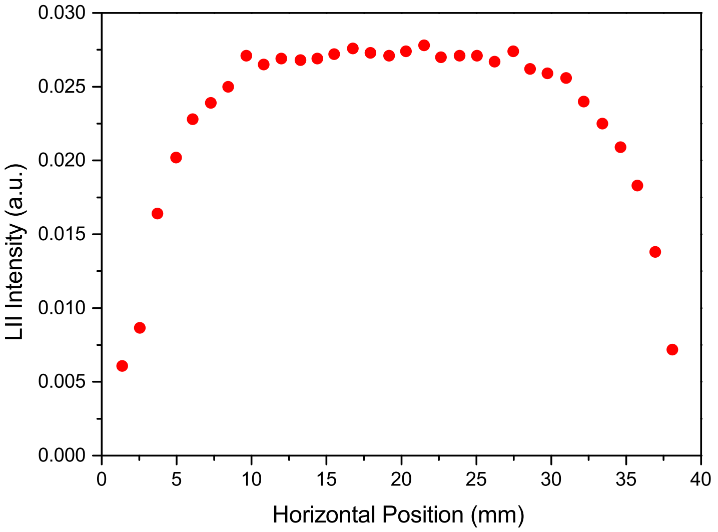

Figure 3.2: LII signal intesity with horizontal position 15 mm above the burner surface within a $\phi = 2.97$ flame (Image reproduced from [69]).

3.3 RGB Image Analysis of Flame Emission

The continuous-wave cavity ring down spectroscopy (cw-CRDS) measurement technique is highly sensitive to additional optical losses caused by the flame, particularly due thermo-optic effects or the presence of particulate soot. For this reason, a number of additional measurements were undertaken on the porous-plug burner. The aim of these measurements was to aid in the interpretation of the cw-CRDS experimental results. In particular, these measurements allow the position of the reaction zone of the flame to be determined, and assess how its position changes with flame conditions. Knowledge of this position is essential as the steepest thermal gradients are present in the reaction zone and therefore this position will have the strongest thermo-optic perturbations. The position of the reaction zone is assessed from images of the visible emission from the flame. The methodology and results of this investigation are described in this section.

A Number of complex imaging systems have become more prevalent in combustion diagnostics [70–72]. However it was decided that a commercial digital single lens reflex (DSLR) camera could provide a convenient, and relatively inexpensive tool which can be used to measure emission from the flame. To achieve this a DSLR camera (Canon, model: 450D) was securely mounted on an optical post assembly, with the centre of the lens positioned 10.5 mm above, and perpendicular to, the burner surface. Images were taken of flames over the full range of equivalence ratios shown in table 3.1. To allow for direct image-to-image comparison of emission intensity the camera sensor gain (ISO), aperture, and exposure time were held constant for all images. Example images for each flame condition are shown in figure 3.3.

The images shown in figure 3.3 can be readily separated into their constituent red, blue, and green components using Matlab, and figures 3.4 & 3.5 show the intensity of each component for the $\phi = 2.67$ & $\phi = 2.67$ flames using an average of four images. In the $\phi = 1.77$ flame, the lack of soot particulate can be observed as a reduction of the red and green emission. The lower equivalence ratio leads to more complete combustion and higher temperatures near the reaction zone, resulting in an increase in the intensity of blue and green emission lower in the flame caused by emission from excited molecular radicals. Emission at blue/green wavelengths is characteristic of the ‘Swan bands’ [73] of radical diatomic carbon, with an emission contribution from singlet methylene also present.

Although not undertaken in this work, soot temperature and volume fraction measure-

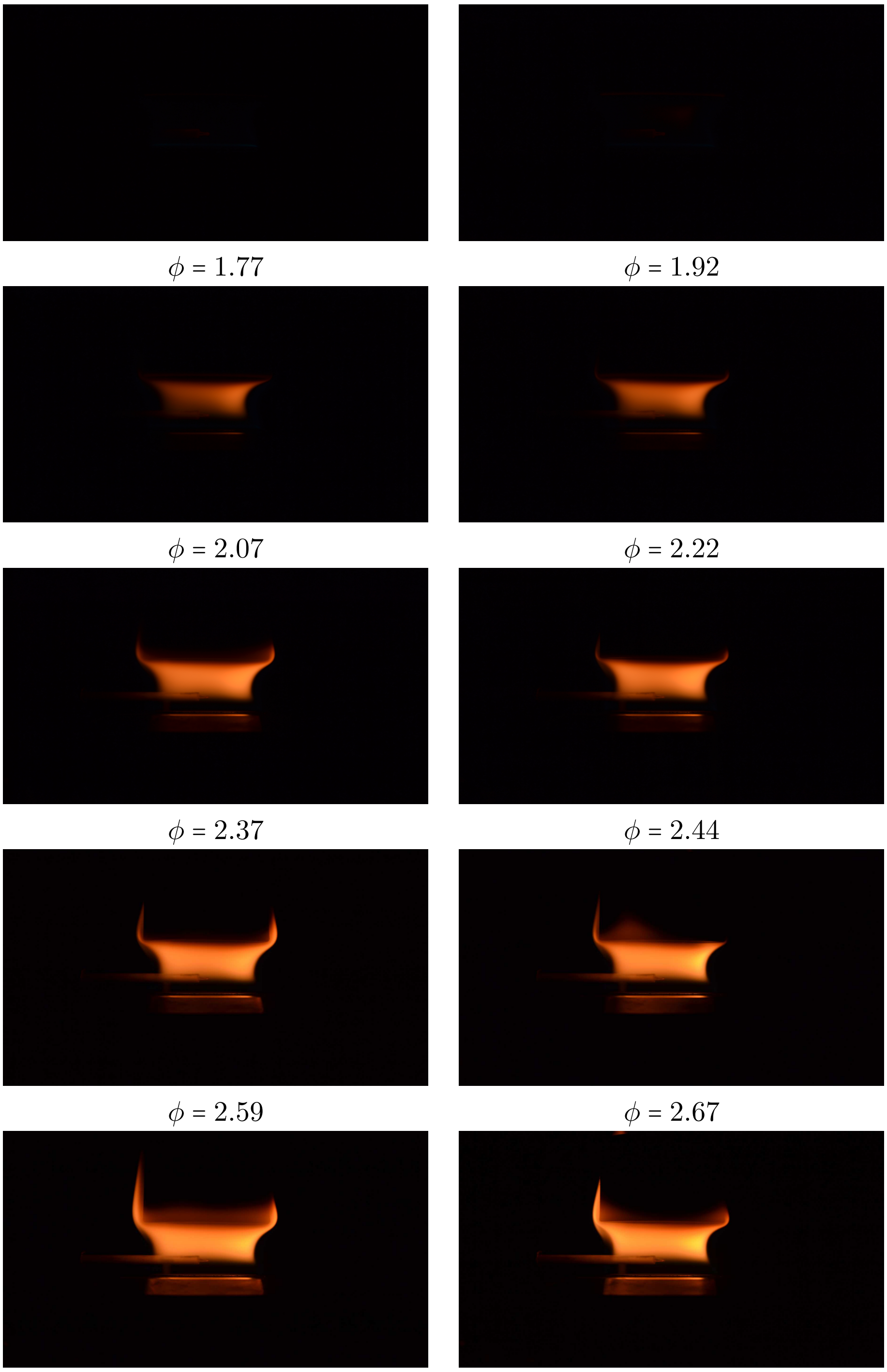

$\phi = 1.77$ $\phi = 1.92$

$\phi = 2.07$ $\phi = 2.22$

$\phi = 2.37$ $\phi = 2.44$

$\phi = 2.59$ $\phi = 2.67$

$\phi = 2.82$ $\phi = 2.97$

Figure 3.3: DSLR camera images of all flames ($\phi = 1.77$ to $\phi = 2.97$)

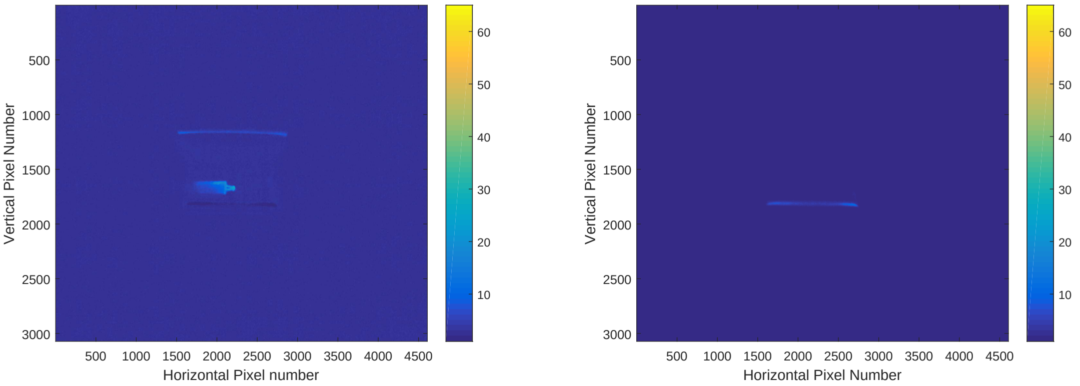

ϕ = 1.77 Red Component

ϕ = 1.77 Green Component

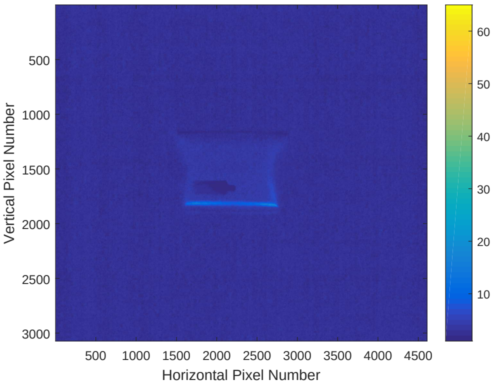

ϕ = 1.77 Blue Component

Figure 3.4: Separated RGB components for average of 4 images of the ϕ = 1.77 flame

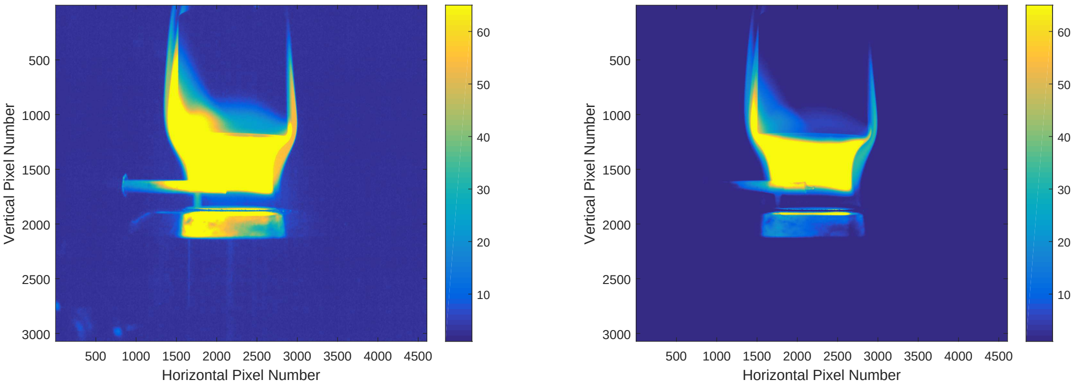

ϕ = 2.67 Red Component

ϕ = 2.67 Green Component

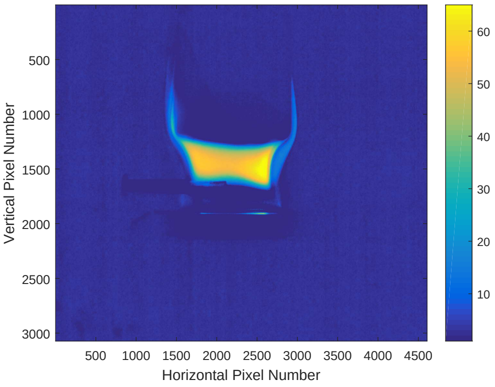

ϕ = 2.67 Blue Component

Figure 3.5: Separated RGB components for average of 4 images of the ϕ = 2.67 flame

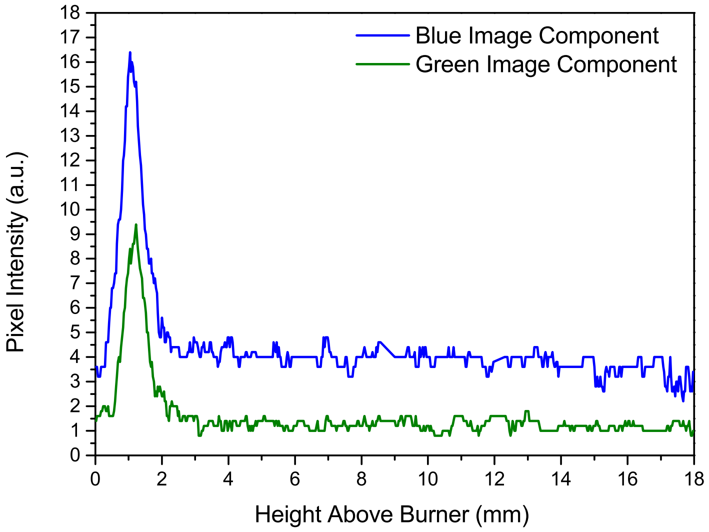

Figure 3.6: Blue and green image components vs height above burner for a $\phi = 1.77$ flame

ments based on the ratio of the intensity of emission of each RGB element using a DSLR camera were demonstrated by Guo et. al [71]. The approach of making quantitative measurements from radiative emission, at selective wavelengths as well as broadband measurements, from soot has found wide use in soot formation studies [74–76], and is often used to better understand measurements made using other techniques [77]. Emission based measurement has the advantage over laser based measurements that it is entirely passive and therefore there is no potential for perturbation [27]. Furthermore, it can be implemented on a range of combustion systems.

To allow for meaningful comparison to laser-based optical measurements, the vertical pixel number from the camera was calibrated to height above the burner. This was completed by photographing a steel rule at both the front and rear edges of the porous plug, with the average of these measurements used as the calibration for the centreline of the burner. Calibrating the images in this way is not ideal, as it makes the assumption that the flame is two dimensional. The individual pixels in the image will contain emission contributions originating from above/below the height determined

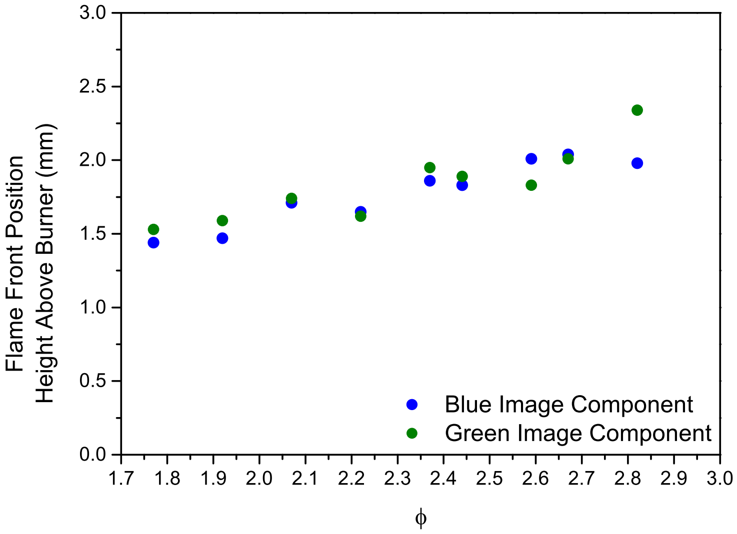

Figure 3.7: Estimation of reaction zone position based on peak emission of blue and green image components

from the calibration. Nevertheless, measurements made using this method can contain useful information about the combustion process. Following further calibration of the camera sensor response there is scope to use this technique to obtain the radial emission profile using a technique such as an Abel inversion [78]

Figure 3.6 shows the average blue and green components of 4 images taken for a $\phi = 1.77$ flame as a function of height above the burner. There is a definite peak indicating a high rate of heat release, between 1 mm and 2 mm HAB which is near the expected position of the reaction zone. As the equivalence ratio is increased the intensity of the blue and green emission near the reaction zone diminishes as the temperature decreases due to the increasing heat capacity of the incomplete combustion products [79]. The position of the peak of this emission can be used to estimate the relative position of the reaction zone as the equivalence ratio is varied. Figure 3.7 shows the estimated position for a range of different equivalence ratios.

The decreased intensity of the blue and green emission in the higher equivalence ratio flames results in a greater uncertainty in the estimation of the position of the reaction zone. The highest equivalence ratio flame imaged, ϕ = 2.97, has not been included in figure 3.7 as the signal to noise ratio at the peak of the blue and green emission is not sufficient to give a good estimation of position (SNR< 2). Further uncertainty in the position is encountered in high equivalence ratio flames as significant reflection of the brighter emission higher in the flame occurs at the burner surface, increasing the noise in the emission peak. In rich flames above ϕ = 2.67 a 4th order polynomial fit was applied over the emission peak to better estimate the peak position despite the increased noise.

The position of the reaction zone appears to move upwards from the surface of the burner. This is assumed to be due to a reduced requirement for heat transfer to the burner surface due to the reduction in the flame temperature. This information is useful for the design of new optical measurement techniques, such as cw-CRDS, as the strongest thermal gradients, and hence optical disturbance, exist close to the reaction zone, which can pose a challenge for such measurements.

Figure 3.3 indicates that visible orange emission begins to occur at an equivalence ratio between ϕ = 1.92 and ϕ = 2.07. These flames should possess a relatively low soot volume fraction, and it is assumed that this orange emission occurs due to the presence large poly-aromatic hydrocarbons or small nascent particles.

3.3.1 Comparison to Laser Induced Incandescence (LII)

Laser induced incandescence (LII) is widely becoming accepted as the pre-eminent technique used to conduct measurements of particulate matter (soot) in-situ in flames, due to its ability to undertake rapid spatiality resolved measurements [80]. LII operates by heating any present particulate matter, using a suitably powered laser, to an elevated temperature where they begin to emit significant additional Planck radiation [23]. With proper calibration, the magnitude of this incandescent emission can be used to quantify the volume fraction of the particulate. LII measurements are normally under-

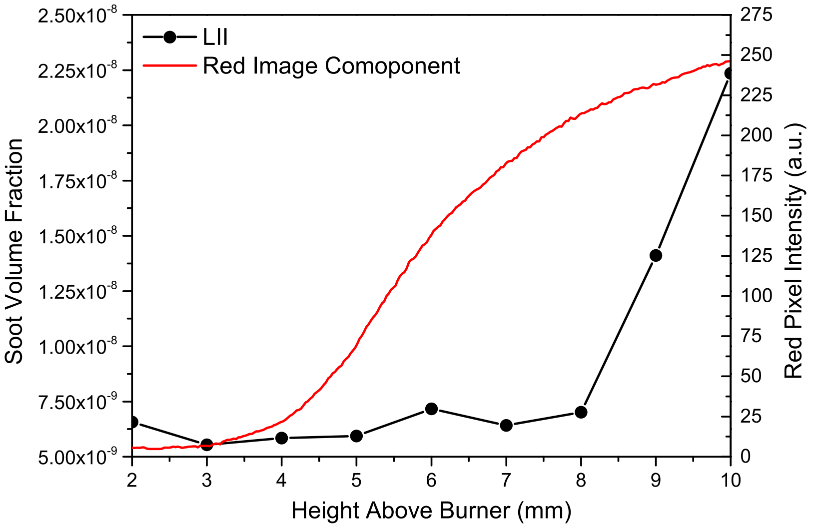

Figure 3.8: Comparison of red emission with soot volume fraction measured using prompt LII for a $\phi = 2.44$ flame.

taken using a pulsed laser source, allowing the particulate to be rapidly heated before cooling at a slower rate. The time between laser excitation and measurement of the incandescent signal can be varied from immediate detection of the magnitude of the LII signal (prompt detection) to a point, typically several 10s of ns, after excitation (delayed detection).

Dunn [69] employed the LII technique to measure soot volume fraction within a range of flame conditions from $\phi = 2.44$ to $\phi = 2.97$. These measurements were made using the prompt approach at an excitation wavelength of 1064 nm. The LII signal was calibrated to a measurement of soot volume fraction by optical extinction. The LII would appear to show a clear threshold at 7 – 8 mm above the burner, dependent on equivalence ratio where soot becomes present, with the volume fraction of soot above this point increasing with equivalence ratio.

Figure 3.8 shows a comparison of the red image component of the $\phi = 2.44$ flame and the soot volume fraction measured by Dunn using prompt LII close to the region where the formation of particulate soot is thought to begin. The visible orange emission becomes significant at approximately 5 mm above the burner surface, however the soot volume fraction measured by LII only shows a significant increase at 8 mm above the burner. This discrepancy indicates that the orange emission in the lower regions of the flame may originate from large organic molecules and/or nascent soot particles. The high laser fluence used by Dunn, typical for pulsed laser LII measurements, may lead to the sublimation of such small nascent particles and could partly account for the lack of LII signal observed at these lower positions.

In addition to these soot volume fraction measurements Dunn also undertook LII measurements at 532 nm, and 283 nm, where the LII signal contains a fluorescence component arising due to the presence of poly-aromatic hydrocarbons (PAHs). If the LII contribution generated using 1064 nm is subtracted from the measurements made using 532 nm, and 283 nm inferences could be made about the concentration profile and class of the PAHs present. The maximum florescence signal occurred around 4 mm to 5 mm above the burner, indicating the presence of PAHs in this region. This supports the hypothesis that the orange emission that begins at this position may be due these large aromatic molecules.

3.4 Measurement of Soot Distribution by the Photoacoustic Effect

Photoacoustic detection has been used for high sensitivity detection of trace gases using IR absorption spectroscopy [81], and environmental particulate levels [82]. In this technique the optical energy is absorbed by any particulate present, this results in localised of the particles. This heat is transferred from the particles to the surrounding gas, resulting in the expansion of the gas [83]. Modulating the laser intensity leads to a variation in the rate of heat transfer, resulting in an acoustic pressure wave [84], and this pressure wave can then be detected using either a microphone or a piezoelectric transducer (typically used for higher frequencies). Assuming that the modulation fre-

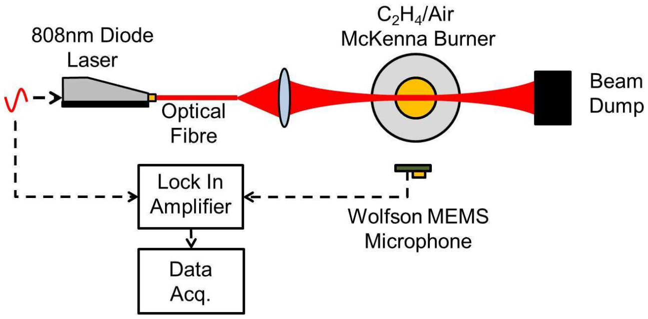

Figure 3.9: Experimental set-up for photoacoustic soot measurement.

quency of the incident laser light is much slower than the rate of heat transfer from the absorbing media to the surrounding gas the frequency of the generated acoustic wave will be the same as the modulation frequency of the laser.

Using lock-in amplification will suppress any noise that is not at the modulation frequency, as lock-in amplification acts as a narrow-band filter with an output of the amplitude of the detected signal at the lock-in amplifiers reference frequency. Therefore, lock-in detection is well suited to photoacoustic measurement, providing there are no sources of acoustic noise at, or very close to, the modulation frequency. The sensitivity of photoacoustic detection can generally be improved by increasing the amplitude of the intensity modulation of the incident laser light, referred to as the modulation depth.

This section will present a novel photoacoustic method for the in-situ measurment of the distribution of soot within the flame. These measurements, along with the previous LII measurements, will provide information about the optical loss due to the presence of particulate soot, which could limit the sensitivity of cw-CRDS.

3.4.1 Experimental set-up for photoacoustic soot measurement

The experimental set up used for photoacoustic soot measurement is shown in figure 3.9. A fibre-coupled, high-power continuous-wave diode laser, with a maximum power of 30 W ($\lambda = 808$ nm, DiLAS), was used to heat the soot particulate present in the flame. The light was delivered to the burner using 600 μm core diameter multi-mode fibre, then focused using a plano-convex lens, with a focal length of 120 mm. The transverse profile of the laser beam was measured at several points along the beam path by translating a knife edge through the beam.and was found to have a $1/e^2$ beam diameter of 1.06 mm at the centre of the burner. The beam waist was nearly constant over the burner diameter, expanding out to a $1/e^2$ beam diameter of 1.30 mm at the extremities of the flame, and the beam was measured to have a near-Gaussian intensity distribution.

The laser power was modulated sinusoidally at 10 kHz by supplying a modulated control voltage from a function generator to the laser drive electronics which in turn modulated the current supplied to the laser diode. A thermal laser power meter was used to terminate the beam, and to monitor the power of the beam when setting the control voltage. in The resulting intensity modulation produced an acoustic wave, that was then detected using a MEMS microphone (Wolfson Microelectronics) located 60 mm from the burner centre-line.

The microphone, was originally designed for hearing aid applications, and has a flat output response up to 20 kHz , implying that a broadband acoustic measurement would be highly susceptible to background noise. A hardware lock-in amplifier module (Stanford Research Systems, model: SRS 830)was used, and a relatively high modulation frequency of 10 kHz was selected. This frequency was selected as the power spectral density of any ambient acoustic noise is expected to be roughly inversely proportional to frequency. The time constant of the lock-in amplifier was set to 3 s to minimise the effect of any low frequency disturbances to the flame. The output from the lock-in amplifier was recorded using a data acquisition card (National Instruments, model: PCI-6120) for in an integration time of 10 s, at a sampling rate of 1 KS/s.

It was initially thought that a large intensity modulation amplitude would be required to achieve the required sensitivity for soot measurement. In fact, the intensity modulation amplitude of the laser was limited by the frequency response of the available drive electronics and the frequency response of the laser diode itself. Even though the control voltage for the laser was modulated through its full range of 10 V this produced

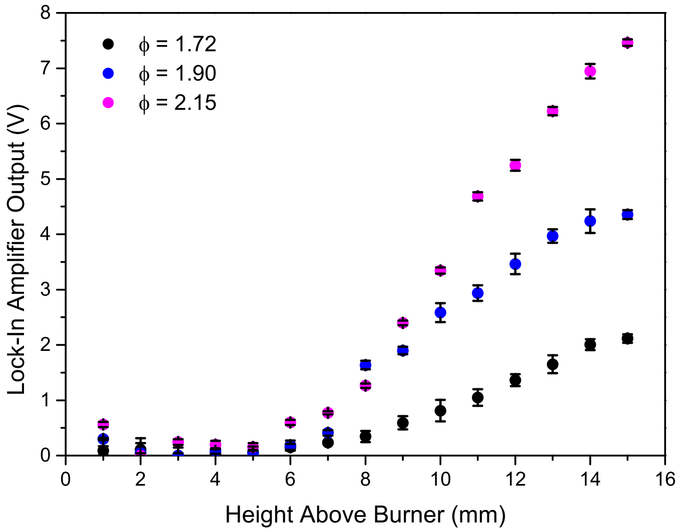

Figure 3.10: Lock in amplifier output voltage using photoacoustic detection in 3 sooting flames.

an intensity modulation amplitude of only 130 mW, instead of the expected 30 W. However, experimentally it was shown that this modulation amplitude was still sufficient to make useful measurements. To improve the sensitivity of the technique the use of an optical chopper was investigated as a means of producing a higher modulation depth, but practical difficulties were encountered in achieving a sufficiently high modulation frequency. Although an increased intensity modulation depth was achieved, increasing the amplitude of the acoustic signal to audible levels, additional noise was observed on the output of the lock-in amplifier. This was attributed to unstable photoacoustic effects which were generated at the detection frequency due to the laser heating the chopper blades. Even when the voltage controlled modulation method was employed a significant background photoacoustic signal could be detected in absence of the flame, the majority of this background signal was attributed to laser heating of the optical components and the power meter.

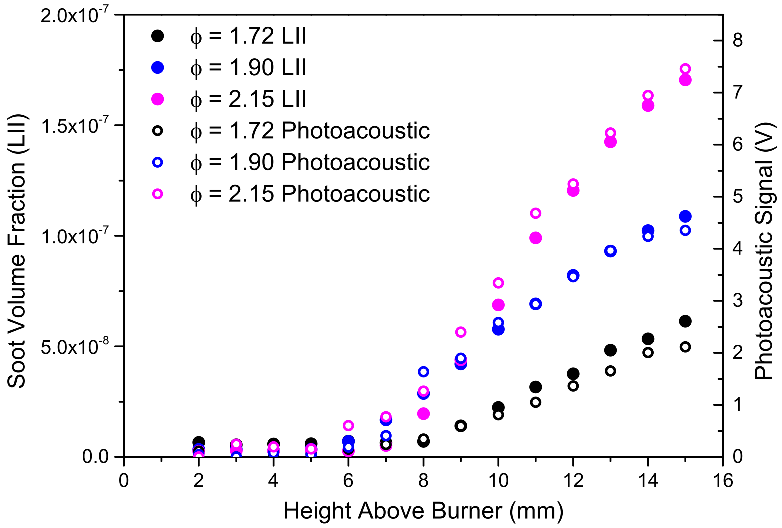

Figure 3.11: Lock in amplifier output voltage using photoacoustic detection in 3 sooting flames.

3.4.2 Comparison of photoacoustic and LII soot measurements.

Measurements of the photoacoustic signal recorded for flames of three different equivalence ratios (ϕ = 2.44, ϕ = 2.67, and ϕ = 2.97) taken across a range of positions above the burner surface are shown in figure 3.10. The background signal in absence of any absorption from particulate present in the flame was measured to be 0.23 V and this value has been subtracted from each data point. The photoacoustic measurements indicate that significant absorption occurs at positions 6 mm to 7 mm above the burner, indicating that the onset of soot formation occurs at this point. This agrees well with the previous LII measurements taken by Dunn. A high level of repeatability can be observed in the measurements: the error bars in figure 3.10 represent the standard deviation calculated from three repeated height translations, this is due to the combination of long integration time and lock-in amplifier time constant. Figure 3.11 shows a comparison of the magnitude of the photoacoustic signal with the soot volume fraction measurements made using LII by Dunn. There is a very good correlation between the two measurement techniques, indicating that the majority of the absorption encountered within the flame arises from the presence of soot particulate.

Finally, to confirm that the photoacoustic signal detected by the MEMS microphone had originated from the interaction of the laser with the flame, and not due to any ambient photoacoustic effects, the position of the microphone was translated on a horizontal axis perpendicular to the laser beam axis and signals were recorded at each location as described above. The results from this test are shown in figure 3.12, and show that recorded signals closely follow an inverse-square ($1/R^2$, where R is the separation distance) relationship with distance from the source of the sound at the centre of the burner. However, this relationship is only likely to be a true approximation at separations where the source of sound can be considered a point source. As the seperation distance is decreased the cylindrical nature of the laser-soot interaction will mean that the relationship tends more towards a simple inverse ($1/R$)

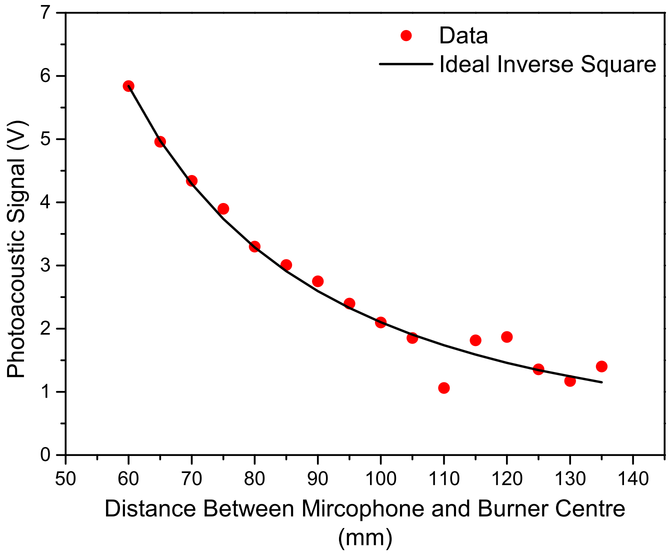

Figure 3.12: Results of translating the microphone away from the burner with a model inverse-square law ($1/R^2$) drop off from the initial value.

3.4.3 Calibration of acoustic signal

As with the LII approach, calibration of the photoacoustic signal requires an independent measurement of soot volume fraction. A common calibration technique is to measure the extinction of the laser energy due to absorption. There are numerous disadvantages to this approach, such as the extremely low extinction encountered at low soot volume fractions, and uncertainties in the optical properties of the soot. Despite the disadvantages, extinction calibration has been shown to give good agreements with other measurement methods [74]. If it is assumed that the extinction coefficient k_{ext} is equivalent to the absorption coefficient of the soot k_{abs} then the soot volume fraction f_v can be determined using

$$k_{ext} \approx k_{abs} = f_v \frac{6\pi E\left(m\right)}{\lambda} \tag{3.2}$$

where $E\left(m\right)$ is the soot absorption function and λ the wavelength if of the light used to make the extinction measurement. Although $E\left(m\right)$ can vary as the soot structure changes. A constant value of $E\left(m\right)$ was adopted, due to the complexity of determining an accurate value of $E\left(m\right)$ for all the positions and flames. A value of $E(m) = 0.3 \pm 0.06$ is suggested by Schulz et al. [85] as being representative of the range of measured $E(m)$ values.

It is somewhat counter intuitive that the low modulation depth produced by the DiLas laser would produce such a strong acoustic signal. Calibration of the acoustic signal was undertaken by measuring the extinction of the DiLas laser due to the presence of soot 15 mm above the burner in the $\phi = 2.97$ flame. To do this, a lower laser power of 2 W was used, which was the lowest power at which the laser output power was stable. The transmitted beam was sampled ($\approx 4\%$)using a reflection from a quartz microscope slide, which was further attenuated by neutral density filters before being focused onto a silicon photodiode. The output of the photodiode was calibrated using the thermal power meter, and was found to have a linear response up to the maximum laser output

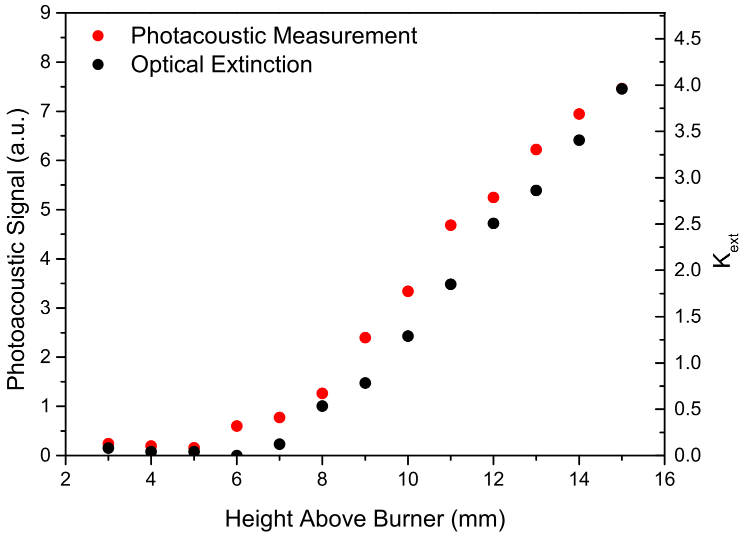

Figure 3.13: Comparison of extinction coefficient and photoacoustic signal for the ϕ = 2.97 flame.

power. Repeated measurements were taken in the presence and absence of the flame. For the purpose of calculating the extinction coefficient, the radial soot distribution was assumed to have a top-hat profile with a diameter of 33 mm.

Although only a single calibration point was required, additional extinction measurements were completed for each height above the burner as shown on figure 3.13. Measurements below 2 mm are omitted due to the high optical extinction from the optical disturbances encountered close to the reaction zone. The extinction coefficient at each height correlates well with the photoacoustic signal however, the value of 3.96 at 15 mm suggests a soot volume fraction of 5.66×10^{-7} (using equation 3.2). Errors in the extinction calibration arising due to errant emission from the flame were effectively minimised in the recalibration as they are of a relatively low energy compared to the laser, and do not produce a significant output on the photodiode. The high extinction coefficient gives an explanation as to why the acoustic signal can easily be detected despite the decreased modulation depth.

This new extinction data was used to recalibrate the previous LII measurements, and

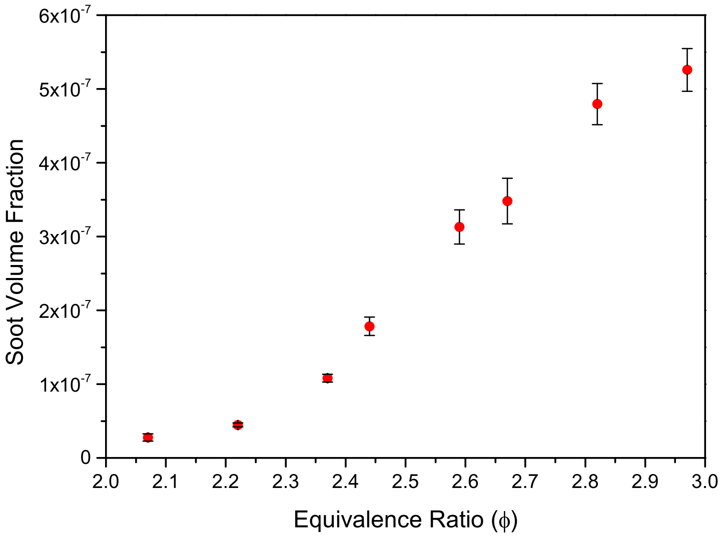

Figure 3.14: Soot volume fraction at a range of equivalence ratios measured 14 mm above the burner using extinction-calibrated photoacoustic detection

calibrate the photoacoustic measurements, for the lower equivalence ratios, to provide values for soot volume fraction. The results of this calibration are shown on figure 3.15. Figure 3.14 shows the measured soot volume fraction 14 mm above the burner for a range of equivalence ratios which appear to show that there is a threshold for soot formation at an equivalence ratio between $\phi = 2.07$ and $\phi = 2.22$.

Figure 3.14 shows photoacoustic soot measurements taken 14 mm above the burner, over a wider range of equivalence ratios ($\phi = 2.07$ to $\phi = 2.97$) . Comparison of these photoacoustic measurements with the raw flame images (Figure 3.3) shows that although soot formation begins at $\phi \approx 2.07$, the orange emission from soot particles begins at a slightly lower equivalence ratio, between $\phi = 1.92$ and $\phi = 2.07$). Although a relatively high power continuous-wave laser source was used for the photoacoustic measurements the laser fluency is still substantially lower than the prompt LII measurements undertaken by Dunn, therefore it is unlikely that smaller soot particles would be vaporised using this method. This provides further evidence that this emission most probably occurs from nascent soot particles or large PAH molecules, which do not absorb sufficient

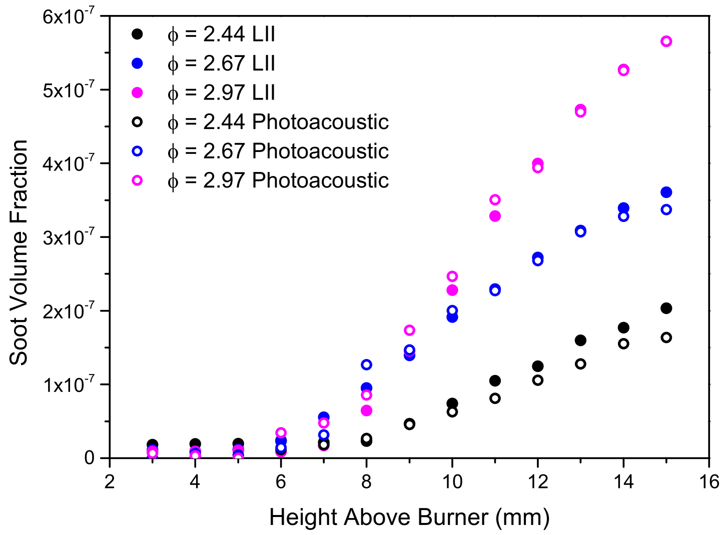

Figure 3.15: Comparison of soot profiles obtained using photoacoustic and LII detection methods, calibrated with the updated extinction measurements.

laser energy to produce a significant acoustic signal. A key point in this possible explanation is the different properties of nascent particles and mature soot, with nascent soot having a quasi-liquid like structure [21]. This could lead to the nascent particles possessing different optical properties, from mature soot, such as $E\left(m\right)$ [86], which can effect the absorption of laser energy, and therefore the generation of an acoustic or LII signal. There is considerable debate as to the correct value of $E\left(m\right)$ as it is critical the interpretation of optical soot measurements, which are calibrated by extinction, and recently great effort has been devoted to determining the correct value through the soot formation process [87].

3.4.4 Review of the photoacoustic measurement technique

The photoacoustic measurements compare well to those made using the well-established LII technique, producing repeatable measurements across a range of flame conditions. The simplicity and low cost of photoacoustic soot detection using fibre-coupled cw-diode lasers may make it an attractive alternative for certain applications. One of the disadvantages of the technique, compared to spatially resolved techniques such as LII, is that the measurements are integrated along the laser path-length. Therefore, following the currently the technique is limited to applications, such as flat-flame burners where there is little variation in soot volume along the path-length.

The long term stability of the porous-plug burner allows for a long integration time to be used, which reduces the effect of sporadic short-term disturbances on the measurement. If the sensitivity of the technique was improved, e.g. by using a laser source which is capable of a greater modulation depth), the integration time could be reduced and therefore more temporarily resolved measurements could be made. A further limitation to this is that the time constant for the lock-in amplifier must be several times the modulation period of the laser. Despite these apparent disadvantages the simplicity and low cost of the photoacoustic technique, and the convenience of using fibre-coupled cw-diode lasers, may make it an attractive alternative for certain applications.

3.5 Temperature estimation using laser induced fluoresce of OH

As described in chapter 2 accurate measurements of gas temperature are essential tor the interpretation of absorption spectra in order to achieve accurate values for species concentration. Hu made temperature measurements using the laser induced fluorescence (LIF) technique.

LIF [88] occurs when energy is spontaneously emitted by a molecule which had previously been raised to an excited state through absorption of laser energy. In order to undertake temperature measurements in the porous-plug burner Hu measured the relative intensities of seven emission lines of the rotational band of hydroxyl (OH), at a wavelengths around of 303 nm. The ratio of the emission intensity of these lines was then used to prepare a linear Boltzmann plot which could be used to infer temperature. The nature of OH LIF thermometry requires a significant concentration of OH to be present. OH is only present close to the reaction zone and hence measurement accuracy decreases at higher elevations above the burner surface, and almost impossible above 4 mm and below 0.6 mm. The average temperature in the plateau region, away from the reaction zone, appear to be ≈ 1600 K for this flame. Due to the low concentration of OH there was a high level of variance in the temperature measurements undertaken in this way however, the average temperature profile in this region compares well to the temperature predicted using kinetic modelling.

3.6 Summary

In section 3.1 the background and underpinning assumptions for the standard McKenna burner was presented and compared with the the porous-plug burner used in this work, the design of which was presented in section 3.2. To aid in the novel application of cw-CRDS to the burner, which is the primary focus of this work additional characterisation measurements were undertaken on the emission from the flame using a commercial DSLR camera, these measurements are presented in section 3.3. A novel soot measurement technique based on the photoacoustic effect was presented in section 3.4 and the measurements were compared with the previous measurements made using the LII technique.

The measurements indicated that orange emission occurred in the flame before any particulate could be detected using either the LII or the photoacoustic technique. This emission was thought to originate from nascent particles which did not absorb sufficient energy for detection or from large PAH molecules.

4 Continuous-Wave Cavity Ring Down Spectrometer Design

4.1 Introduction

Laser absorption spectroscopy is a technique which is well suited to conducting in-situ concentration measurements in reacting flows, such as flames. Absorption spectroscopy is minimally intrusive, requiring only modest laser power in the majority of applications and therefore does not impart significant energy which could cause a change if conditions in the flow being measured [85]. The background and theory for using diode laser absorption spectroscopy in the near-infrared (NIR) for species concentration measurements was presented and discussed in chapter 2

Standard single-pass absorption spectroscopy often lacks the required sensitivity for species concentration measurements in flames. This can be due to a combination of the low concentration or the low absorption cross-section of the target species, a short interaction length and the intense background emission [89]. The sensitivity of absorption measurements can be improved by increasing the laser-gas interaction length, passing the light through the gas multiple times. This can be achieved by coupling the light into an optical cavity constructed around the measurement volume. Several measurement strategies exist for undertaking such cavity enhanced measurements [90]. Several of the more commonly used cavity enhanced techniques were briefly described in chapter 2.

Cavity ring-down spectroscopy (CRDS) is one such technique [57], originally developed to measure the optical reflectance of early laser mirrors. During a CRDS measurement the input light into the cavity is terminated, resulting in the intensity of the residual light within the cavity leaking through the cavity output mirror decaying exponentially. If no absorbing medium is present, the rate of decay should ideally only be due to mirror transmission/scattering losses. When an absorbing species is present this rate of decay can be increased proportional to the per-pass absorption losses in the optical cavity.

In this chapter the theory and practical considerations that are required for the design of a continuous-wave cavity ring-down spectrometer will be presented and evaluated. The outcomes from this evaluation will be used as a basis for the design of a spectrometer capable of operating in-situ in a combustion process.

4.2 Cavity Ring-Down Spectroscopy Theory

Consider a cavity formed of two high reflectivity ($\mathcal{R} > 0.999$) mirrors where a proportion d of the cavity length is occupied by a species with absorbance A. It is assumed the the only losses from the cavity are due to absorption and interactions with the cavity mirrors. The derivation given here is adapted from [56].

In Chapter 2 the Beer-Lambert law was introduced to define the proportion I of incident I_0 light that is transmitted after interacting with the absorbing species [].

$$\frac{I}{I_0} = \exp\left(-Ad\right) \tag{4.1}$$

Considering a single round trip of light between two mirrors separated by an absorbing medium, optical intensity within the cavity will be lost during the two mirror interactions and due to absorption through the path between reflections. Hence, the intensity I_n remaining following n complete round trips is:

$$I_n = I_0\mathcal{R}^{2n}\exp\left(-2nAd\right) \tag{4.2}$$

with the time t taken to complete n round trips given by

$$t = \frac{2nL_c}{c} \tag{4.3}$$

By re-arranging equation 4.3 for n and substituting into equation 4.2, the intensity $I(t)$ of the light remaining within the cavity at any time following termination of the input energy will therefore decay exponentially according to:

$$I(t) = I_0 \exp\left[\frac{tc}{L_c}\left(\ln(\mathcal{R}) - Ad\right)\right] \tag{4.4}$$

The mirrors used for CRDS are typically of a very high reflectivity ($\mathcal{R} \approx 1$), therefore the approximation of $\ln(\mathcal{R}) \approx (1 - \mathcal{R})$. Using this assumption a new parameter, ring-down time τ can be defined as the decay constant according to:

$$\tau = \frac{L_c}{c\left[(1 - \mathcal{R}) + Ad\right]} \tag{4.5}$$

Thus the decay function for the intensity of the light in the cavity can be described as:

$$I(t) = I_0 \exp\left(-\frac{t}{\tau}\right) \tag{4.6}$$

By measuring the decay constant of the exponential decay the CRDS technique is independent of the initial intensity within the cavity and is therefore not affected by any intensity fluctuations to the input light to the cavity. Hence, the minimum detectable absorption measured with CRDS is defined by the reflectivity of the cavity mirrors and the minimum observable change in the ring-down time compared to an 'empty' cavity. In most practical applications it is likely that there may be additional optical loss within the cavity. To account for this an additional loss term X can be included in equation 4.5

$$\tau = \frac{L_c}{c\left[(1 - \mathcal{R}) + Ad + X\right]} \tag{4.7}$$

The simple case described above is known as the 'photon bullet' or 'ping-pong' model which assumes that no overlap or interference occurs between the forward and backward propagating light. In order to fully describe the theory of CRDS (and in particular cw-CRDS) such interference effects must be considered. Section 4.3 describes the more complex case where the light within the cavity overlaps with the input light.

4.3 Optical Cavity Theory

To allow the design a cw-CRDS spectrometer that is capable of making sensitive absorption measurements in-situ in the porous-plug burner, it is first necessary to summarise the theoretical description of resonant optical cavities.

The simplest form of optical cavity is a linear cavity constructed from two mirrors, between which a self replicating or 'standing' wave can be maintained allowing the intensity of the light in the cavity to build up over time. For simplicity the description given in this work is restricted to the propagation of monochromatic laser light within the cavity.

4.3.1 Frequency Response of Optical Cavities

A standing wave will be formed when the cavity length and the wavelength of the light are at a resonant condition, such that the incoming light constructively interferes with the light reflected from the far cavity mirror.

In the simple two mirror cavity configuration resonance will occur when the cavity length is equal to an integer number of half-wavelengths. This is due to the π phase shift that occurs as the light is reflected from the mirror surface. Due to this phase shift the amplitude of the em wave must be equal to zero at the mirror surface to fully overlap the incident wave. The periodic conditions required to achieve resonance are know as the 'longitudinal resonant modes' of the cavity. Mathematically, the conditions required for resonance can be defined as [92]

$$L_c = q\left(\frac{\lambda}{2}\right) \tag{4.8}$$

where q is an integer number (known as the mode number), λ the wavelength of the

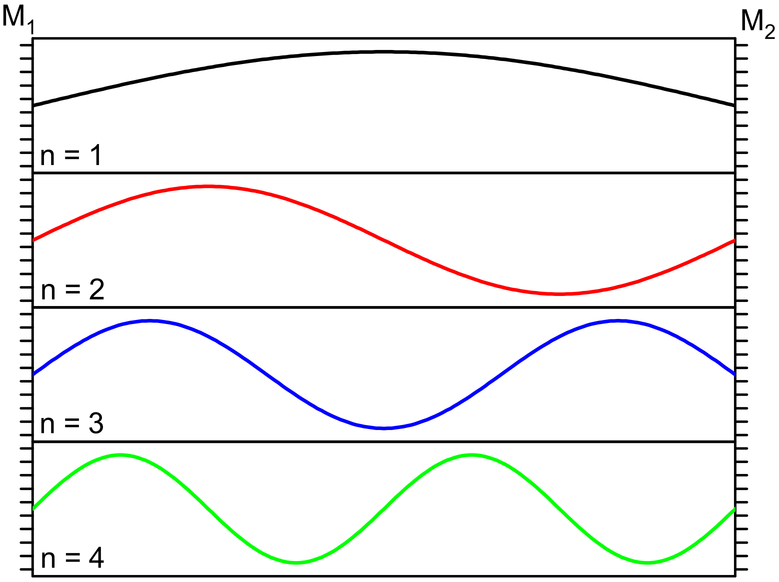

Figure 4.1: The first 4 longitudinal resonant modes of a simple 2 mirror cavity.

incident light, and L_c is the mirror separation, i.e. the length of the cavity. diagram depicting the first four longitudinal modes of a simple two mirror M_1,M_2 cavity is shown in figure 4.1.

The frequencies of light at which the cavity can support a standing wave are therefore limited by the above condition, with each mode maintaining a constant frequency separation, known as the 'Free Spectral range' ($\Delta\nu_{FSR}$) of the cavity which is defined as

$$\Delta\nu_{FSR} = \frac{c}{2L_c} \tag{4.9}$$

where c is the speed of light in the medium separating the mirrors.

The variation of the optical intensity of the light within the two mirror cavity as its length is varied by a small distance (2λ) is shown in figure 4.2. The Lorentzian shape of the longitudinal modes can be described by introducing the concept of the 'Finesse' of the cavity. Until now we have not considered any potential loss to the light within the cavity. In a practical optical cavity the cavity mirrors will not return all of the

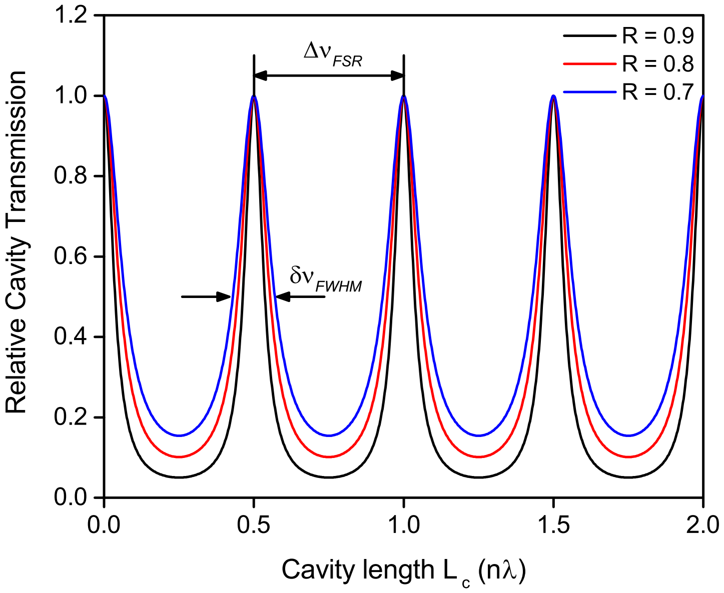

Figure 4.2: Theoretical response of a 2 mirror cavity through a small change in the cavity length.

light which is incident on the mirror surface, with some light being scattered out of the cavity, and a proportion of the light being transmitted through the mirror. The reflectivity parameter $\mathcal{R}$ represents the proportion of the incident light that is reflected from the mirror surface.

For a lossless cavity constructed using ideal mirrors ($\mathcal{R}$ = 1,) the condition described in equation 4.8 permits only resonant frequencies to exist within the cavity. All other non-resonant frequencies are suppressed by destructive interference. However, when there is a source of loss in the cavity (such as a reduction in the mirror reflectivity, shown in figure 4.2) the intensity of the reflected light is reduced which, in turn, reduces the effect of the destructive interference. This permits a wider range frequencies to build up within the cavity, leading to the broadening of the longitudinal modes. Mathematically the finesse is a function of the 'effective reflectivity' $\mathcal{R}_{eff}$ of the cavity and represents the ratio of the full width half maximum (FWHM) of the modes to their free spectral range

$$\mathcal{F} = \frac{\pi\sqrt{\mathcal{R}_{eff}}}{\left(1 - \mathcal{R}_{eff}\right)} \tag{4.10}$$

It therefore follows that the FWHM of the modes, known as the 'cavity bandwidth' $\delta\nu_{FWHM}$, which is given as.

$$\delta\nu_{FWHM} = \frac{\Delta\nu_{FSR}}{\mathcal{F}} \tag{4.11}$$

The effective reflectivity is used to account for all losses within the cavity, not merely those caused by interaction with the mirrors. Finesse is a measure of the effective path-length of the cavity and can describe the ability of the cavity to sustain any resonance following a small disturbance to the resonant conditions, such as any instability of the incoming laser light or small changes to the cavity length due to poor mechanical stability. As the effective reflectivity of the cavity increases the proportion of the light which is transmitted through the mirrors is reduced. Therefore, for the cavity to achieve a relative transmission of unity the circulating power within the cavity will be significantly higher than that of the incident light.

For cw-CRDS applications, cavities are often constructed using mirrors with reflectivity greater than 99.99% to achieve the extended path-length and a more favourable sensitivity. This can lead to the cavity having an extremely narrow bandwidth. For example, consider a linear optical cavity of 0.5 m in length which is constructed using such mirrors. Such a cavity would have a finesse $> 30,000$ and a bandwidth of only 9.55 kHz, much narrower than the line-width of the typical laser sources used in these set ups. This results in only a small fraction of the laser power being resonant with the cavity. Also the long-path length produced by such cavities can extend beyond the coherence length of the incident light, causing a chaotic variation in the peak transmission.

4.3.2 Cavity Stability

To obtain a stable resonance within the cavity not only must the frequency conditions described in section 4.3.1 be achieved, the reflected light must also replicate the in-

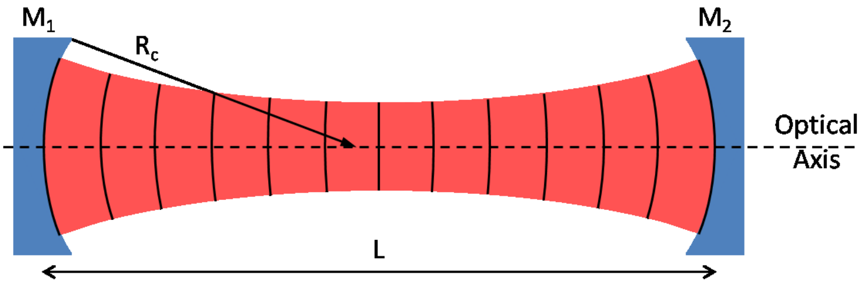

Figure 4.3: Example 2 mirror cavity

coming light spatially following each successive reflection. Empirically this would be achievable using planar mirrors carefully aligned so as to ensure that the incident light into the cavity is normal to the reflective surface ensuring that any subsequent reflections are therefore normal to the surface. In practice however any deviation in this angle, however small, will eventually lead to the light escaping the cavity. Because of the curved mirror construction the propagation of light within the cavity is best described using Gaussian optics, as opposed to geometric ray optics.

For this application Gaussian beams can be described using the complex beam parameter, also known as the q-parameter $q(z)$ which represents the radius of curvature of the wave-front at a distance z from the beam waist w_0. The q-parameter is calculated according to [93]:

$$q(z) = z + z_R i \tag{4.12}$$

where z_R is the Rayleigh range which is the distance along the propagation of the beam at which the cross-sectional area of the beam has doubled. Rayleigh range is determined from wavelength and the size of the beam waist according to [94]:

$$z_R = \frac{\pi w_0^2}{\lambda} \tag{4.13}$$

Considering the optical cavity shown in figure 4.3, constructed from two identical concave spherical mirrors of radius of curvature (ROC) R_c separated by a distance L. In this configuration, the ROC of the wave-front inverts at the centre of the cavity. Al-

Matrix	Component
$\begin{bmatrix} 1 & d \\ 0 & 1 \end{bmatrix}$	Propagation through distance d in free space
$\begin{bmatrix} 1 & 0 \\ \dfrac{-1}{f} & 1 \end{bmatrix}$	A thin lens of focal length f
$\begin{bmatrix} 1 & 0 \\ \dfrac{n_1 - n_2}{R_c n_2} & \dfrac{n_1}{n_2} \end{bmatrix}$	Refraction at a curved surface
$\begin{bmatrix} 1 & 0 \\ \dfrac{-2}{R_c} & 1 \end{bmatrix}$	Reflection from a concave mirror

Table 4.1: Common Ray Matrices

though there is a multitude of stable, multi-mirror cavity configurations in this work consideration is only given to cavities constructed from identical concave spherical mirrors, as this is the simplest configuration and the most commonly used for cw-CRDS.

The choice of an appropriate mirror ROC and separation is important so that the light is not directed out of the cavity after a number of trips. By applying the ray matrix transfer technique [95] the propagation of Gaussian beams at any point in an optical system can be described. Ray transfer matrix analysis applies an $ABCD$-matrix to each component and the change in the q-parameter from q_1 to q_2 is calculated according to [93]:

$$q_2 = \frac{Aq_1 + B}{Cq_1 + D} \tag{4.14}$$

The individual matrices shown in table 4.1 represent a selection of common optical components which can be combined to produce a single $ABCD$-matrix that represents the round trip within the cavity. This matrix is constructed using matrix multiplication from right to left, following the order in which the beam encounters each component. Considering the simple optical cavity shown in figure 4.3, constructed from two concave mirrors of identical radius of curvature R_c, separated by free space distance d, the multiplication will comprise of; The propagation through the length of the cavity to the first mirror, reflection from the first mirror, propagation to the second mirror, and reflection from the second mirror.

$$\begin{bmatrix} A & B \\ C & D \end{bmatrix} = \begin{bmatrix} 1 & 0 \\ \frac{-2}{R_c} & 1 \end{bmatrix} \begin{bmatrix} 1 & L_c \\ 0 & 1 \end{bmatrix} \begin{bmatrix} 1 & 0 \\ \frac{-2}{R_c} & 1 \end{bmatrix} \begin{bmatrix} 1 & L_c \\ 0 & 1 \end{bmatrix} \tag{4.15}$$

As stated above, for the cavity to be stable the light must be constantly refocussed. This requires that the input and output q-parameters are identical ($q_2 = q_1$), and therefore equation 4.14 can be rearranged to give:

$$Cq_2^2 + (D - A)\, q_1 - B = 0 \tag{4.16}$$

and the determinate of the $ABCD$-matrix must be unity. By applying Sylvester's theorem it can be shown that for the cavity to be stable the $ABCD$-matrix must meet the condition [94]:

$$-1 < \left(\frac{A + D}{2}\right) < 1 \tag{4.17}$$

Completing the matrix multiplication on equation 4.15 gives

$$\frac{A + D}{2} = \left[1 - \left(\frac{L_c}{R_c}\right)\right]\left[1 - \left(\frac{L_c}{R_c}\right)\right] - 1 \tag{4.18}$$

If we define a new parameter g_n the'cavity stability parameter' for each mirror according to the equation:

$$g_n = \left[1 - \left(\frac{L_c}{R_c}\right)\right] \tag{4.19}$$

a stable two mirror cavity must meet the condition:

$$0 < g_1 g_2 < 1 \tag{4.20}$$

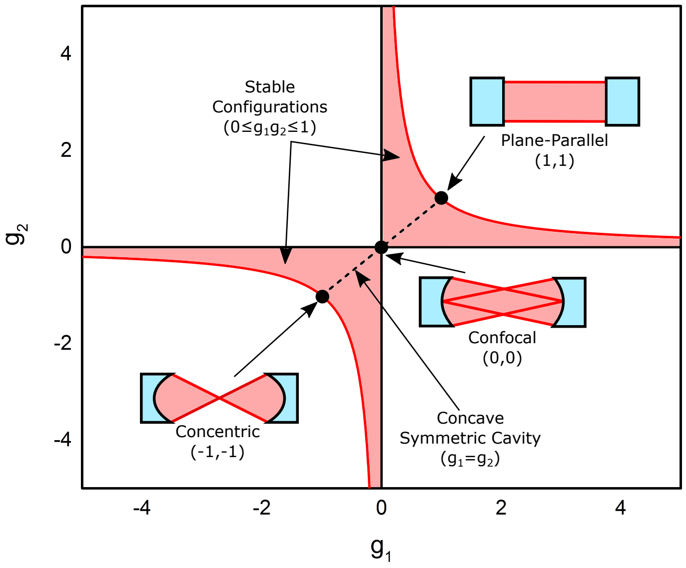

Figure 4.4: Cavity stability plot. Several different symmetrical configurations are shown

Therefore, when designing an optical cavity one should select a combination of mirror radius of curvature and cavity length that satisfies the above condition. Figure 4.4 shows all possible stable configurations for a two mirror cavity. As stipulated above in this work consideration is only given to symmetric cavities constructed from identical ($g_1 = g_2$) concave mirror, and therefore the condition required for a stable cavity is simply:

$$L \leq 2R_c \tag{4.21}$$

4.3.3 Transverse Electromagnetic Modes

To fully describe the propagation of light within the optical cavity consideration must be given to the transverse intensity profile of the beam, described as the transverse electromagnetic modes (TEM). Normally, such modes are modelled as the product of two polynomials, with orders m and n respectively e.g. TEM_{mn}. The fundamental mode is labelled TEM_{00} and has a Gaussian transverse intensity profile. Higher order transverse modes propagate through different optical paths and have a different

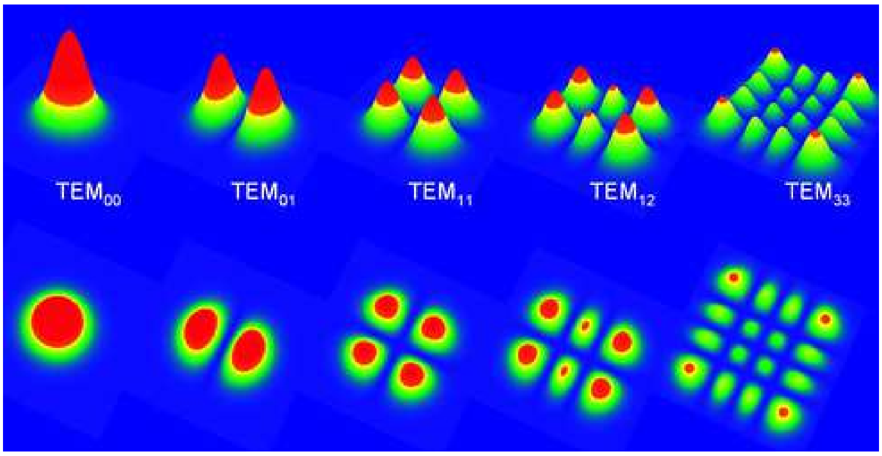

Figure 4.5: Intensity profile of higher order TEM_{mnq} modes (Hermite-Gaussian) Image taken from []

transverse intensity distribution to the TEM_{00} mode. Figure 4.6 shows the transverse intensity distributions for a variety of higher order modes. Compared to the TEM_{00} mode the energy in higher order mods is more spatially extended as the order of the mode increases, illuminating more of the the mirror surface.

For a cavity constructed from spherical concave mirrors the TEM_{00} mode is supported when the wavefront radius of curvature matches that of the mirror surface at the point of refection, and to achieve resonance the magnitude of the electric field at the mirror surface must be zero. The spherical nature of the wavefront causes a phase retardation compared to the planar case. Following the detailed description given by Saleh et al [92] and recalling that the total change in phase for a round trip through the cavity must be a multiple of 2π, we can refine equation 4.8 to represent the TEM_{00} transverse mode as

$$\nu_q = \frac{c}{2L_c}\left[q + \frac{\arccos\left(\pm\sqrt{g^2}\right)}{\pi}\right] \tag{4.22}$$

The free spectral range, $\nu_q - \nu_{q-1}$ remains the same in this more refined picture. Higher order transverse modes resonate at different frequencies therefore the longitudinal res-

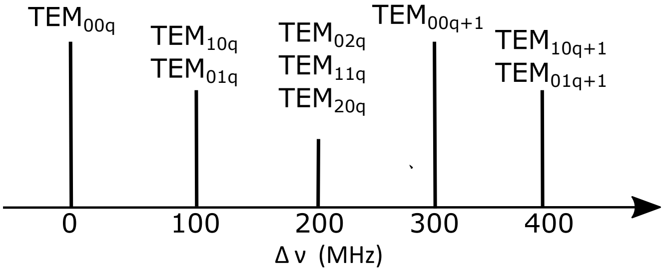

Figure 4.6: Frequency distribution of higher order TEM$_{mnq}$ modes

onant condition for any TEM$_{mn}$ mode can be described as

$$\nu_{mnq} = \frac{c}{2L_c}\left[q + (m+n+1)\frac{\arccos\left(\pm\sqrt{g^2}\right)}{\pi}\right] \tag{4.23}$$

A diagram demonstrating the frequency spacing of several high order modes with respect to the fundamental TEM$_{00}$ mode is shown in figure4.6. It is clear from equation 4.23 that there are numerous higher order transverse modes which share the same resonant frequency, this case is referred to as 'Transverse Mode Degeneracy'. Degeneracy can lead to a reduction in the sensitivity of the CRDS technique as each of the excited modes will have a different decay rate, increasing with the mode order due to increased interaction with the cavity mirrors. Therefore degeneracy between transverse modes leads to the observed decay function having a multi-exponential nature [96]. The light in simultaneously excited transverse modes can also lead to interference noise on the observed decay (a situation known as 'mode beating') leading to further errors in the fitting for the ring-down time [97].

The frequency separation of the higher order transverse modes aids in coupling of the light into a single fundamental TEM$_{00}$ mode in cases where the narrow line-width of laser sources is $<< \Delta\nu_{FSR}$. For example, if we consider a 0.5 m optical cavity constructed from mirrors with 1 m radius of curvature, which would have a free spectral range of 300 MHz the spacing between the TEM$_{00}$ and the adjacent TEM$_{01}$/TEM$_{10}$ modes would be 100 MHz.

4.3.4 Mode-Matching

To achieve a high level of coupling efficiency and couple most of the incident laser light within the cavity the propagation of the input beam must match that of the target transverse mode, for cw-CRDS applications this is normally the fundamental TEM_{00} mode.

Before a solution can be designed to preferentially excite the fundamental TEM_{00} mode it is first necessary to describe the propagation of the TEM_{00} mode along the length of the cavity. As stated in section 4.3.2, the TEM_{00} mode has the shape of a Gaussian beam with a wave-front curvature that matches the mirror curvature at the point of reflection. For a symmetrical cavity the beam waist w_0 will be at the centre of the cavity, and the Rayleigh distance of the TEM_{00} can be determined from:

$$R_c = 0.5L_c + \frac{z_R}{0.5L_c} \tag{4.24}$$

The TEM_{00} mode can be calculated using equation 4.13 and the q-parameters at the mirror surface and the cavity centre are:

$$q_m = \frac{L_c}{2} + iz_R \qquad \text{and} \qquad q_0 = iz_R \tag{4.25}$$

To achieve the best possible coupling to the TEM_{00} mode, and avoid coupling a proportion of the input light into higher order transverse modes, the q-parameter input beam must match the q-parameter of the mode. In practice this can be achieved by preparation of the input beam using a simple two lens telescope configuration, although in some cases, where significant reduction of the input beam is not required, a single lens system may be possible. An example two lens Keplerian telescope format is shown in 4.7 For high curvature mirrors it is important to account for the change in q-parameter associated with the lensing effect of the mirrors. Therefore, the $ABCD$-matrix representing such a mode matching system is a multiplication of the matrices representing the two lenses with focal lengths $f_1 \& f_2$, their separation d_2, the distance from the final

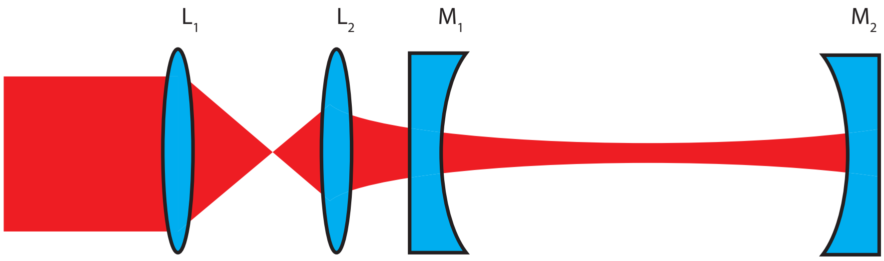

Figure 4.7: Example Keplerian telescope mode-matching set up.

lens to the back face of the mirror d_3 and the lensing effect of the mirror. The total $ABDC$−matrix is therefore:

$$\begin{bmatrix} A & B \\ C & D \end{bmatrix}_{MM} = \begin{bmatrix} 1 & 0 \\ \frac{n_m-1}{-R_c} & n_m \end{bmatrix} \begin{bmatrix} 0 & 1 \\ 1 & \frac{1}{n_m} \end{bmatrix} \begin{bmatrix} 0 & d_3 \\ 0 & 1 \end{bmatrix} \begin{bmatrix} 1 & 0 \\ \frac{-1}{f_2} & 1 \end{bmatrix} \begin{bmatrix} 0 & d_2 \\ 0 & 1 \end{bmatrix} \begin{bmatrix} 1 & 0 \\ \frac{-1}{f_1} & 1 \end{bmatrix} \begin{bmatrix} 0 & d_1 \\ 0 & 1 \end{bmatrix} \tag{4.26}$$

where d_1 represents the distance of the beam from the point where its q-parameter is known to the first lens in the mode matching system. For some applications a pinhole is also included at the focal plane between the lenses which acts to spatially filter the incident laser beam if the transverse profile does not match a fundamental Gaussian.

Most mode matching strategies will not achieve total mode matching (i.e. 100% of the incident light is held within the TEM$_{00}$ mode) but as will be discussed further below it is important that the coupling efficiency to the TEM$_{00}$ be far greater than any of the higher order modes, to ensure that only these modes meet the trigger threshold to initiate a ring-down measurement. To this end, an aperture may included intra-cavity, in order to induce loss to the more disperse modes.

4.4 Modes of Operation for cw-CRDS

Once the optical intensity within the cavity has built up to a suitable threshold level the ring-down time can be measured by preventing any further build up of intensity within the cavity [98]. There are several different operating strategies for measuring the ring-down time in cw-CRDS, with the majority of applications attenuating the incident

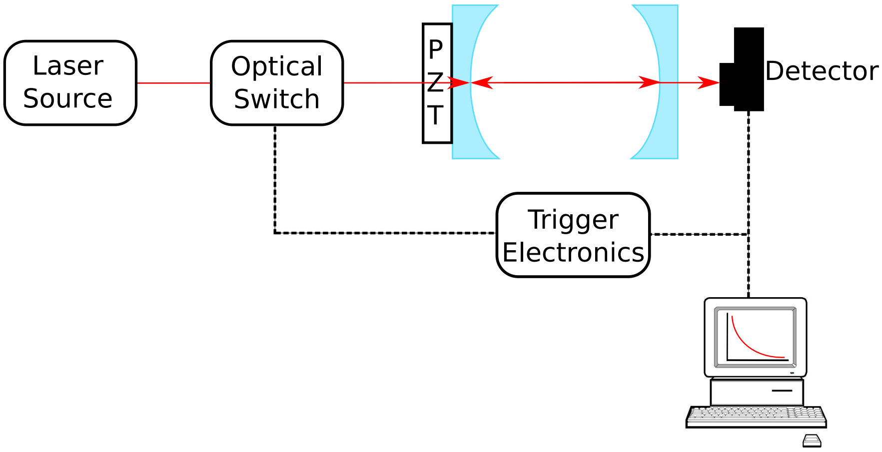

Figure 4.8: Typical cw-CRDS experimental setup, using optical shutter and piezoelectric transducer (PZT).

laser energy, for a given period, using some form of optical switch to allow the cavity to ring-down.

An example experimental setup for cw-CRDS is shown in figure 4.8. In this set-up the cavity length is scanned over a small distance (normally equivalent to just over $\Delta\nu_{FSR}$) exciting a longitudinal resonant mode of the cavity. When the voltage from the detector reaches a preset level the trigger electronics engage the optical switch to rapidly attenuate the incident laser light.

Another method was used by Orr et al [99] where, upon reaching the resonance threshold the cavity length was rapidly ($<< \tau$) scanned away from the resonance condition, thereby effectively attenuating all but a small residual amount of the input laser light. This approach has the advantage that it does not require any form of optical switch. Orr also successfully tested a similar approach by rapidly scanning the laser wavelength across the absorption feature of interest rapidly coupling and de-coupling across several cavity modes, producing a number of ring-down events.

4.4.1 Optical Switches in cw-CRDS

The optical switch used in the standard cw-CRDS approach usually takes the form of an acousto-optic modulator (AOM) which rapidly deflects the input beam away from the cavity. A less common method is to use a high speed electro-optic intensity modulator (EOM), a component used to encode data in optical fibre telecommunications. EOMs are widely available in fibre coupled packages, for applications at wavelengths around 1550nm (the telecoms C-band) . These modulators are able to operate in the GHz range, attenuating the incoming light on nanosecond time scales, this makes them attractive for cw-CRDS applications. Commercially available EOMs are typically fibre-based Mach-Zehnder interferometers with an electrically modulated (lithium niobate) phase delay applied to one arm. On recombination the phase difference leads to varying degrees of destructive interference, resulting in an output intensity modulation with attenuation of up to 40 dB. Huang et al. [100]. showed that for optimal performance the extinction requirement for cw-CRDS switches should be above 70 dB. In the same work Huang et al. demonstrated the first use of a semiconductor optical amplifier (SOA) as the optical switch, which performed comparably the more commonly used AOM. The use of a SOA has a particular advantage over EOMs and AOMs, which is that it is an active optical component which provides some amplification of the input laser light, where as the other options have insertion losses of typically $3-4$ dB associated with them. This is especially useful for applications which have a reasonably high broadband optical loss, as is encountered in flames, which will be discussed further in chapter 5. A further disadvantage of this type of modulator is that the output is dependent on the polarisation state of the input light, which necessitates the inclusion of a polarisation controller, on the input to the modulator.

4.5 The use of Pulsed versus CW Laser Sources

Both pulsed and cw laser sources are routinely used for CRDS, with each having its own benefits and disadvantages. The decision of which type of source should be used for a given application will, ultimately, be dictated by the availability of a source which emits at the absorption wavelength of the target species.

CRDS systems using pulsed laser sources are, normally, simpler to implement and are generally more robust in the presence of mechanical or optical disturbance as they do not rely on optical resonance to build-up power within the cavity. Pulsed CRDS by its nature does not require any attenuation of the incoming laser light in order to allow the cavity to ring-down, which provides the greatest simplification in the experimental set-up compared to cw-CRDS. In a pulsed CRDS system power is rapidly built up within the cavity as the pulse duration is typically much shorter than the ring-down time of the cavity. The pulsed operating mode can often be described using the simple 'Ping-pong' model were the duration of the laser pulse is shorter than the round trip time of the light within the cavity which results in no optical interference taking place. The light that is present at the start of the ring-down period is simply the proportion of light that is transmitted through the input mirror following the laser pulse, however as the peak power of pulsed sources is normally very high (on the order of MW) even this small proportion is easily detectable. For cases where the pulse duration is longer than the cavity round trip time there will be some overlap of the em-field within the cavity. The broad line-width which is normally possessed by pulsed sources is often much wider than $\Delta\nu_{FSR}$ which results in light being simultaneously coupled into several different longitudinal cavity modes which can reduce sensitivity (see section 4.3.3). The broad line-width of pulsed laser sources produces spectra which are a broadened convolution of the laser line-width and the absorption feature which must be accounted for in the data analysis. Another disadvantage in using pulsed laser sources is that such sources are typically much more bulky and expensive than the cw diode laser sources which are used for cw-CRDS.

4.6 Initial cw-CRDS Spectrometer Design

The initial design for a cw-CRDS spectrometer to be applied to in-situ measurements using the porous plug burner, described in chapter 3, follows the typical mode of operation described in section 4.4, using a piezoelectric transducer equipped mirror mount to vary the cavity length. A diagram showing the components, and optical and electrical connections of this initial design is shown in figure 4.9. In this section each of the main components of the spectrometer will be described individually, followed by an evaluation of the spectrometer performance under ambient conditions.

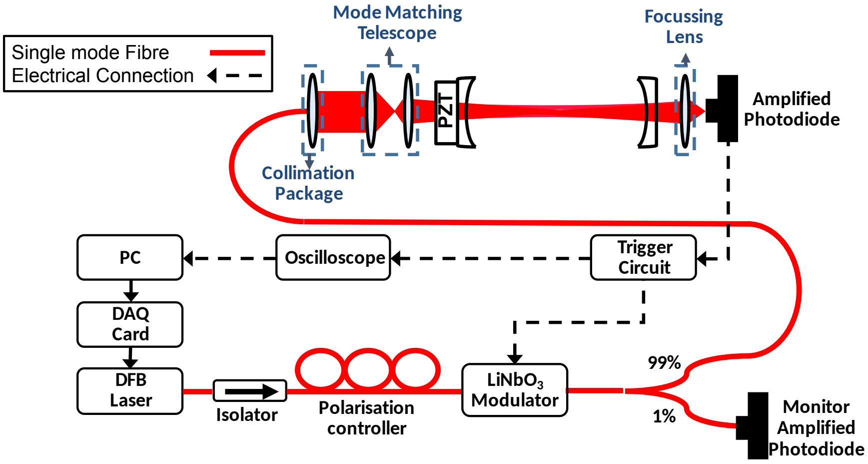

Figure 4.9: Initial cw-CRDS spectrometer design using $LiNbO_3$ intensity modulator.

4.6.1 Optical Cavity

As the spectrometer is primarily for in-situ combustion measurements, the optical cavity is constructed as an open path with a length of 0.5 m. The mirrors (CRD Optics) are 1 inch diameter and have a radius of curvature of 1 m, and are rated by the manufacturer to have a reflectivity in excess of 99.99% at 1550 nm. This design satisfies the stability condition described in section 4.3.2 (equation 4.21). The open path of the optical cavity, by its nature, exposes the mirrors to any dust or other contaminants present in the atmosphere, such as soot produced from the porous-plug burner. To protect the mirrors from becoming fouled, cover plates are installed over the surface of the mirrors, which have a 4 mm aperture in the centre. These cover plates also serve to induce loss in the higher order transverse modes.

The input mirror is mounted using a PZT equipped mirror mount (Thorlabs, model no. KC1-PZ/M), allowing the cavity length to be rapidly varied across several longitudinal modes. During operation the input mirror is continuously scanned over a distance corresponding to just over $\Delta\nu_{FSR}$ ensuring that at least one longitudinal mode is excited each scan.

The beam profile of the TEM_{00} mode through the cavity was modelled using WinLase software. This provided a beam diameter of 0.93 mm at the centre of the cavity (corresponding to a beam waist w_0 of 0.465 mm) and a rayleigh distance of 434.5 mm. The results of this model were confirmed using equations 4.13 and 4.24. The profile of the TEM_{00} mode determines the spatial resolution of the spectrometer, which is important for the measurement of concentration profiles in the flame. The near planar nature of the cavity ($g_1 g_2$ = 0.25) and long rayleigh distance of the beam ($z_R \approx L_c$ shows that the TEM_{00} mode is close to a collimated beam.

During operation the input mirror is continuously scanned over a distance corresponding to just over $\Delta\nu_{FSR}$ ensuring that one longitudinal mode is excited each scan.

4.6.2 Laser Source

The choice of laser source was based on the wavelength of an accessible acetylene absorption feature based on modelling the expected absorption spectra of the porous-plug burner using the HITRAN 2008 database (chapter 2) from which the p17e absorption feature at 1535.4 nm, previously used for in-situ detection by Wagner et al. [24, 55] was identified as being a suitable target.

The laser source is a tunable telecommunications distributed feedback (DFB) diode laser with a maximum output power of approximately 15 mW. The laser is encased within a fibre-coupled butterfly package, which directs the emitted light into SMF-28 single mode fibre. Within the laser package is an optical isolator, used to prevent optical feedback to the gain medium which could cause instabilities in the laser output.

The recovery of absorption spectra requires the laser wavelength to be scanned over the absorption feature(s) of interest with a suitable resolution. The laser has an emission wavelength in the region of 1535 nm and is able to be coarsely tuned through approximately 5 nm by adjusting the temperature of the diode through a peltier element contained in the laser package. The peltier element was controlled by a PID control unit (Thorlabs model number: TED200C). Fine wavelength tuning is achieved be changing the drive current supplied to the diode. To allow the performance of the system to be characterised without the flame present a second DFB laser emitting at ≈ 1548 nm can be used in place of the 1535 nm laser. This second DFB laser is able to access some weak features of H_2O present in the ambient air.

4.6.3 Mode Matching Optics

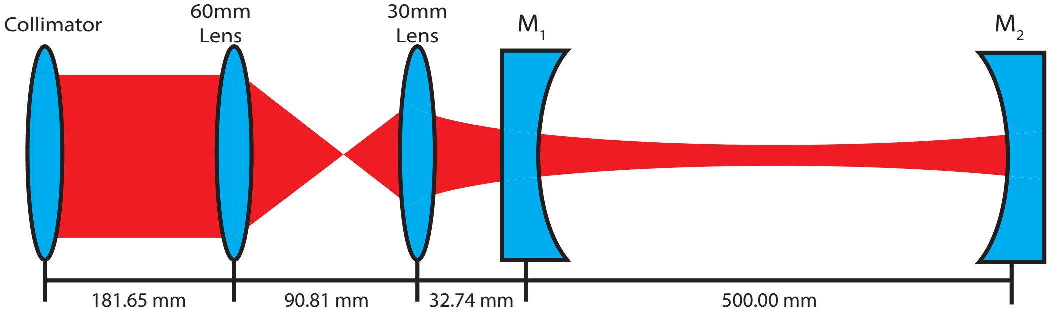

Figure 4.10: Separation distances for cavity and mode-matching optics (not to scale)

Mode-matching to the TEM_{00} mode is achieved using two, 1 inch diameter, biconvex positive spherical lenses (focal lengths 60 mm and 30,mm respectively) arranged in the basic Keplerian telescope format described in section 4.3.4.

To aid in the accurate mode matching to the TEM_{00} mode the q-parameter of the input beam at the point of collimation was determined by measuring the $1/e^2$ diameter of the beam using an automated knife-edge profiler (Manufacturer: Thorlabs). The profiler was translated linearly over a distance of 400 mm over which the diameter of the beam reduced by 164.08 μm, which indicates a convergence angle, θ_{conv} of 4.1×10^{-4} rad. This is used to estimate the waist size of the input beam $w_{0\,coll}$:

$$w_{0\,coll} = \frac{\lambda}{\pi \theta_{conv}} = 1.203\, mm \tag{4.27}$$

The Rayleigh distance for the output from the collimator, $z_{R\,coll}$ is therefore 2.932 m, calculated using equation 4.13. The radius of the beam was measured at the collimator lens w_{coll} to be 1.32 mm which allows the position of $w_{0\,coll}$ relative to the position of collimation lens, z_{coll} to be calculated using:

$$w_{coll} = w_{0\,coll}\sqrt{1 + \left(\frac{z_{coll}}{z_{R\,coll}}\right)} \qquad z_{coll} = 1.337\, m \tag{4.28}$$

and hence the q-parameter at the collimator surface, q_{coll} is:

$$q_{coll} = -z_{coll} + i z_{R\,coll} = -1.337 + 2.932i \tag{4.29}$$

Using equation 4.26 the separation of the optical components can be calculated to match the q-parameter at the cavity waist, by solving equation 4.26 using for d_1, d_2, and d_3, shown in figure 4.10. Due to the near-collimated nature of the TEM_{00} mode efficient mode matching can still be achieved if the spacing between the collimator and first lens, and the distance between the second lens and the input mirror, are different form those shown on figure 4.10 d_1 and d_3 providing the mirror separation d_3 is maintained.

4.6.4 Optical Switch and Trigger Electronics

Due to component availability and the convenience of fibre-coupling this initial design for the spectrometer used a $LiNbO_3$ intensity modulator. A 99:1 fibre splitter is used to monitor the output from the modulator. Through careful adjustment of the the bias voltage (provided by a standard 0 – 12 V bench top supply) and the polarisation of the input laser light, using the polarisation controller, the modulator can be configured to provide the greatest possible extinction ratio between its 'on' and 'off' states.

The voltage required to switch the $LiNbO_3$ modulator is provided using a small analog electronic circuit, which compares the photodiode voltage to a preset reference level. The circuit consists of a single printed circuit board (PCB) which contains 5 integrated circuits (ICs). The input signal to the circuit is first amplified using a high speed LM7171 op-amp, which has a gain of 10 and is wired in an inverting amplifier configuration. The output from this IC is then passed to a second LM7171 which is a second inverting amplifier with unity gain. The use of two inverting amplifiers provides linear amplification of the photodiode output. The next IC in the circuit is a LM311N comparator, wired in a Schmitt trigger configuration. This comparator compares the signal to a threshold voltage, set by a variable voltage divider. When the signal exceeds this value the comparator outputs 5 V. To interrupt the laser long enough for the cavity to ring-down the comparator is used to trigger a multivibrator IC, which holds a 5 V output for $\approx 200\,\mu$s. The final IC in the circuit is another LM7171 op-amp with variable gain which is used to ensure the output voltage from the circuit is sufficient to change the $LiNbO_3$ modulator from maximum to minimum transmission. The total time delay from the cavity transmission exceeding the preset threshold until termination of input light to the cavity is ≈ 40 ns.

4.6.5 Control and Data Acquisition

The nature of the cw-CRDS spectrometer requires a number of actions to be undertaken in the correct sequence. The required number of averages must be acquired on the oscilloscope (Tektronix), the data transferred to a PC and recorded, the wavelength of the laser incrementally adjusted, and the oscilloscope be reset for subsequent acquisition. LabView (produced by National Instruments) is a graphical programming language which is hardware orientated, with the manufacturers of measurement equipment often

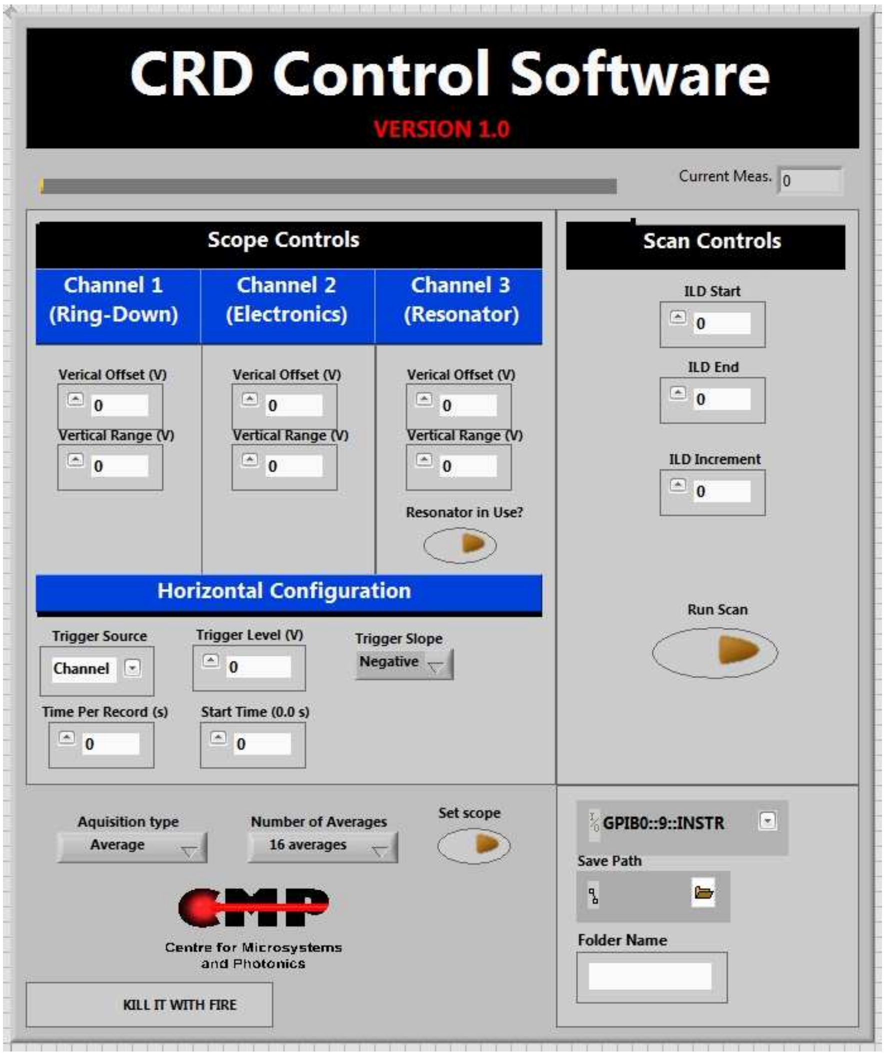

Current Meas. 0

Verical Offset (V) 0
Vertical Range (V) 0
Verical Offset (V) 0
Vertical Range (V) 0
Verical Offset (V) 0
Vertical Range (V) 0

Trigger Source Channel
Trigger Level (V) 0
Trigger Slope Negative
Time Per Record (s) 0
Start Time (0.0 s) 0

ILD Start 0
ILD End 0
ILD Increment 0

Aquisition type Average
Number of Averages 16 averages
GPIB0::9::INSTR

Figure 4.11: Front panel of the spectrometer LabView control program.

providing pre-made LabVIEW programming blocks. A LabVIEW program was developed to communicate with the oscilloscope via general purpose interface bus (GPIB) by adapting such programming blocks. The front panel of the control program is shown in figure 4.11. The laser wavelength was incrementally tuned by varying the current applied to the laser diode via current controller (ThorLabs, Model: LDC 210C), which is equipped with an analogue voltage input which can be used to control the output current with a conversion rate of 100 mA/V. The control voltage was provided by generating a DC level from the analogue output (AO) of a 16-bit data acquisition (DAQ) board (National Instruments, Model: PCI 6120) installed in the control PC. The oscilloscope is triggered to the interruption of the input laser using the same signal used to drive the EOM switch. This allowes the ring-down trace to be averaged accurately even if some of the excited modes do not build up enough intensity to trigger a measurement.

4.6.6 Optical Alignment Procedure

To achieve the greatest possible sensitivity, and to ensure that the majority of the incident laser light is coupled into the TEM_{00} transverse mode, the spectrometer optics require precise alignment. The procedure for the cavity alignment is detailed below:

1. The mounts used to hold the cavity mirrors are placed at the correct separation: 500 mm. The collimator, input mirror mount, and mode matching optics are mounted within a 30 mm optical cage system and translated to the correct separations. The angle of the collimator mount is adjusted to ensure that the beam passes through the centre of the optics.
2. Two IR florescent alignment discs are mounted in the cavity mirror mounts. The discs have a 1 mm hole drilled in the centre. The position of the output mirror mount is adjusted to ensure the beam is co-linear to the optical axis of the cavity.
3. The focusing lens and the photodiode are moved into position and aligned by maximising the signal on the detector.
4. An optical fibre circulator is installed between the $LiNbO_3$ modulator and the collimator, to measure the back reflection which will be used to align the cavity mirrors.
5. The output cavity mirror is mounted and the back reflection into the optical fibre is maximised to ensure overlap of the incident and reflected beams.
6. The input cavity mirror is mounted and the back reflection maximised.
7. The circulator is removed and the PZT is scanned through a distance of several wavelengths to excite a number of cavity modes.

8. The mirror alignment and mode matching optics are carefully optimised to maximise the cavity transmission from the TEM_{00} mode, whilst minimising any higher order modes.

4.7 Spectrometer Performance Evaluation

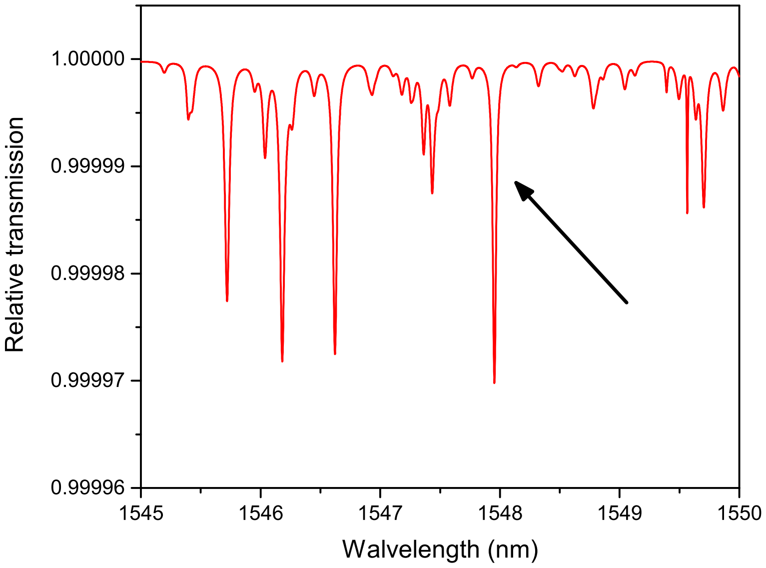

Figure 4.12: Model absorption spectra of 1.6% H_2O at ambient temperature for a pathlength of 500 mm.

The initial performance tests of the spectrometer were undertaken using the 1547 nm laser to measure an absorption feature of water at 1547.95 nm, shown on figure 4.12, which has a maximum fractional absorption of 3×10^{-5} for an ambient concentration (1.6%) at room temperature ($\approx 298\,K$) over the length of the cavity.

Although a detailed characterisation of the wavelength with drive current tuning was not undertaken for the 1547 nm laser, an approximate measurement of the wavelength was made using an optical spectrum analyser (OSA, Agilent Technologies) which provided settings for the TEC and current to scan across the correct feature. Figure 4.13

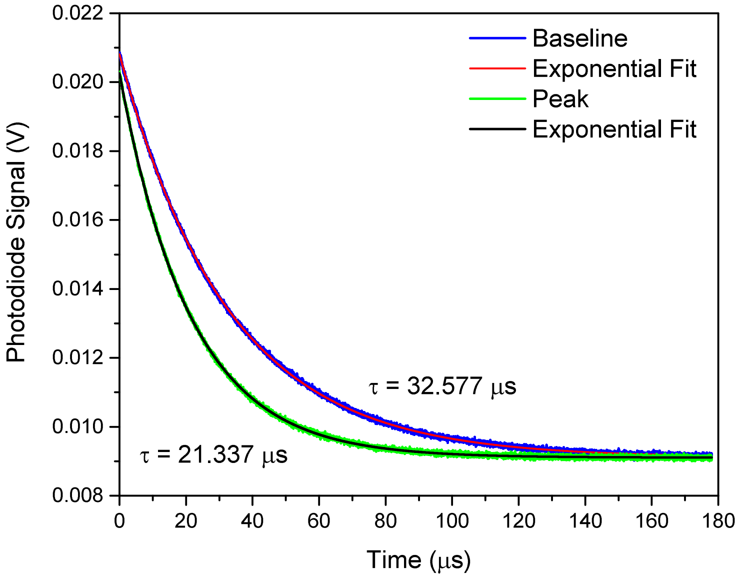

Figure 4.13: Comparison of ring-down traces taken at drive currents corresponding to the baseline and the peak of the absorption feature.

shows the average of 64 ring-down traces recorded at two drive currents, corresponding to wavelengths with minimal absorption, and at the peak of the absorption feature. The ring-down traces are shown with best fit exponential decays used to calculate the ring-down time. Using equation 4.5 the effective reflectivity of the cavity is calculated to be 0.99995 in this instance, which is above the manufacturer-quoted reflectivity for the mirrors. The fractional absorption at the peak of the feature measured this way is 2.695×10^{-5}. The close fit of the exponential decay curve indicates that the ring-down signal most likely a single exponential decay, with little transverse mode degeneracy.

By applying the data acquisition process detailed in section 4.6.5, tuning the drive current from 165 mA to 195 mA in 0.05 mA increments, the laser wavelength was scanned over the feature. A Matlab code was developed to carry out automated exponential fitting of the ring-down traces and the final result of this scan is shown in figure 4.14. Although the spectrometer has sufficient sensitivity to resolve this weak feature it is clear that one of the challenges faced by this initial design is that the finesse of the

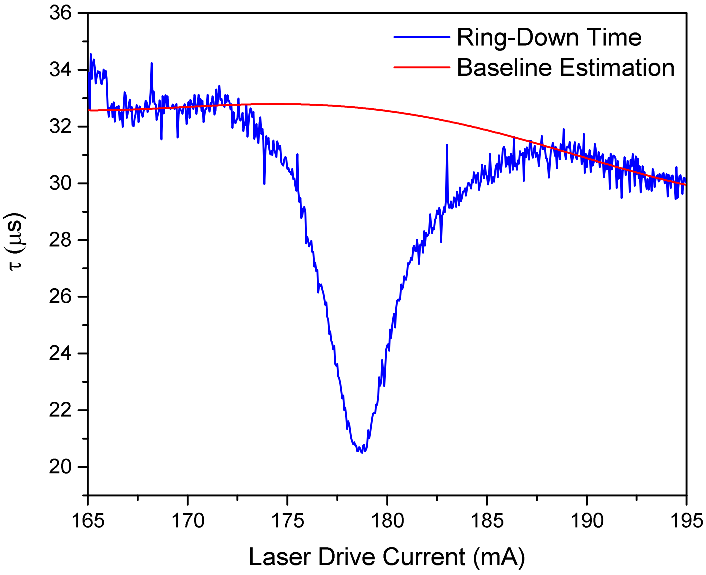

Figure 4.14: Ring-down time spectra of ambient water vapour feature.

degrade with time as the alignment degrades and the surface of the mirrors becomes fouled. The effect of this degradation is particularly evident in this high resolution scan and this could be limited in the future by increasing the drive current increment, and reducing the time required to record a spectrum. A feature of note in figure 4.14 is the rapid reduction in the cavity finesse at the start of the scan (drive current = 166 mA), This is potentially due to the presence of a small particle of dust landing on the mirror's surface, further highlighting the fouling problem faced by the open path cavity.

To quantify the minimum detectable absorption for the spectrometer an estimation of degradation to the finesse through the scan was made by applying a 4th order polynomial fit to the sections of the scan either side of the main feature which are free from significant absorption. This estimation was then used to normalise the scan, shown in figure 4.15.

The standard deviation of the noise in the area free from significant absorption is 6.117×10^{-7}, and hence the absorbance that can be detected (with an SNR of 3, or 3σ) is $3.670 \times 10^{-8}\,\mathrm{cm}^{-1}$. Although this detection limit compares favourably with single-

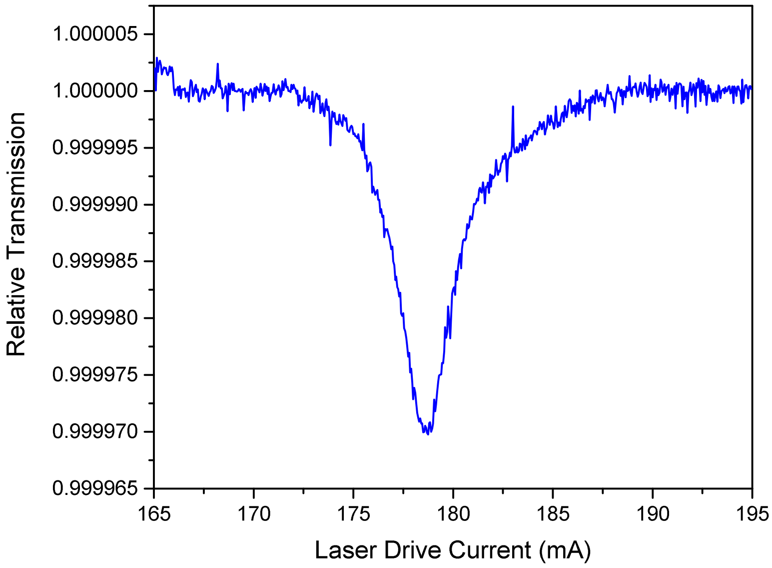

Figure 4.15: Normalised spectra of ambient water vapour feature.

pass absorption based techniques, which have a typical detection limit of $1 \times 10^{-5}\text{cm}^{-1}$ it is not particularly sensitive for cw-CRDS. Despite this the sensitivity is more than sufficient to successfully measure the p17e line of acetylene under the conditions within the porous plug burner.

4.8 Summary

In section 4.2 the principle for making absorption measurements from the lifetime of the light in an optical cavity was presented. The background theory and the design considerations for a stable optical cavity were presented and discussed in section 4.3. The outcomes from this discussion were then used to design an open-path cw-CRDS spectrometer to conduct sensitive absorption measurements in-situ in the porous plug burner. The initial design for the spectrometer was presented in section 4.6 and the performance was evaluated in section 4.7, where the minimum detectable absorption (3σ) was calculated to be $3.670 \times 10^{-8}\,\text{cm}^{-1}$.

5 cw-CRDS Combustion Measurements

5.1 Introduction

In chapter 1 The role that acetylene is understood to take in the current model for soot formation was presented. The need for accurate experimental measurements of species concentration under controlled conditions, which can be used to evaluate such models was discussed. The lack of in-situ measurements of acetylene was highlighted, which is thought to be due deficiencies in the capability of current in-situ measurement techniques.

In chapter 2 model spectra were shown which demonstrated the low, high temperature absorbance of acetylene in the near infra-red spectral region. Various optical measurement strategies were reviewed and the sensitivity and continuous-wave cavity ring-down spectroscopy showed promise for the detection of acetylene despite the novelty of its application for measurements in-situ in harsh combustion environments, such as flames. The initial design of the cw-CRDS spectrometer was presented in chapter 4. The spectrometer was designed with the aim of measuring the concentration profile of acetylene (C_2H_2) in laminar ethylene/air flames, with a range of fuel equivalence ratios. The flames are supported on the porous-plug burner presented in chapter 3. In this chapter the ability of the spectrometer to conduct such measurements is evaluated, and in in-situ concentration measurements of acetylene are presented.

In section 5.2 the suitability of the initial design of the spectrometer to recover absorption spectra in the porous-plug burner flames is evaluated. The outcomes from this evaluation are then used in section 5.4 to refine to the design of the spectrometer to overcome some of the difficulties posed by the introduction of the flame intra-cavity. Section 5.5 presents a detailed evaluation of the performance of the refined design. The recovered spectra are compared to spectra modelled using the Hitran/Hitemp databases

[51, 52]. Finally section 5.6 presents the development of an analysis strategy which adapts the spectra acquired using the spectrometer such that the model spectra can be fitted to determine the acetylene concentration.

5.2 cw-CRDS Spectrometer Adaptation to In-Situ Flame Measurements

The initial design of the cw-CRDS spectrometer was installed around the porous-plug burner, such that the TEM_{00} cavity mode would pass through the centre of the 33 mm diameter porous-plug. The burner was mounted on vertical stage which allowed the measurement position to be translated vertically through the flame whilst keeping the optical components stationary.

Initial measurements with the flame in-situ showed that bandwidth of the cavity mirrors was not sufficient to block the detector from errant flame emission. This emission produced significant variations in the detector output voltage, following even a minor disturbance to the flame. These voltage fluctuations were often greater than the trigger voltage level resulting in a high number of false acquisitions.

Figure 5.1 shows a comparison of the detector wavelength responsivity with the calculated Planck emission for a $1600\,K$ black-body (emissivity = 0.3), and the reflectivity range of the cavity mirrors. This comparison shows that only a narrow wavelength range of the errant emission, which falls within the detector response will be blocked by the cavity mirrors. To attenuate the remaining errant emission a 1550 nm centred, dielectric band-pass filter was installed between the output cavity mirror and the focussing lens ($\Delta\lambda = 40\,\mathrm{nm}$). The transmission response for this filter is also shown on figure 5.1, which is completely bounded by the cavity mirror reflectivity curve. The maximum transmission of the band-pass filter is only 57 % reducing to < 40 % at the target dectection wavelength of 1535 nm. This will have an adverse effect on the signal to noise ratio of the recorded ring-down measurements.

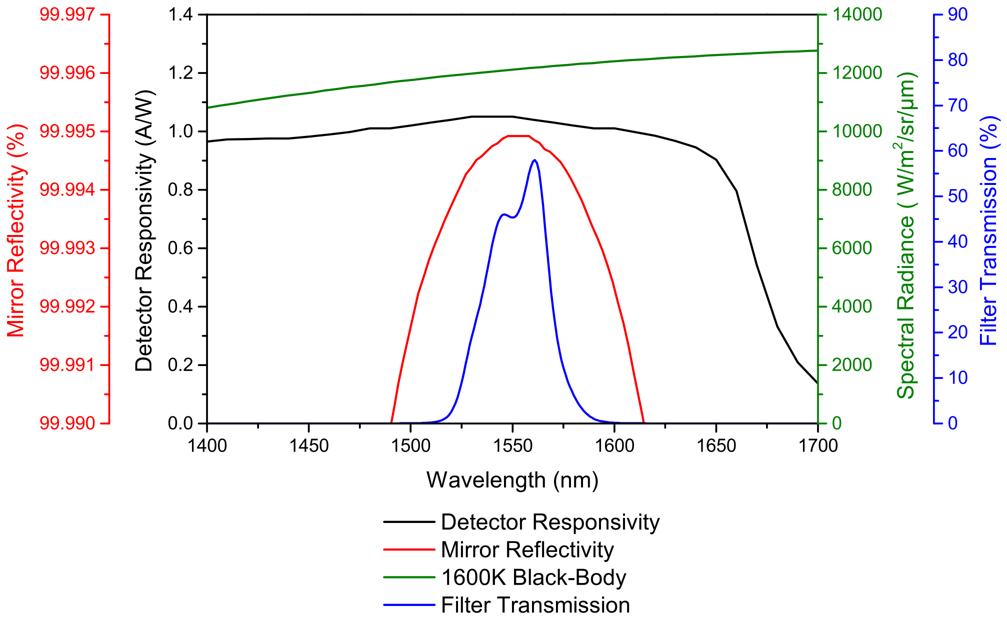

Figure 5.1: Spectral response of spectrometer components compared to radiance from $1600\,K$ black-body.

Although the design of the spectrometer is targeted towards measurements of C_2H_2 at around 1535 nm, the 1547 nm laser, which was used for the ambient water vapour tests, was initially used for the evaluation of the design for combustion measurements. The presence of the flame intra-cavity has a significant detrimental effect on the coupling efficiency of the laser into the resonant TEM_{00} cavity mode. This can be observed from the large reduction in on-resonance transmission and the reduced ring-down time of the cavity, indicating a significant increase in intra-cavity losses. Figure 5.2 shows a comparison of 32-averaged ring-down measurements made both in absence of a flame, and with a $\phi = 2.22$ flame, where the centre of the TEM_{00} mode is positioned $2\,mm$ above the surface of the burner. The laser drive current was set to $190\,mA$. To allow a for comparison the trigger voltage was reduced for the in-flame signal to maintain a comparable measurement repetition rate for both measurements ($\approx 5\,Hz$). As a consequence of the decreased transmission the gain on the photo-diode was increased form $30\,dB$ to $40\,dB$, to increase the SNR of the in-flame measurement.

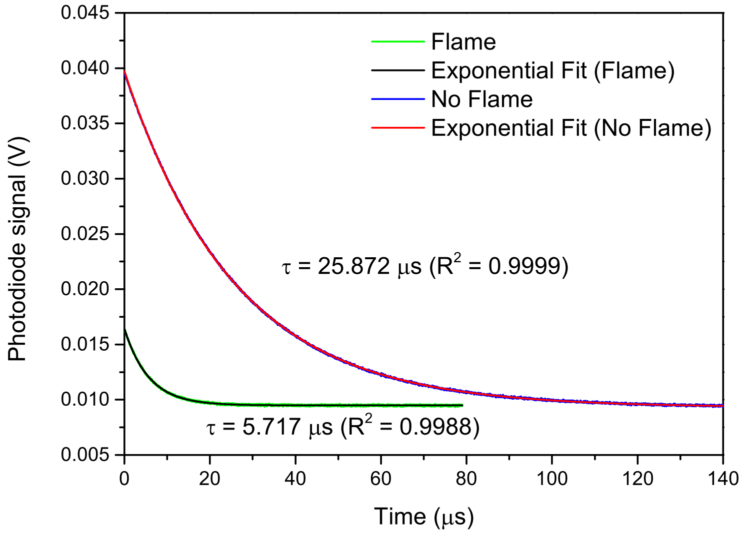

Figure 5.2: Comparison of averaged ring-down traces In absence of the flame (red) and $2\,mm$ above the burner in a $\phi = 2.22$ flame (detector gain $40\,dB$).

The measured ring-down time for the cavity before and after ignition of the flame is $25.872\,\mu s$ and $5.717\,\mu s$ respectively. If it is assumed that there is no significant absorption at this wavelength, this reduction in the ring-down time implies that the presence of the flame increases the intra-cavity loss, X in equation 2.1, by 1.61×10^{-4}. The source of this additional loss is thought to be due to perturbation of light resonating in the TEM_{00} mode, due to thermo-optical effects in the flame, causing beam steering, and thermal lensing [101] which could potentially direct light out of the TEM_{00} mode out of the cavity or into non-resonant higher order modes.

Figure 5.3 shows the ring-down time of the cavity as a function of the $1547\,nm$ laser drive current, with a $\phi = 2.22$ flame included in the centre of the cavity. The measurement location was $2\,mm$ above the burner surface. Several absorption features are apparent in the scan. Although the absorption features remain unidentified this initial test demonstrates the ability of the spectrometer to recover absorption spectra from species present in the flame despite the increased intra-cavity losses.

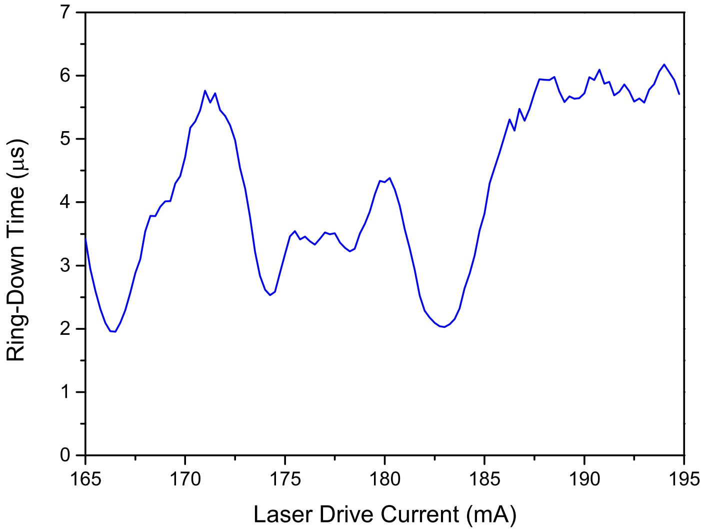

Figure 5.3: Initial current scan of 1547 nm laser. Recorded 2 mm above the burner in a $\phi = 2.22$ flame (0.25 mA resolution).

5.3 1535 nm Laser Wavelength Characterisation

Although the wavelength of the 1535 nm laser can me measured using an optical spectrum analyser, the wavelength resolution that can be achieved using tunable DFB diode lasers is much higher than can be measured by this approach. Therefore a different approach is required to assign a wavelength scale to the spectra acquired using the spectrometer. The techniques used to measure the wavelength tuning characteristics of DFB lasers using interference fringes have been described in detail previously [102] and the technique used by Johnstone et al. [103], using the output from a fibre ring-resonator to assign a relative wavelength scale to the applied drive current (for a given diode temperature) was used here.

A fibre ring-resonator is constructed using two fibre couplers, with one output from each coupler connected to the input of the other to form a ring cavity. The laser signal is supplied into the first coupler which couples a proportion of light into the ring, with the second coupler allowing a proportion of the light to be de-coupled from the ring.

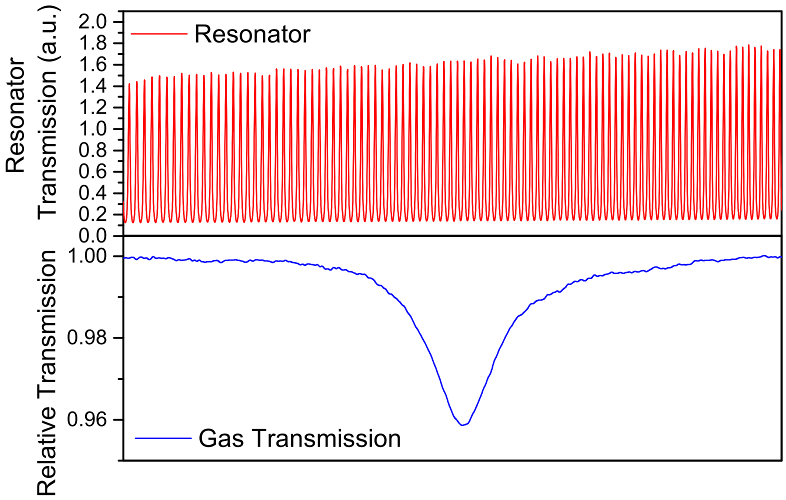

Figure 5.4: P17e absorption feature of 1% concentration C_2H_2 at room temperature, shown with resonator trace from 0.4275 GHz fibre ring-resonator.

The couplers in this case are akin to the mirrors of a linear cavity and hence when the longitudinal mode condition (equation 4.8) is fulfilled resonance is achieved. Resonant fringes will occur periodically as the wavelength of the laser is scanned. A relative frequency is then be derived by measuring the position of the transmission fringes through a wavelength scan of the laser as a function of drive current, and interpolating using a 4th-order polynomial fit based on the fringe positions.

The advantage of using the fibre ring-resonator in place of a free space optical cavity for wavelength characterisation is that the fibre ring-resonators generally are of lower finesse and hence possess a higher level of mechanical stability. The lower finesse also means that the fringes can be more easily resolved during the scan. In most cases the ring-resonator is constructed using single mode fibre therefore it will only support the TEM_{00} mode. Single mode operation removes any errors in the relative wavelength measurement occurring from fringes relating to higher order transverse modes. Although the free spectral range ($\delta\nu_{FSR}$) of the interference fringes provides only a relative frequency scale, by measuring a scan through the fibre-ring simultaneously with a transmission spectra of a known absorption feature, the scale can be converted to

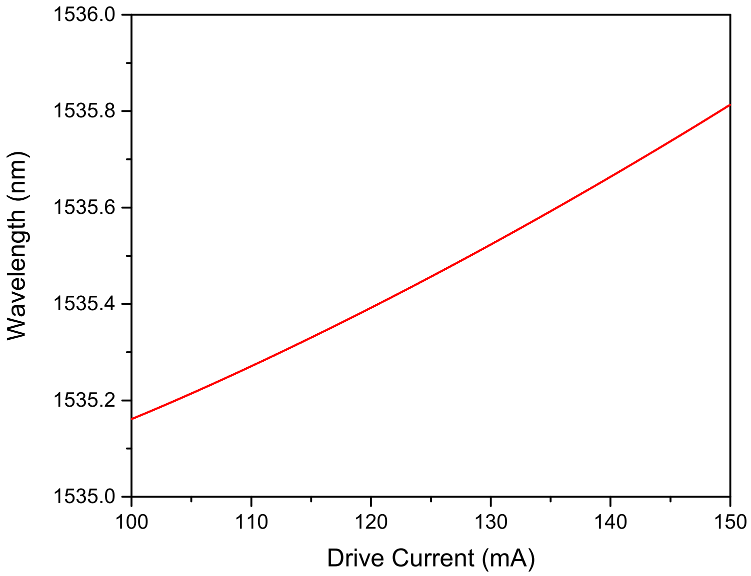

Figure 5.5: Wavelength tuning curve for the 1535 nm laser at a TEC thermistor setting of 14.024 $k\Omega$

an absolute wavelength scale. The point in the scan which corresponds to peak of the absorption feature is assigned the centre wavelength of the feature, provided in the Hitran 2008 database. Figure 5.4 shows the transmission spectrum of the P17e acetylene feature at room temperature ($\approx 298K$) at a concentration of 1% and the associated resonator trace used to determine the absolute wavelength scale of the scan. The free spectral range of the resonator used was $0.4275GHz$ Using this absolute wavelength scale a function which relates the drive current to the absolute laser wavelength, for a given diode temperature, can be prepared, which is shown in figure 5.5. This function is used to assign a wavelength scale to all spectra in this work measured using the 1535 nm laser, though in some cases the function is marginally offset to maintain the position of the peak of the absorption feature of interest.

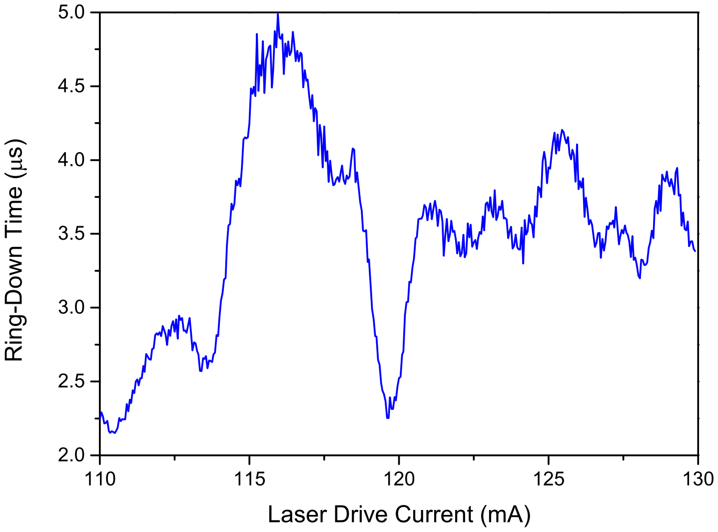

Figure 5.6: Initial current scan of 1535 nm laser. Recorded 2 mm above the burner in a $\phi = 2.22$ flame (0.05 mA resolution).

5.3.1 Initial Measurements of The P17e Acetylene Feature

The 1547 nm laser was replaced with the 1535 nm laser to interrogate the spectral region around the P17e acetylene feature. The wavelength characterisation was used to adjust the temperature of the laser diode such that the peak of P17e absorption feature ($\lambda = 1535.39\,nm$) would correspond to a drive current setting of $\approx 120\,mA$. Initially,the drive current of the laser was scanned from 110 mA to 130 mA, using a high resolution current scan with increments of 0.05 mA. The resulting spectrum is shown on figure 5.6. The P17e absorption feature can clearly be identified at the expected drive current of 120 mA. However, there is a large number of unidentified, interfering absorption features present. The high number of features presents the problem, as there appears to be no region of the spectrum that is free from absorption. Therefore the broadband losses (X) for the scan cannot be easily determined to allow for normalisation of recorded spectra. To enable comparison with predicted spectra modelled using HITRAN, the point on the spectrum with the maximum ring-down time (drive current $\approx 117\,mA$) was assumed to be free from any significant absorption, and was therefore used to approximately

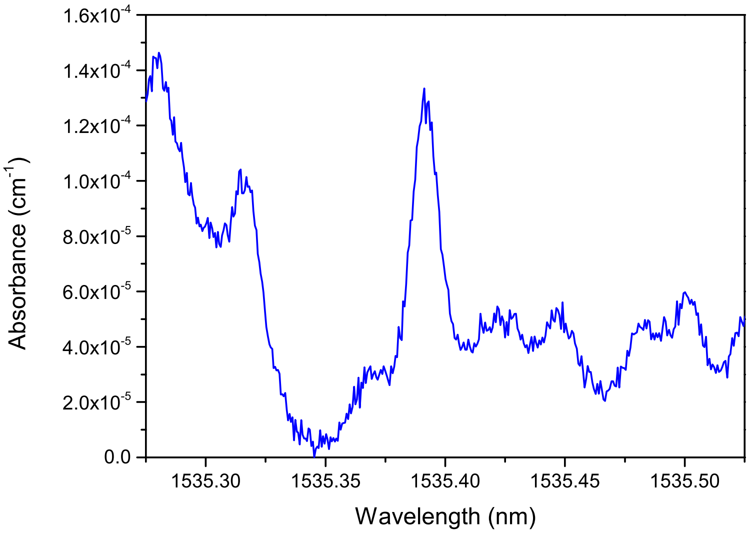

Figure 5.7: Comparison of initial flame spectra, normalised based on estimated broadband losses.

normalise the spectrum, which is shown in figure 5.7. Although several of the stronger unassigned absorption features are thought to be due to high temperature water, the majority are unassigned at this time. The complex nature of incomplete combustion and soot formation [8] means that there a high number of intermediate species that could be present at this position in the flame, some of which may have a contribution to the spectrum shown. Further variations in the acquired acetylene spectrum compared to the model could be because the database was not intended to be used at the elevated temperatures encountered in the flame.

5.4 Refinement of Spectrometer Design to Improve In-Situ Flame measurements

The initial design for the cw-CRDS spectrometer was capable of resolving the P17e acetylene feature, though the initial in-situ tests revealed a number of problems which limited the usefulness of this design for undertaking measurements of the concentration

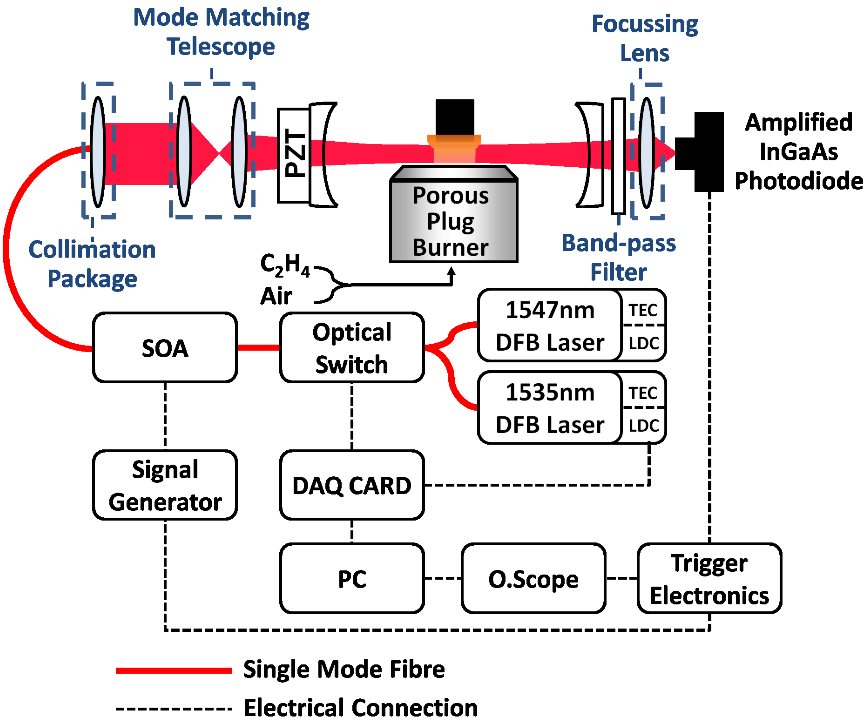

Figure 5.8: Refined cw-CRDS Experimental Set up: SOA, Semiconductor Optical Amplifier; DAQ Card, Data Acquisition Card; TEC, Thermoelectric Controller; LDC, Laser Diode Controller.

of acetylene. Firstly the reduction of the on-resonance transmission of the cavity following ignition of the flame, which required a reduction in the trigger voltage to make measurements. Even with this reduced trigger voltage, the spectrum shown in figure 5.6 had an acquisition time of over 50 minutes requiring an average of 7.6 s integration time per data point. This resulted in an approximate repetition rate of 4.2 Hz, based on 32 averages. As detailed in chapter 3, using richer flame conditions for this length of time would result in a large build up of soot particulate on the stabilisation plate, thereby limiting the total number of ring-down measurements that could be taken and hence the resolution of the resulting spectrum. Secondly the spectra could not be properly normalised due to the large amount of interfering features. To overcome these challenges refinements were made to the initial design of the spectrometer.

A detailed diagram of the updated spectrometer is shown in figure 5.8, which includes several additional components to reduce the impact of the detrimental effects encountered with in-situ operation in the flame. Each change to the design will be presented in this section.

5.4.1 Semiconductor Optical Amplifier

In chapter 4 the potential use of a semiconductor optical amplifiers (SOA) to initiate the cavity to ring-down was discussed. A C-band SOA (manufacturer: Kamelian) was used in place of the $LiNbO_3$ intensity modulator, as it is able to provide amplification increasing the optical power coupled into the cavity, thus improving the overall SNR of the recorded ring-down trace. The SOA was powered and controlled using an arbitrary function generator (manufacturer: Agilent Technologies) which supplied a DC level of 10 V corresponding to a drive current of approximately 200 mA. When the 1535 nm is used as the input wavelength for the SOA produced a total output power of $\approx 20\,m$W, which was measured using an optical power meter. When cavity transmission reached the trigger threshold, the output voltage of the function generator was reduced to 0 V (edge time 5 ns), providing over 80 dB of attenuation. The 0 V output from the function generator maintained a period of 200 μs, which was sufficient to allow the cavity to fully ring-down. Figure 5.9 shows a comparison of ring-down measurements using the SOA and $LiNbO_3$ modulator, taken 2 mm above the surface of the burner in the $\phi = 2.22$ flame. The increased photo-diode signal when using the SOA requires the photodiode gain to be reduced to 20 dB. The measurement made using the SOA has normalised for gain to 40 dB to allow a direct comparison with the $LiNbO_3$ modulator measurement which required a pre-amplifier gain of 40 dB. This comparison demonstrates the increased intensity of the on-resonance cavity output when the SOA is used. It should be noted that the slight difference in the ring-down time between the two measurements is probably due to varying the broadband intra-cavity losses (mirror fouling/alignment drift), as these measurements were not taken in immediate succession.

A further advantage of replacing the $LiNbO_3$ modulator with an SOA is that it removes any sensitivity of the fibre system to polarisation, which had the potential to

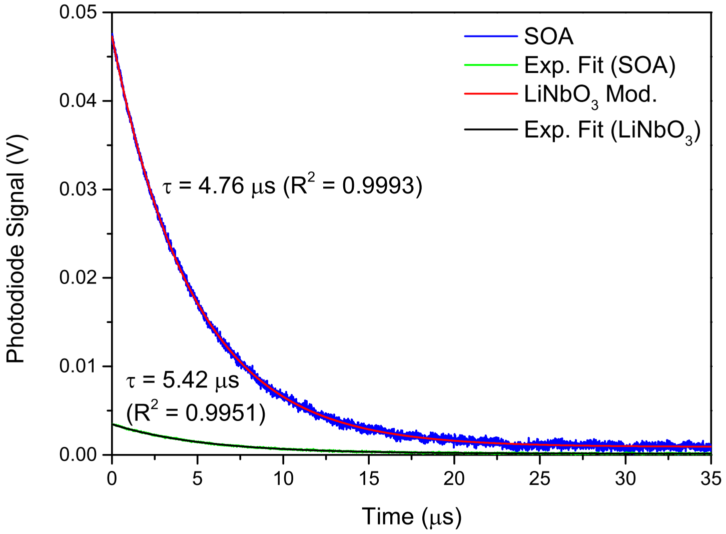

Figure 5.9: Comparison of ring-down traces with the laser attenuated using the SOA and $LiNbO_3$ intensity modulator. The SOA trace is rescaled to compensate of a $20\,dB$ reduction in pre-amplifier gain.

drift during the scan period (i.e. due to any mechanical disturbance to the optical fibres). It was therefore possible to remove the input polarisation to the modulator, there by reducing optical loss in the fibre system. The standard deviation of the 32 individual ring-down traces has been measured to be $0.132\,\mu$s. For the 1547 nm laser, which is equivalent to 3% of its average ring-down time.

5.4.2 Trigger Electronics

The increase in the on-resonance cavity transmission, afforded by the SOA, removes the requirement for a separate trigger circuit. The signal generator used to control the SOA has the option to accept an external trigger signal to control the voltage supplied to the SOA. This external trigger input is designed to operate with a standard 5 V TTL signal, but will trigger using any short rise time pulse that exceeds 2.5 V. In place of the trigger circuit used in the original spectrometer design a high speed linear amplifier was included to amplify the output of the photodiode such that it exceeds the 2.5 V trigger level when the build up of light in the cavity is sufficient for a ring-down measurement. Removing the analog trigger circuit simplifies the design, and adds a further degree of robustness to the spectrometer, by using only commercial grade equipment for the trigger process. The only disadvantage of this new approach is that the trigger level must now be set by adjusting the gain on the amplifier (and photo-diode pre-amplifier) which limits the trigger level to a range of discreet settings dictated by the available combinations of amplifier gain settings.

5.4.3 Signal Normalisation Using Two Wavelength Approach

The spectrum acquired using the 1547 nm laser, shown in figure 5.3, appears to have a region free from any significant absorption features at the wavelength corresponding to laser drive currents of ≈ 195 mA. Figure 5.10 shows a further scan of this region, where the wavelength of the laser has been slightly shifted by adjusting the diode temperature. The region of reduced absorption appears to lie between two strong features and there may be some overlap with the wings of these features. Although a small amount of absorption may also be present in this region, this absorption is much less than the P17e feature and hence they will only introduce a minor error in the absorption measurement. This region of reduced absorption was then targeted as a suitable point from which the broadband losses in the system could be calculated, allowing the measurements taken with the 1535 nm laser to be normalised. This was achieved by including an optical switch in the spectrometer prior to the SOA, and switching between the two lasers to seed the SOA alternately, ring-down measurements can be recorded at both wavelengths. With calibration for the slight variation in mirror reflectivity (2.4% reduction in ring-down time) due to the change in wavelength, the effective reflectivity ($\mathcal{R}_{eff}$) of the cavity can be determined. This allows the spectra acquired with the 1535 nm laser (the wavelength of which is scanned across the wavelength region of interest) to be normalised. Alternately switching between the lasers also solves the problem reported in chapter 4, where the effective reflectivity of the cavity was observed to degrade during

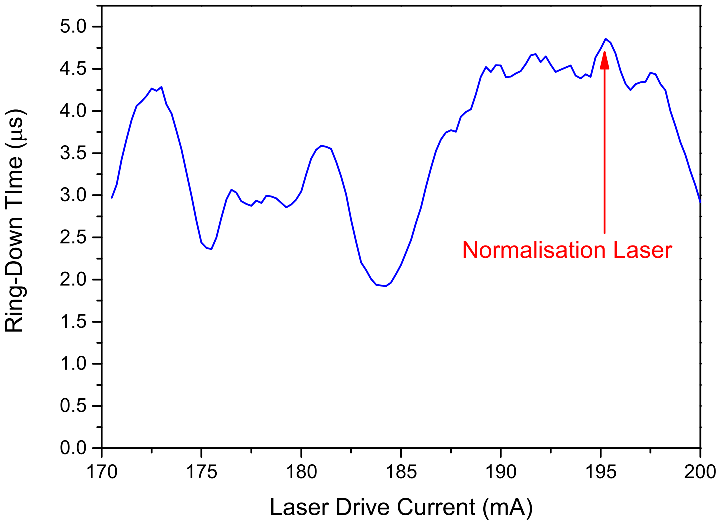

Figure 5.10: Ring-down time spectrum from current scan of 1547 nm laser with small temperature shift. Recorded 2 mm above the burner in a ϕ = 2.22 flame (0.25 mA resolution)

the scan, as this is now measured following every acquisition. The LabView program controlling the spectrometer was adapted to control the position of the optical switch using the digital outputs from the DAQ card, Figure 5.11 shows the amended workflow diagram for the LabView program. To carry out the normalised in-flame CRDS measurements the 1535 nm interrogation laser is current tuned using the DAQ board as before, acquiring and averaging the required number of ring-down traces at each current setting. However, between each drive current increment of the interrogation laser, the LabView program triggers the optical switch to shift to the 1547 nm normalisation laser, again acquiring and averaging the required number of ring-down traces. The LabView program then switches back to the interrogation laser and increases the drive current by one current increment. The process is then repeated until a spectrum has been recorded over the desired wavelength range.

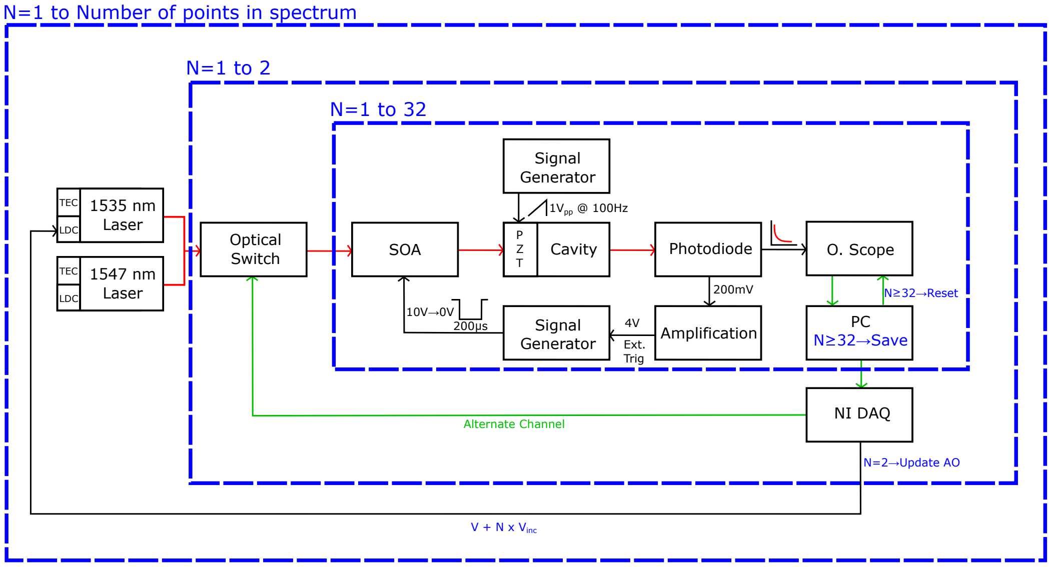

Figure 5.11: Work-flow diagram for spectrometer control LabView program, expanded to include optical switch.

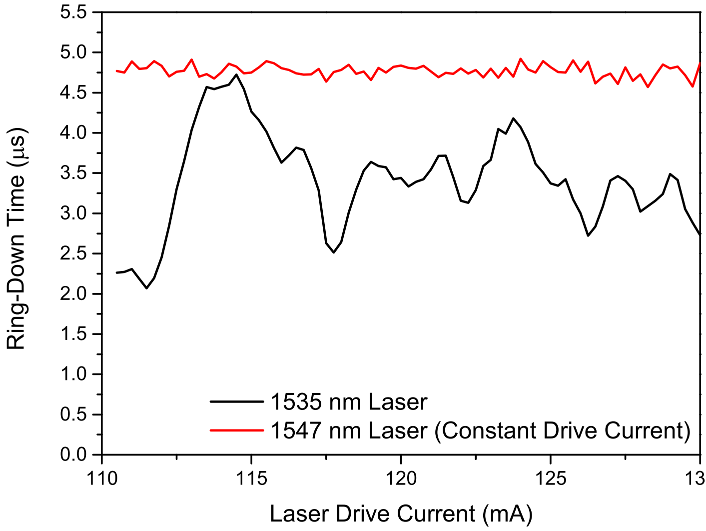

Figure 5.12: Example of ring-down time flame spectrum for 1535 nm interrogation and 1547 nm normalisation laser (held constant at 195 mA)

5.5 Spectrometer Performance Evaluation

Figure 5.12 shows a typical raw acquisition taken using the two wavelength approach, recovered 3 mm above the burner surface in a $\phi = 2.07$ flame, using the new spectrometer design. In this case, the drive current of the interrogation laser has been scanned in 0.25 mA increments, which corresponds to an average wavelength change of 3.6 pm. As with the initial combustion measurements an average of 32 ring-down traces was recorded at each current increment, and also for the normalisation laser, which was held constant. The standard deviation in the un-averaged ring-down times was measured to be 0.132 μs for the normalisation laser (approximately 3% of its average ring-down time).

The time taken to complete the scan shown in figure 5.12 was approximately 8 minutes with an average acquisition time of 3 s per data point, implying that individual ring-down measurements occurred at a rate of 10.67 Hz, which is a significant improvement over the initial design. There is a disadvantage to the new approach however, as each absorption measurement requires an associated measurement at the normalisation point. Despite the increased number of data points the overall acquisition time for a spectrum is still reduced using the refined design due to the increased cavity output intensity using the SOA. Figure 5.12 also shows that the normalisation laser ring-down time does drift at a rate estimated to be approximately $1 \times 10^{-4}\,\mu$s/s. It is assumed that this drift is due to degrading mirror reflectivity and/or alignment, and is also present at the same rate in the interrogation laser measurements. The drift is therefore negated by measuring the effective reflectivity of the cavity using the two laser approach. In practice extended operation of the cavity inevitably leads the finesse to degrade to a point where the quality of the recorded spectra is effected, during normal operation the spectrometer could typically be operated for three consecutive days. After this point the mirrors required to be removed for cleaning necessitating the realignment of the cavity optics.

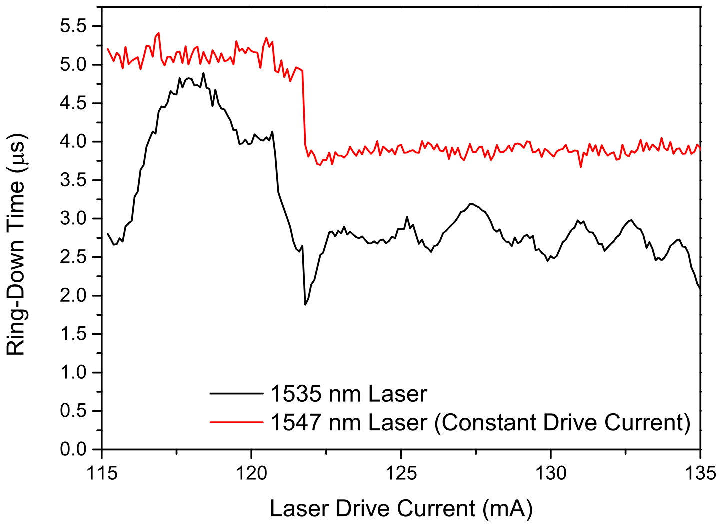

Figure 5.13: Example of raw ring-down time flame spectrum including a mid-scan drop in finesse.

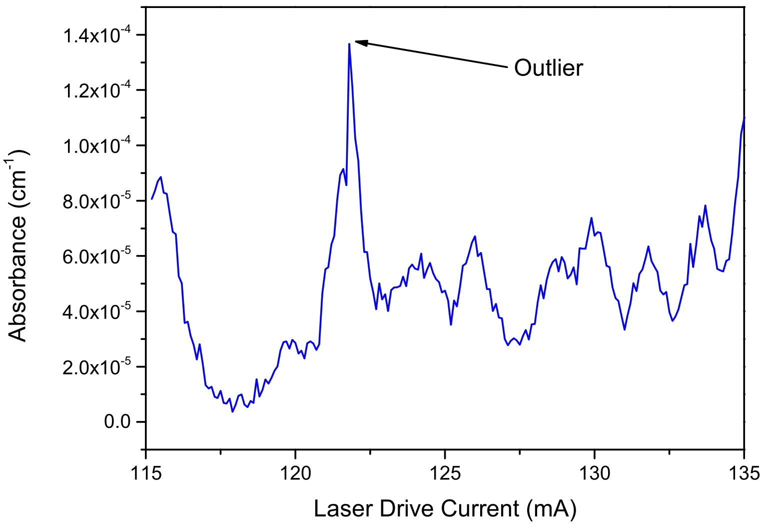

Figure 5.14: Example of normalised flame spectrum including a mid-scan drop in finesse. (outlier identified)

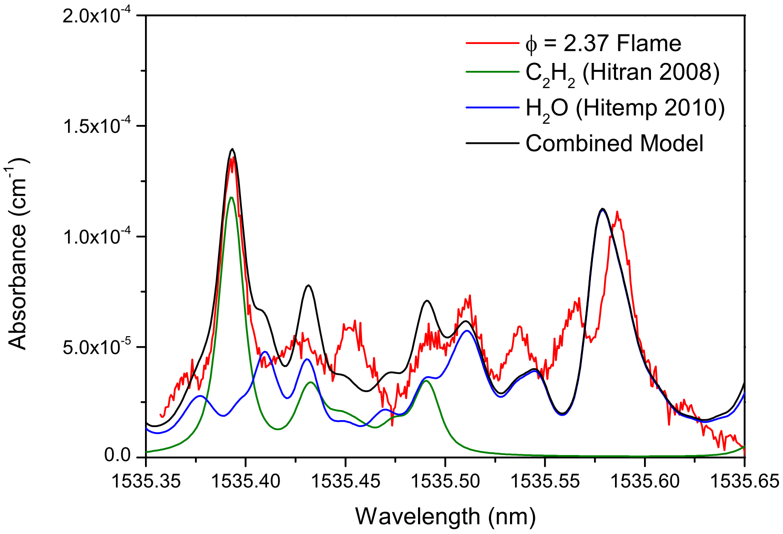

Figure 5.15: Normalised high resolution (0.05 mA increments) flame spectrum, recorded 3 mm above the burner in a $\phi = 2.37$ flame.

Parameter	Value	Units
Temperature	1600	K
C_2H_2 Concentration	1.22	%
H_2O Concentration	7	%
Pressure	1.013	bar
Path-length	3.4	cm

Table 5.1: Input parameters for Hitran 2008 model.

Figure 5.13 shows another higher resolution scan during which the effective reflectivity of the cavity is sharply decreased, likely due to particulate fouling of the mirrors. When this spectrum is normalised, shown in figure 5.14, the two laser method is robust enough to correct for even such sharp decrease in ring-down time, albeit with an outlying point immediately following the decrease. Figure 5.15 shows a normalised spectrum taken at a higher resolution, at a position 3 mm above the burner surface in a $\phi = 2.37$ flame. . In this measurement the interrogation laser was scanned over a larger wavelength range to aid in the identification of the unknown absorption features, revealing a second large feature, which can be assigned using the HITEMP 2010 database as water. Figure 5.15

also shows the modelled spectra of C_2H_2 and water (which was introduced in in chapter 2), highlighting the discrepancy between the model and the experimental spectra, even when high temperature water is included in the model. The input parameters used for the model are shown on table 5.1. This discrepancy between the measured and modelled spectra will introduce an error in the concentration values recovered from the fitting process, which will be discussed further in section 5.6

The signal to noise ratio (SNR) for the P17e acetylene feature was calculated to be approximately 31 for this spectrum, and was calculated by comparing the standard deviation of the absorbance measurement at the peak of the P17e absorption feature and comparing with an estimation of the average absorption at the peak, which was determined from a third order polynomial fit applied over 20 measurements at the peak of the feature. The measured absorbance at the peak of the P17e feature is $1.3 \times 10^{-4}\,\mathrm{cm}^{-1}$ at this position in the $\phi = 2.37$ flame. This leads to a measurement sensitivity of $1.2 \times 10^{-5}\,\mathrm{cm}^{-1}$ based on the sensitivity limit being 3 times the standard deviation of the absorption measurement.

5.5.1 Cavity Mode Structure

The beam steering and thermal lensing effects caused by the flame are thought to direct light out of the fundamental TEM_{00} mode, and direct the light into higher order transverse modes with each successive round trip. As was discussed in chapter 4 each of the higher order modes will have a different ring-down time, which will introduce error in the absorption measurement.

Figure 5.16 shows the result of scanning the cavity length a short distance ($\approx \Delta\nu_{FSR}$) using the piezoelectric mirror mount. The design of the mode-matching optics and careful alignment of the cavity mirrors couples the majority of the input laser-light into the TEM_{00}mode. This is evident from the high transmission when this mode is resonant compared to the inter-spaced higher order transverse modes, the majority of

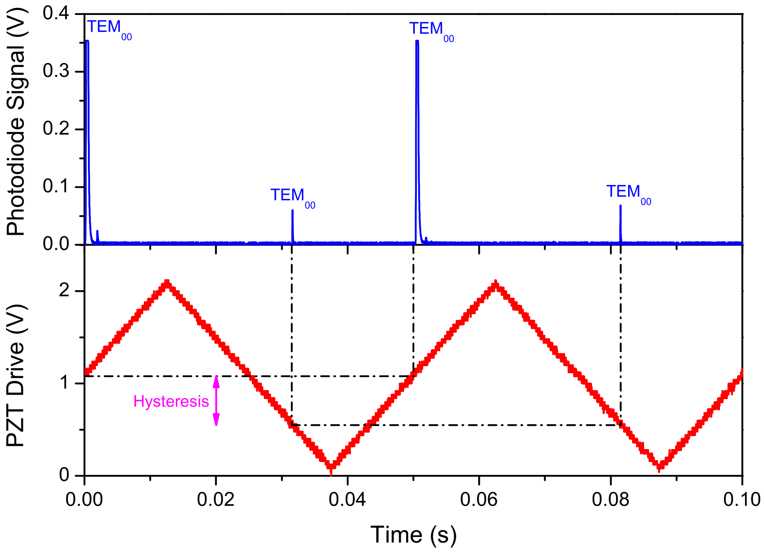

Figure 5.16: Example of cavity output recorded for a cavity length scan (in absence of the flame).

which are not visable on figure 5.16. The difference in output intensity of the TEM_{00} mode between the different directions of the piezo mount sweep is thought to be due to a slight change in alignment associated with the change in direction. The temporal spacing of the cavity modes is also slightly offset in each direction due to the mechanical hysteresis of the piezo mount.

Figure 5.17 shows the same scan of the cavity length where the centre of the TEM_{00} mode, is positioned 3 mm above the burner in a $\phi = 2.37$ flame. Aside from the previously observed reduction of the peak transmission of the TEM_{00} mode there is a marked increase in both the transmission and number of observable inter-spaced higher order modes. This change in the mode structure supports the assumption that a proportion of the light is directed into these modes, with the remainder lost due to any residual broadband absorption and/or scattering losses due to the presence of particulate. Despite the increase in the transmission of the higher order modes the TEM_{00} mode still remains the preferentially excited mode, with the other modes remaining below the trigger level.

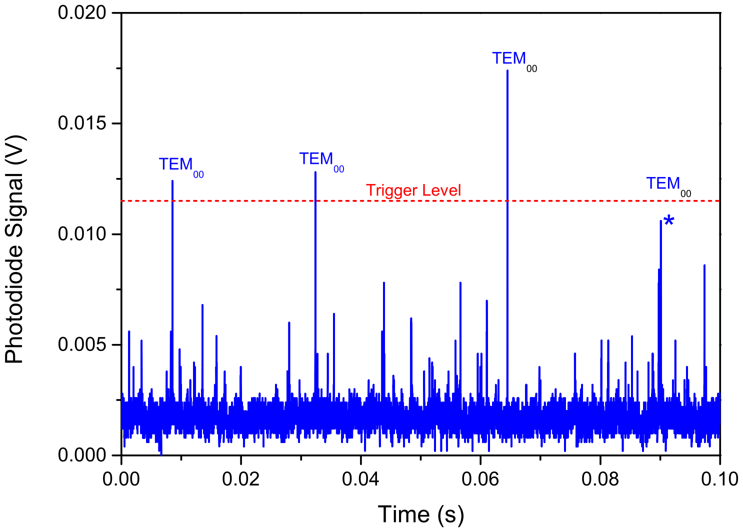

Figure 5.17: Example of cavity output recorded for a cavity length scan with flame ignited.

To reduce the probability of false triggering, the trigger voltage is set relatively high. However, using such a high trigger level reduces the measurement repetition rate as the instabilities introduced from the flame can reduce the on-resonance transmission of the TEM_{00} mode below the trigger level, and therefore a measurement will not be triggered every time the resonant conditions are met. This is shown on figure 5.17 where the resonance denoted with '*' fails to reach this level, and would therefore not be included in the integration of the ring-down time measurement.

One of the concerns with including an additional active optical component, such as an SOA, in the design, is the introduction of noise due to amplified spontaneous emission (ASE), an unwanted broadband emission resulting from the amplification. When the output wavelength of the SOA is not controlled with one of the DFB lasers, the power output of the ASE was reduced to $\approx 4\,\mathrm{mW}$ ($\approx 20\%$ of the output when controlled using a DFB laser), which is distributed across its entire gain region. Figure 5.18 shows the same scan of the cavity length, where the cavity is pumped using only the ASE from the SOA.

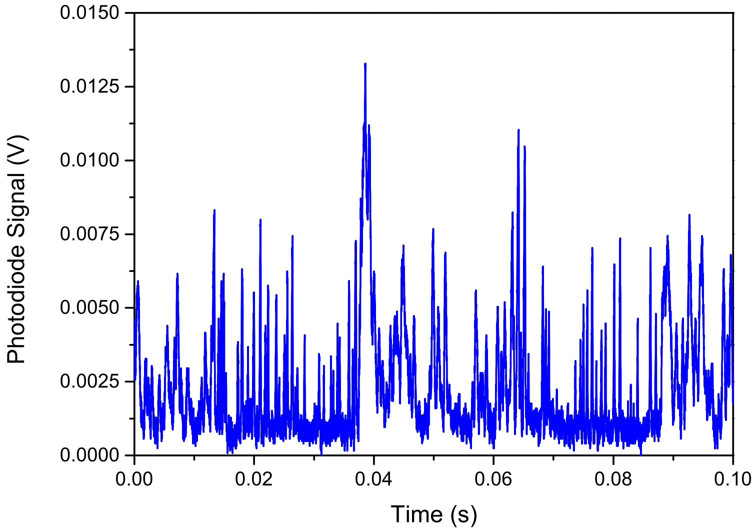

Figure 5.18: Example of cavity output recorded for a cavity length scan with the ASE from the SOA.

The spontaneous nature of ASE means that it is generally incoherent. However, due to the broad range of phases emitted a proportion of the light will have a degree of coherence, which results in random build up in the cavity. As the efficiency of the mode-matching optics has been shown to be high, the vast majority of this light is held within the TEM_{00} mode. Comparing this random excitation of the cavity to the well defined mode structure shown in figure 5.16 implies that when the SOA is controlled using the DFB laser there is little contribution of the ASE to cavity resonance compared to the coherent light. Despite the random nature of the resonance using just the ASE from the SOA a stable ring-down trace can be recorded (figure 5.19), with a ring-down time that is of the same order as when the SOA is controlled with a laser.

5.5.2 Ring-down time vs. Height above burner

Using the assumption that no significant absorption occurs at the normalisation laser wavelength, the broadband loss due to the presence of the flame can now be evaluated across a range of equivalence ratios and flame positions. As was discussed in chapter

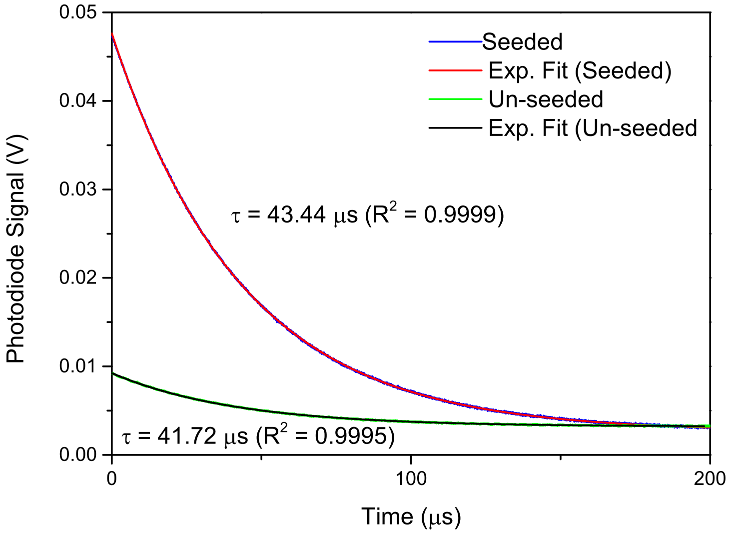

Figure 5.19: Comparison of ring-down measurements with the SOA with and without input light from the 1535 nm laser.

3, the formation of particulate soot is thought to begin at a distance between 5 and 8 mm above the burner surface. The presence of particulate intra-cavity would cause an increase in the broadband losses, which could limit the sensitivity of the spectrometer at these positions in the flame. Similarly the strong thermal gradients known to exist lower in the flame, close to the flame front, will increase the broadband loss intra-cavity.

Figure 5.20 shows the measured ring-down time as a function of height above the burner for a range of flame conditions. These measurements were taken using the 1547 nm laser tuned to the normalisation wavelength, marked on figure 5.10. Aside from showing the limitations of cw-CRDS as a measurement technique, with regards to measurement position, this data also provides useful into particulate formation and flame-front position. There is increased attenuation due to the presence of soot at positions above 7 mm from the burner, In agreement with the photoacoustic (and previous laser induced incandescence) measurements presented in 3. However, the cw-CRDS results also show attenuation lower at lower positions in the flame for the higher equivalence ratios, showing attenuation from 4.5 mm above the burner. This supports the

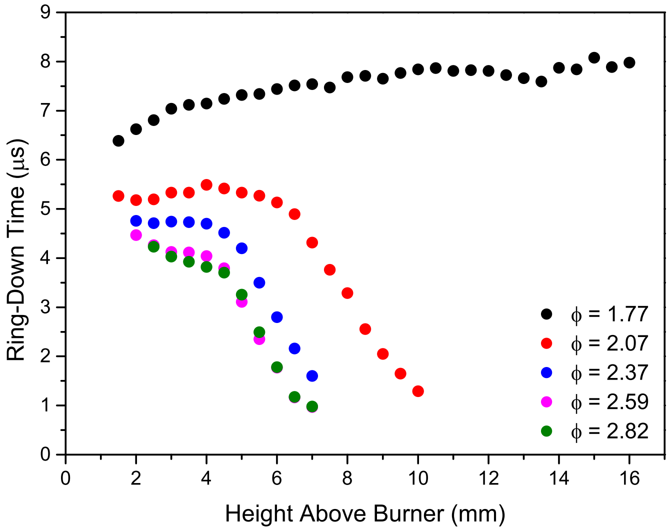

Figure 5.20: Ring-down time compared to height above the burner for the 1547 nm laser tuned to the normalisation point.

explanation for the increased Planck emission at this position, providing a further indication of the presence of small nascent particles, which the other techniques may lack sufficient sensitivity to measure.

As the equivalence ratio is increased there is an increase in the broadband attenuation at all positions above the burner surface. The lowest point in the flame at which resonance could be supported within the cavity becomes elevated as the equivalence ratio is increased. This is consistent with the flame-front position elevating from the burner, with the steep thermal gradients in this region likely responsible for the increased intra-cavity losses.

Figures 5.21 and 5.22 show ring-down time spectra recorded at 1 mm increments above the surface of the burner in the ϕ = 1.77 and ϕ = 2.59 flames respectively. The spectra recorded using the higher equivalence ratio flame do not show a significant change in shape with height above the burner, other than an increase in the broadband attenuation from 5 mm upwards. This indicates that there is likely no significant change in the composition with height above burner. This is in contrast with the lower equiv-

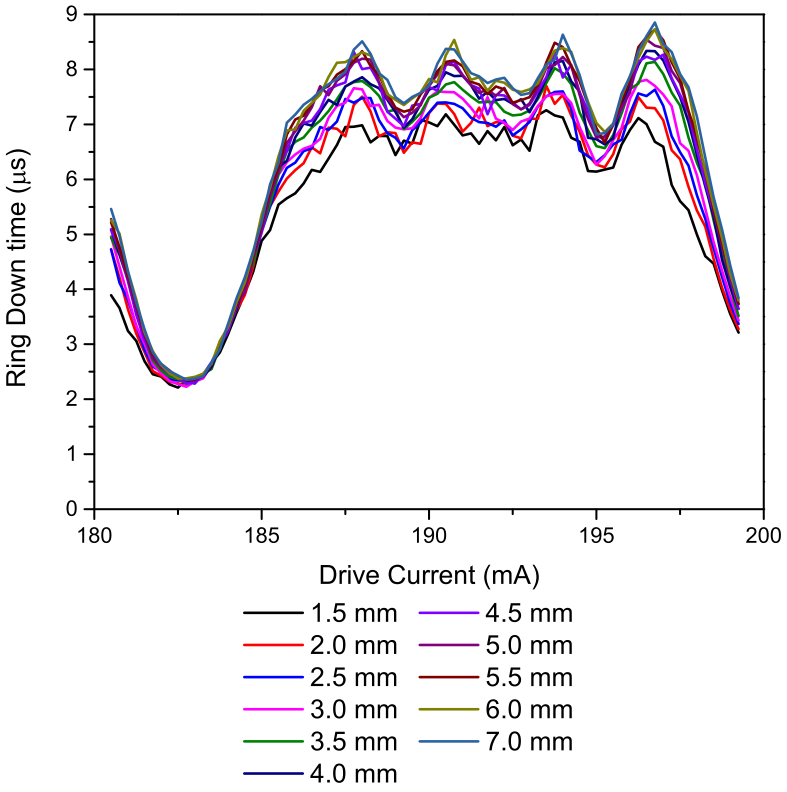

Figure 5.21: Ring-down time spectra recorded using the 1547 nm laser at various heights above the burner in the $\phi = 2.37$ flame.

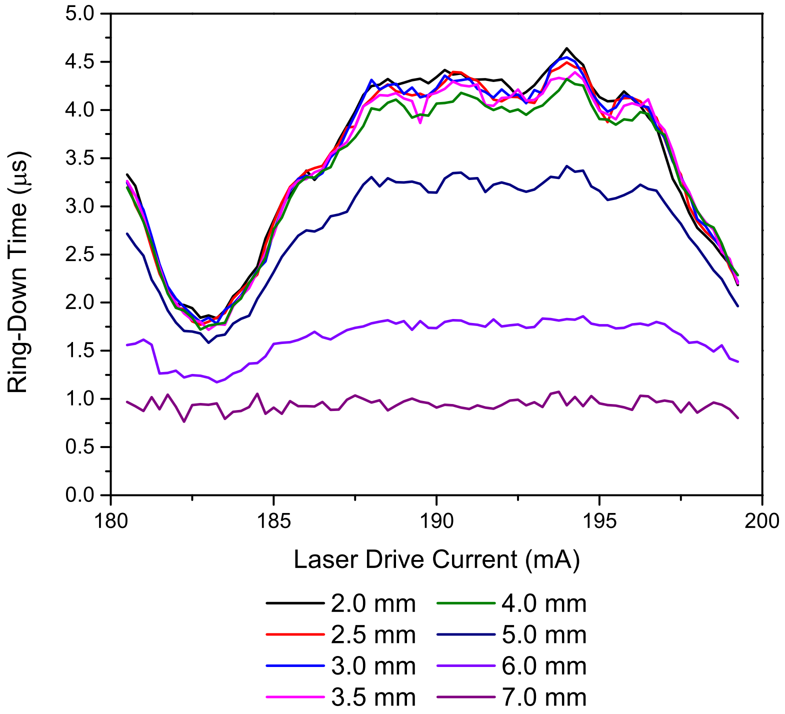

Figure 5.22: Ring-down time spectra recorded using the 1547 *nm* laser at various heights above the burner in the $\phi = 2.59$ flame.

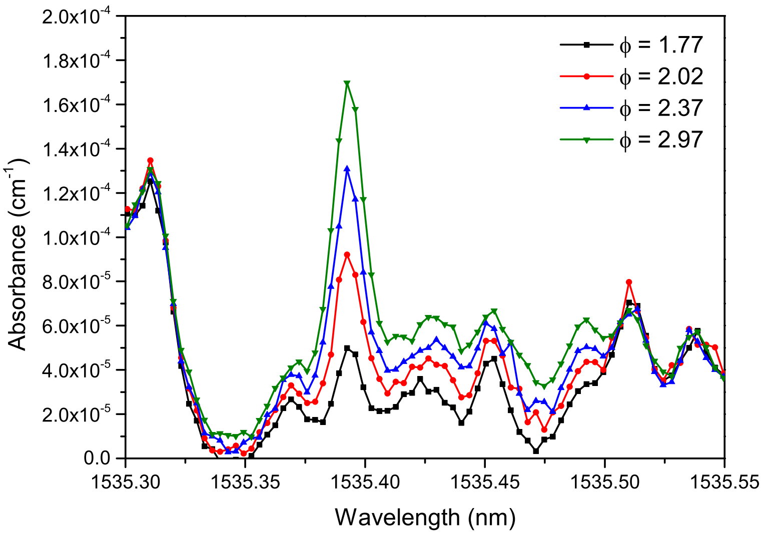

Figure 5.23: Initial comparison of normalised spectra for ϕ = 1.77 to ϕ = 2.59 recorded 3 mm above the burner.

alence ratio flame, where several small features become apparent. This change in the shape of the spectra will reduce the accuracy of the absolute absorption measurements made using the spectrometer, by introducing errors in the normalisation thereby effecting the measured absorption at the peak of the P17e feature. However, the variation is lower than the attenuation due to the presence of particulate. Although this variation is a source of error, other sources, including the lack of agreement with the model spectra, and poor understanding of the temperature dependence of the broadening parameters at high temperatures, have a more significant contribution the residual of the fit and are therefore are a greater source of error in the final concentration values.

5.5.3 Initial Equivalence Ration Comparison.

Due to the variation in the broadband intra-cavity loss, which is observed with varying the equivalence ratio, the initial design for the spectrometer described in chapter 4 would not be capable of producing comparable spectra.

However as shown in figure 5.23 the variation in optical absorption from acetylene

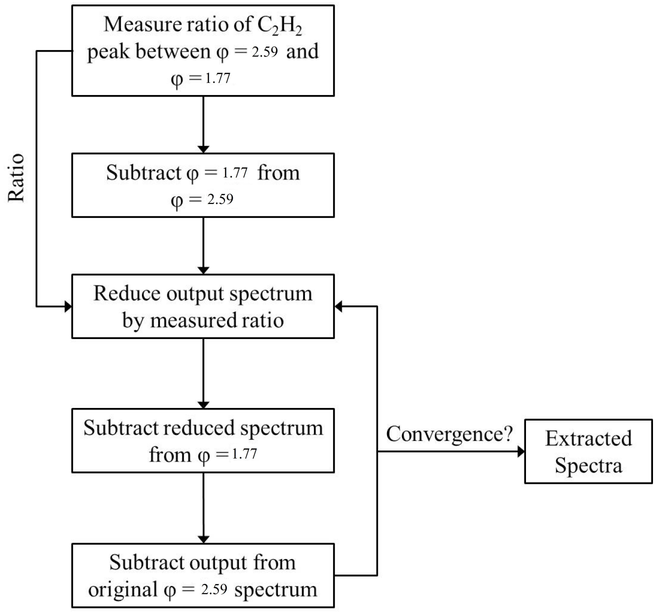

Figure 5.24: Flow-chart of procedure for iterative extraction of acetylene features from constant background spectra.

as a function of the fuel equivalence ratio, is clearly apparent using the new design. This data shows in increase in acetylene concentration, which is expected due to the progressively more sooting conditions as the equivalence ratio is increased. Interestingly, the variation in absorbance as a function of equivalence ratio is limited to the region in which acetylene has a contribution, as shown in figure 5.15. It appears that the spectral features for which absorbance is roughly invariant with equivalence ratio may be associated with species, perhaps water vapour, whose concentration at this location in the flame is generally constant

5.6 Determination of Absolute Acetylene Concentration Profiles

5.6.1 Extraction of Acetylene Spectra

One of the major challenges in determining acetylene concentrations from the spectra acquired using the spectrometer is the large discrepancy to the model spectra. This could potentially introduce large errors in the calculated concentration values using the

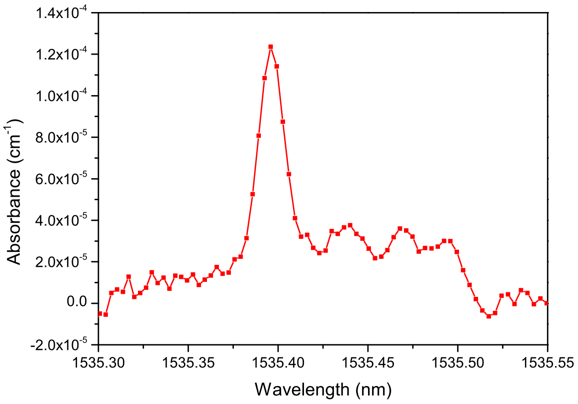

Figure 5.25: Initial estimation of acetylene contribution to spectrum.

model fitting procedure The initial comparison of the different equivalence ratios indicated that there was very little variation of the spectra where there is no contribution from acetylene, this was also observed to hold true at all positions above the burner up to 7 mm. A reasonable approximation of the acetylene concentration can be made using the iterative algorithm shown in figure 5.24.

Figure 5.25 shows the first step in the iterative process where the spectrum recorded in the $\phi = 1.77$ flame has been subtracted from the $\phi = 2.59$ spectrum. This can be considered as a first estimation of the acetylene spectrum. This intial estimation is first reduced by the initial ratio of the acetylene peaks in the $\phi = 1.77$ and $\phi = 2.59$ spectra, and then subtracted from the initial $\phi = 1.77$ spectrum which provided the initial estimation of the non-acetylene portion of the spectra, which is shown on figure 5.26. This first estimation of the non-acetylene spectrum is then subtracted from the original $\phi = 2.59$ spectrum, providing the second estimation of the acetylene spectrum. The process of rescaling the estimated acetyene spectrum, and subtracting from the leaner flame is repeated until convergence. Figure 5.27 shows this second estimation of the acetylene spectrum, along side two further iterations of the extraction algorithm, for a total of four iterations until convergence.

Figure 5.28 shows the output of the algorithm when applied to the spectra for each

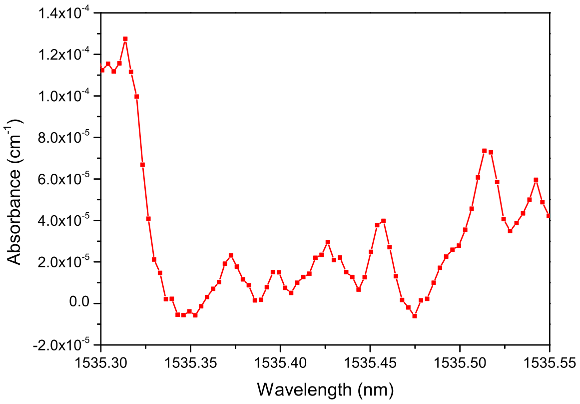

Figure 5.26: Initial estimation of non-acetylene contribution to spectrum.

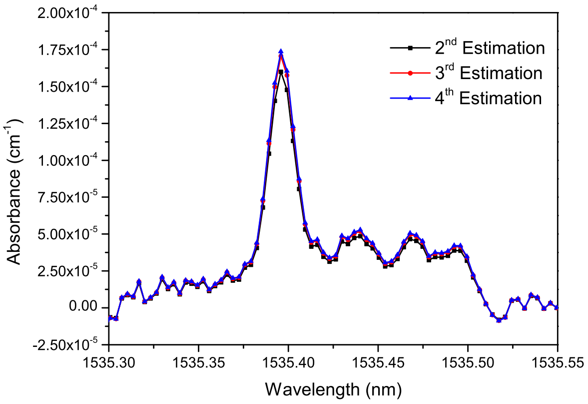

Figure 5.27: Estimation of acetylene contribution following several iterations of extraction algorithm.

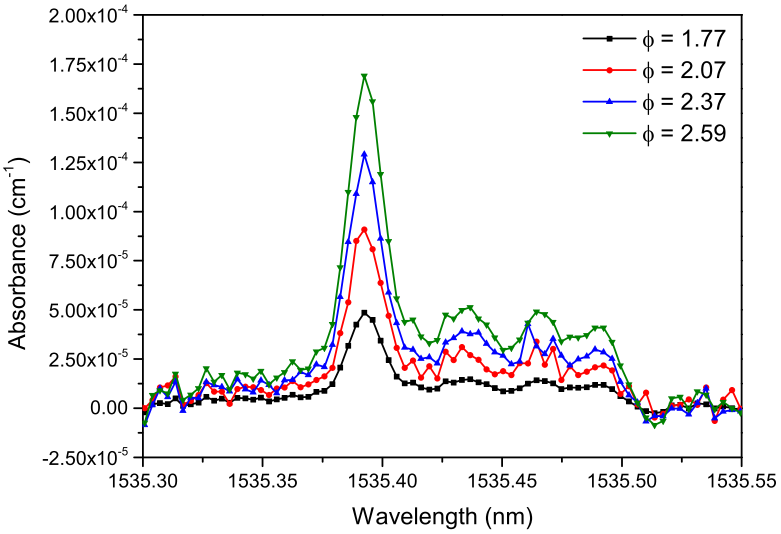

Figure 5.28: Example of extracted spectra for all flame conditions, recorded 2 mm above the burner.

equivalence ratio included in figure figure 5.23. The extraction algorithm removes the majority of the unassigned absorption features, but causes an increase in the level of noise present in the data. Figure 5.29 shows the extracted spectra of the $\phi = 2.37$ flame compared to model spectra calculated from HITRAN 2008. Although some discrepancies remain, the shape of the extracted spectra has a much better resemblance to the model spectra, which should improve the accuracy of the fit. This approach has a further benefit that it removes the need to model the complex water vapour spectrum reducing the number of floating parameters in the fitting process.

Although the shape of the extracted spectra appears to be a better match to the model, the method does not give an exact representation of the acetylene spectra. Figure 5.30 shows an estimation of the non-acetylene portion of the spectrum, which highlights a further error in extraction algorithm. The estimation of the background spectra falls below zero absorbance in several regions which indicates that there will be a corresponding over estimation of absorbance in the extracted acetylene spectra.

Another disadvantage of extracting the acetylene spectra in this way is that the noise

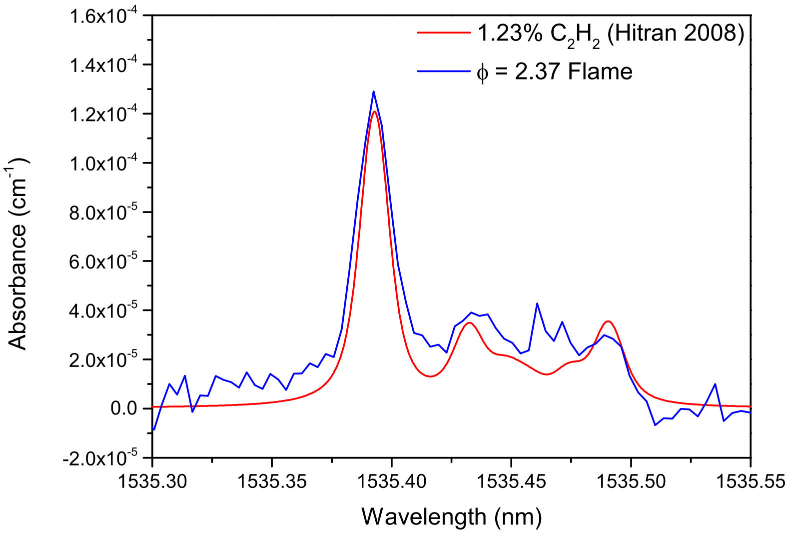

Figure 5.29: Comparison of extracted spectra to Hitran 2008 model.

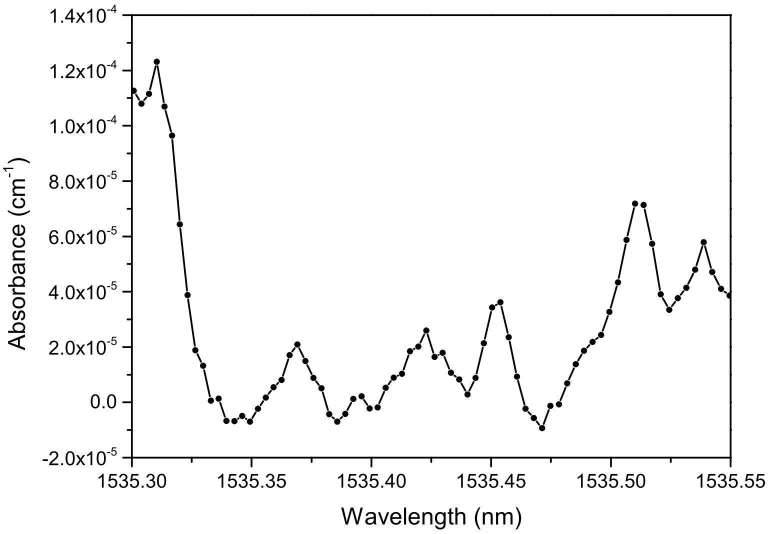

Figure 5.30: Background spectra outputted from iterative extraction.

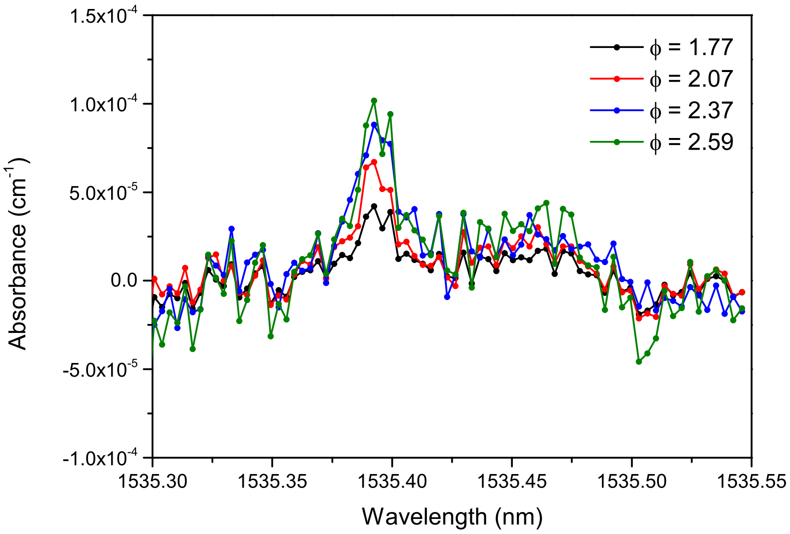

Figure 5.31: Example of extracted spectra for all flame conditions, recorded 7 mm above the burner.

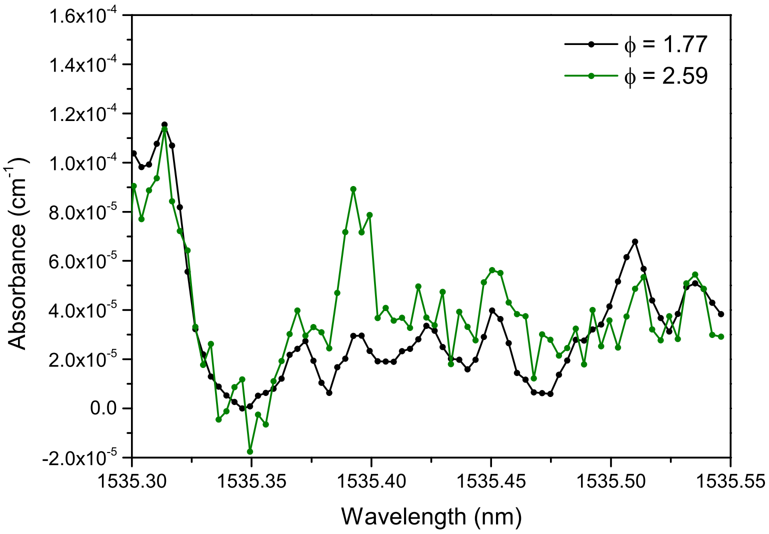

Figure 5.32: Comparison of un-extracted spectra for the ϕ = 1.77 and ϕ = 2.59 flames recorded 7 mm above the burner.

in each spectra will to each of the other spectra following extraction. This is particularly prevalent for measurements which are taken at a position in the flame where there is an increase in the intra-cavity loss in the richer flames. Figure 5.31 shows extracted spectra recovered 7 mm above the surface for the $\phi = 1.77$ and $\phi = 2.59$ flames. There is a marked decrease in the SNR of each of the spectra, which originates from the poor quality of the $\phi = 2.59$ spectra. The extracted $\phi = 1.77$ and $\phi = 2.59$ spectra acquired 2 mm above the burner have an SNR of over 17 compared to the spectra acquired at 7 mm, which have an SNR of approximately 5. The SNR of the extracted spectra begins to decrease above 5 mm above the burner which is consistent which the increase in intra-cavity loss shown on figure 5.20.

5.6.2 Fitting of Model Spectra

The concentration of acetylene can be determined by fitting the model spectra, calculated using parameters from the Hitran 2008 database, to the extracted experimental spectra. This was achieved using an unconstrained non-linear fit in Matlab (function: fminsearch), where the temperature, pressure, and path-length were held constant at the values given in table 5.1. Figure 5.33 shows an example fit to an extracted acetylene spectra acquired 2 mm above the burner in a $\phi = 2.59$ flame.

The output from the fitting function is an acetylene concentration of 1.85% with a total residual (σ/N) of 2.29×10^{-4}. The fit is generally quite poor, particularly at the peak of the main P17e feature, where the peak absorbance is significantly above the experimental data, which potentially provides an over estimation of the acetylene concentration. The quality of the fit can be marginally improved by truncating the experimental data and fitting only over the main feature (shown on figure 5.34). This reduces the calculated concentration to 1.81% and with a lower total residual of 1.71×10^{-4}. However, there is still a relatively large discrepancy at the peak of the main feature.

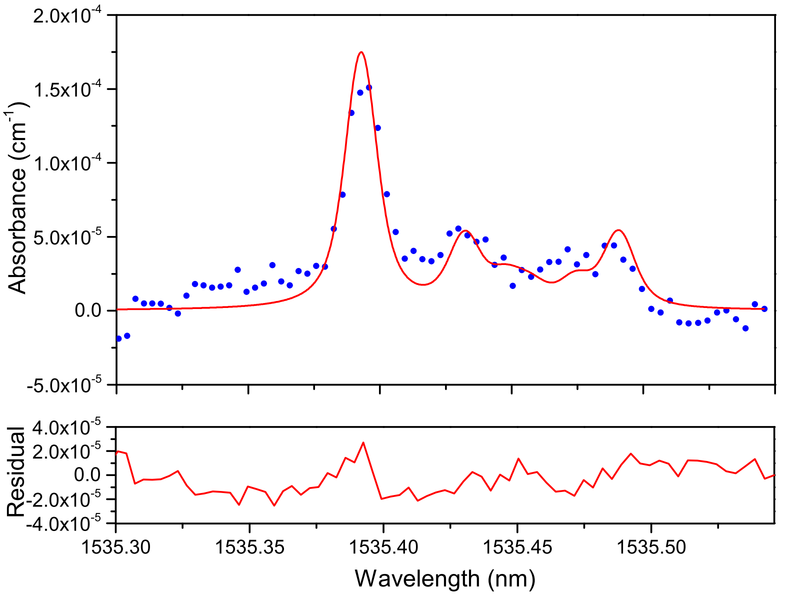

Figure 5.33: Example fit to the extracted spectra for concentration over a number of acetylene features.

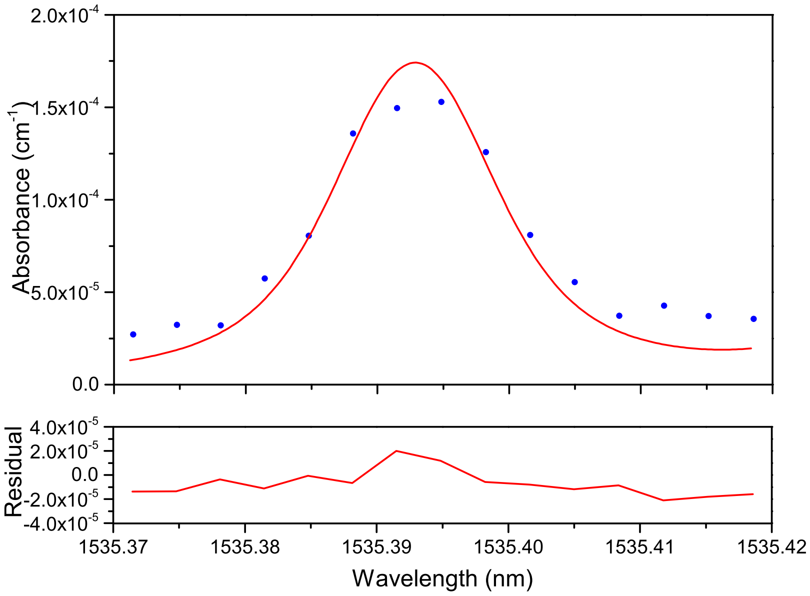

Figure 5.34: Example fit to the extracted spectra for concentration, truncated to the P17e feature only.

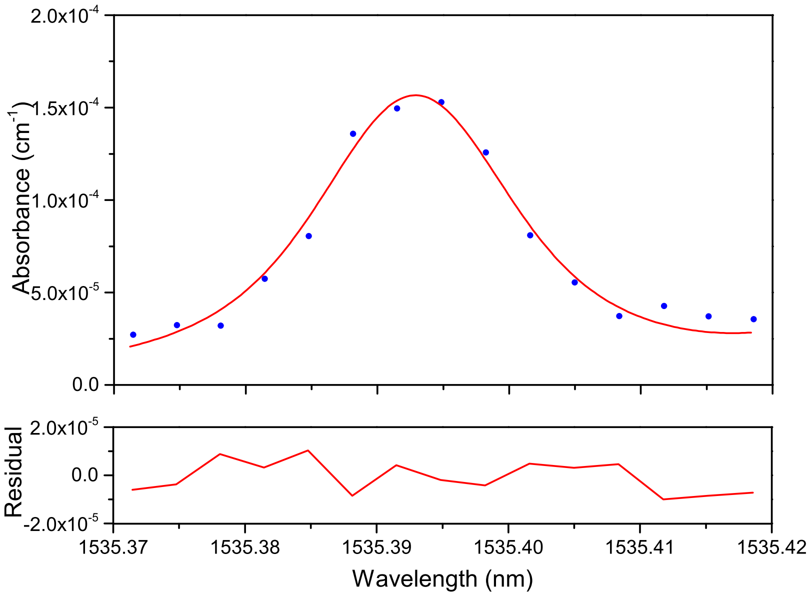

Figure 5.35: Example fit to the extracted spectra for concentration and air broadening parameter.

The error in the fit appears to originate from an incorrect calculation of the FWHM of the model. Returning to the numerical approximation of the Voigt profile presented in chapter 2 it is likely that the source of this error is in the calculation of the Lorentzian FWHM (Γ_L) which is calculated using the broadening parameters taken from the HITRAN 2008 database. At such low concentrations of acetylene the largest contribution to Γ_L will be the air broadened half-width (Γ_{air}). The poor fit indicates that the temperature dependence of Γ_{air} given in HITRAN may be incorrect when applied to the elevated temperatures present in the flame.

The fitting program can be adapted to fit for Γ_L for the main feature in addition to concentration. Figure 5.35 shows a such a fit over the same truncated data. Including the broadening parameter in the fit produces a better match at the peak of the feature and further lowers the total residual to 8.92×10^{-5}. The calculated concentration is now at 1.91%, and the broadening parameter determined from the fit is $0.0306\,\mathrm{cm}^{-1}$ at the flame temperature compared to $0.0207\,\mathrm{cm}^{-1}$ calculated from HITRAN for this temperature. The temperature at which the HITRAN broadening parameter would

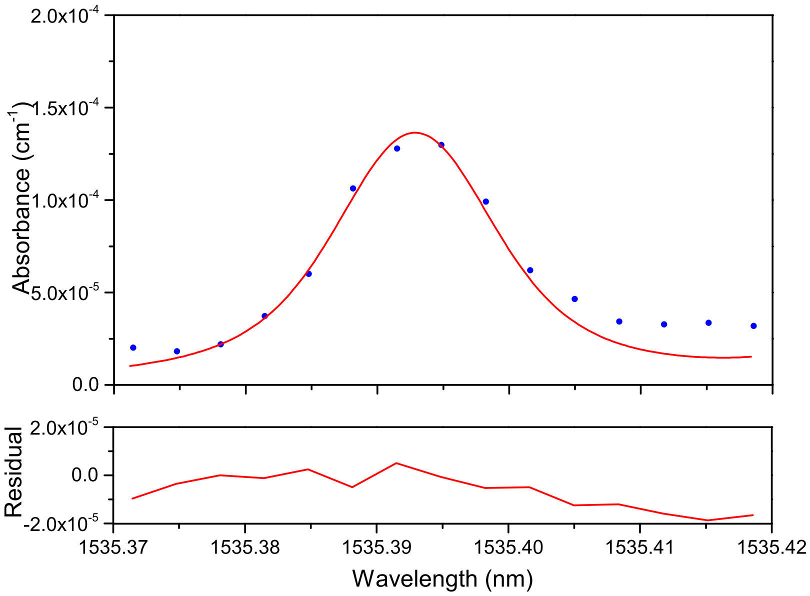

Figure 5.36: Example fit to the un-extracted spectra using the constant background assumption.

match the recorded data is 948.71 K, back calculated using the temperature dependence coefficient from HITRAN (0.75), which is far lower than the input temperature for the model, and below that which was measured by Hu et al [42] at this position in the flame.

The final approach to fitting the model spectra is to make the assumption that the background spectra forms a constant continuum of background absorption under the P17e feature. The un-extracted spectra is then truncated as before, and the offset is subtracted to compensate for this assumption. It is unlikely that this approach would produce accurate absolute values for acetylene concentration. However, the relative concentration values may provide a useful comparison for the values determined from the extracted spectra, as they will not be effected by the reduction in SNR which occurs with the iterative extraction. The accuracy of this assumption will also be at its best when the acetylene concentration is high, as it's contribution to the spectrum will be higher compared to the other species present which are not included in the fitted model.

Figure 5.36 shows a fit using the above assumption. The fit provides a concentration of 1.41% and a total residual of 1.13×10^{-4}. The concentration is lower than that determined for the extracted spectra using the Hitran broadening parameters, which indicates an over assumption in the background spectra.

5.6.3 Acetylene Concentration Profiles

The spectrometer was used to acquire spectra at a range of positions between 1.5 mm and 7 mm above the burner in the $\phi = 1.77, 2.07, 2.37, \& 2.59$ flames. Figures 5.37 and 5.38 show concentration profiles determined from these spectra, using the air broadening parameter from HITRAN 2008, and fitting for broadening parameters respectively.

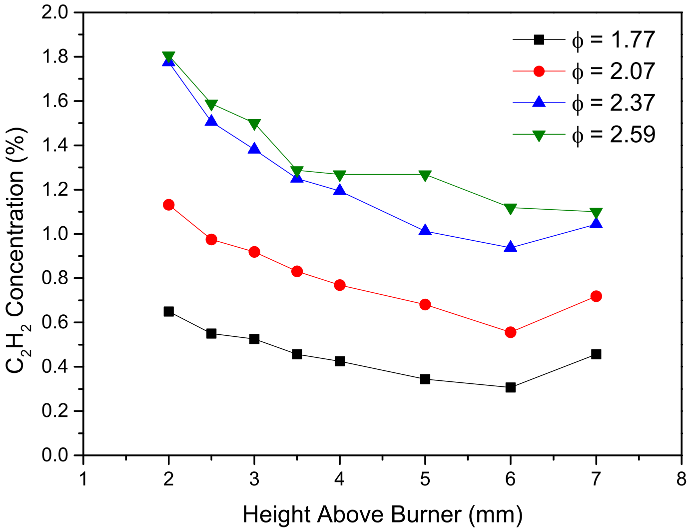

Figure 5.37: Acetylene concentration profiles from fitting the extracted spectra for concentration only.

There is an unexpected upturn in the calculated acetylene concentration between 6 mm and 7 mm with both of these approaches. From previous literature [104] it is likely that this upturn may be the result of a poor fit, due to the decreased SNR in these spectra. Figure 5.39 shows the total residual for each of the fits. There is a marked increase for the spectra acquired at 7 mm above the burner indicating that the increase in concentration at this point may indeed be due to the low quality of

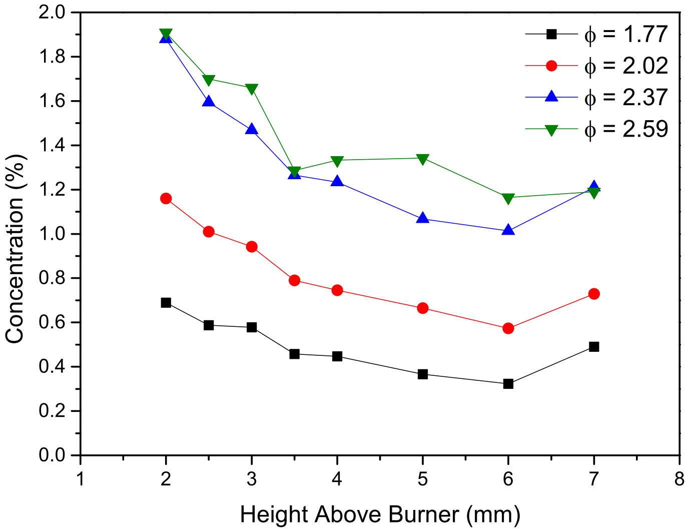

Figure 5.38: Acetylene concentration profiles from fitting the extracted spectra for concentration and air broadening parameter.

the extracted spectra. The residual is reduced for all spectra when the broadening parameter is included in the fit, although there is only a minor change in the determined concentration. Figure 5.40 shows the air broadening parameter determined from each fit. There is no clear trend apparent, although the similarity in the shape of each of the curves gives further indication that the spectra have an influence on each other during the extraction process.

Figure5.41 shows the concentration profiles determined using the constant background assumption. The shape of the concentration profile is largely in agreement with the extracted spectra profiles, with the acetylene concentration decreasing with increased height above the burner. However, the profiles do not show the marked increase at 7 mm. As previously stated, this method is expected to provide the most accurate view to the change in acetylene concentration through the flame. The lack of the marked increase in this data adds further weight that this was indeed due to the reduction in the quality of the fit at this point. Another, minor, advantage to this method is that it does not require measurements at each equivalence ratio at each posi-

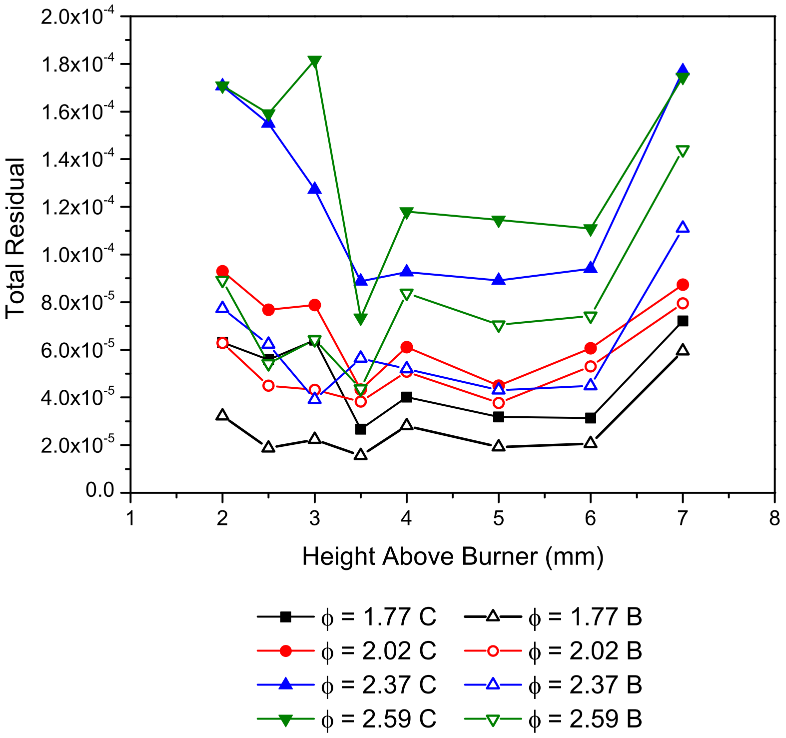

Figure 5.39: Comparison of total residuals for each fitting method and flame condition. 'C' denotes fit for concentration only, and 'B' denotes fit for both concentration and air broadening parameter.

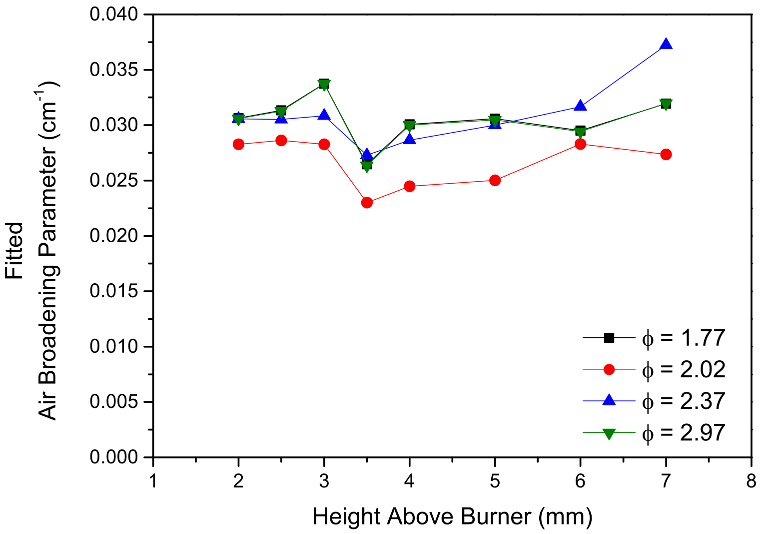

Figure 5.40: Air broadening parameters determined from fitting extracted specta.

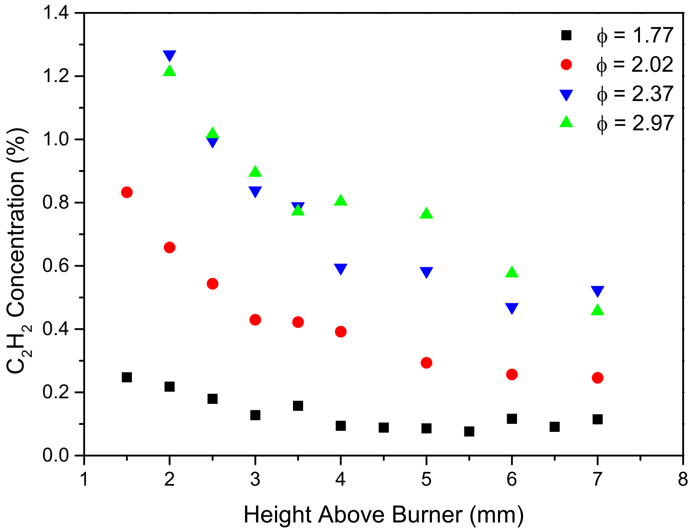

Figure 5.41: Acetylene concentration profiles from fitting the un-extracted spectra.

tion, which allows the concentration to be estimated in positions where it is not possible to make measurements in the higher equivalence ratio flames (e.g. 1.5 mm above the burner).

In all cases there is little difference in the concentration profile between the ϕ = 2.37 and ϕ = 2.59 flames, which is also the case observed for the profile of the broadband attenuation in these flames.

The difference in out-put from each the fitting techniques allows for the estimation of the uncertainty in the acetylene concentration measurement, which is estimated to be 12% of the measured value. The discrepancy resulting from the use of the HITRAN 2008 broadening parameters highlights the need for further calibrated spectroscopic work on acetylene and water at elevated temperatures. The results of such measurements would further aid the identification of the unidentified features present in the flame spectra and would provide a better estimate of the spectroscopic parameters used in the fit, included but not limited to the broadening parameter.

6 Conclusions and Further Work

6.1 Overall conclusions

6.1.1 Project Aims and Objectives

The aim of this project was to develop a measurement technique to measure the concentration profile of acetylene (C_2H_2), which is a precursor in soot formation, in laminar ethylene (C_2H_4) flames supported on the porous-plug burner (described in detail in chapter 3). The low absorbance exhibited by acetylene in the near infra-red precluded the use of direct absorption techniques, and therefore continuous-wave cavity ring down spectroscopy (cw-CRDS) was identified as a technique that should have sufficient sensitivity.

The individual objectives outlined in the introduction (chapter 1) were as follows:

1. To evaluate the porous-plug burner to identify conditions which may inhibit the in-situ operation of the cw-CRDS spectrometer.
2. To develop a cw-CRDS spectrometer which possesses sufficient robustness to operate in-situ within the porous-plug burner.
3. The novel application of cw-CRDS to recover absorption spectra of a suitable acetylene feature in-situ in the porous-plug burner, from which concentration can be determined.
4. To apply existing modelling techniques to the recorded spectra to recover the vertical concentration profile of acetylene in a range of flames supported on the porous-plug burner

6.1.2 Evaluation of Porous-Plug Burner.

Due to the inherent sensitivity of cavity enhanced techniques to optical disturbances caused by the thermal gradients, and soot particulate within the flame, it was deemed necessary to undertake a series of characterisation measurements on the porous-plug burner flames to identify any locations/flame conditions which may limit the usefulness of the cw-CRDS technique.

During this evaluation a novel, easy to implement, photoacoustic technique using an intensity modulated high-power diode laser was developed for in situ measurement of soot profiles. The photoacoustic measurements compared well to those made using the well-established laser induces incandescence (LII) technique, producing repeatable measurements across a range of flame conditions. Soot distribution profiles for three different flames were recovered using this technique, which was able to detect the presence of soot from ≈ 6 – 7 mm above the surface of the burner in each case. The gradient of the distribution profile, and therefore the maximum soot volume fraction, was shown to increase with equivalence ratio (ϕ), and the limit of detection for the technique was determined to be 5 ppb of soot, based on the variation of the background acoustic signal in absence of the flame. This detection limit was ≈ 5% of the maximum soot volume fraction of 5.526×10^{-7} for the $\phi = 2.97$ flame. The soot volume fractions that were measured for this burner were higher than previously reported in other burners, which use a larger diameter porous-plug, operating at the same equivalence ratios. Comparison measurements of temperature were undertaken on the burner used for this project and one such larger burner, using a thermocouple probe positioned 7 mm above the burner surface. The temperature was 100K lower in the smaller burner, and it is believed that this is due to differing heat transfer rates to the stabilisation plate in each case. The presence of particulate soot will limit the usefulness of the cw-CRDS technique at positions above 6 – 7 mm form the burner surface, as it will greatly increase the background intra-cavity losses.

The second characterisation technique used for this technique used for this evaluation was based on measurements of the viable emission from the flame. These measurements were made by imaging a range of equivalence ratio flames (ϕ = 1.77 to ϕ = 2.97) using a commercially available digital camera. By separating each of the camera images into its constituent red, green, and blue components inferences could be made about the position of the reaction zone of the flame, due to an increase in the intensity of the red and green signal close to the surface of the burner. The images showed that the reaction zone, or flame-front, shifted upwards away from the burner surface as the equivalence ratio was increased due to a reduction of the temperature in the region. The reaction zone is the region of the flame which will have the steepest thermal gradients and therefore the highest optical disturbance which will also limit the usefulness of cw-CRDS in this region.

The red component of the images indicated that orange Planck emission begins to occur at a height of 4 – 5 mm above the burner, which is lower than where soot can be detected using either the LII or photoacoustic technique. This emission is thought to originate from nascent particles which do not exhibit sufficient absorption in the near infra-red for detection using either technique.

6.1.3 Development of cw-CRDS Spectrometer

In chapter 4 the background theory of optical cavities was presented and attention was drawn to specific considerations for the design of a cw-CRDS spectrometer. Accurate mode-matching to the fundamental TEM_{00} transverse mode, and therefore suppression of high order modes was identified as a key step in maximising the sensitivity of the spectrometer for combustion measurements. A spectrometer was designed using a $LiNbO_3$ intensity modulator to attenuate the input light to the cavity and initiate a ring-down measurement. This design of the spectrometer was shown to have an absolute detection limit of $3.670 \times 10^{-8}\,\mathrm{cm}^{-1}$ (3σ), which was calculated by measuring a transition of ambient, room temperature, water vapour in absence of a intra-cavity flame. This detection limit, although ex-situ with regards to the flame, is several orders of magnitude greater than should be required for the in-situ detection of acetylene.

6.1.4 cw-CRDS Performance in Laminar Flames

In chapter 4 the application of the initial design of the cw-CRDS spectrometer to a $\phi = 2.22$ flame was presented. The initial in-situ measurements demonstrated that the introduction of the flame produced a significant increase in the intra-cavity losses. This was observed as a $\approx 20\,\mu$s reduction in the ring-down time of the cavity, suggesting the fractional intra-cavity loss had increased by 1.61×10^{-4}. Despite the increased losses the P17e absorption feature, which has previously been uses for acetylene detection in different flames was easily identified.

Although this application was to the best of the authors knowledge the first application of cw-CRDS in-situ in a flame several areas in which the design of the spectrometer could be improved were identified. The key shortcoming of the initial spectrometer design was the inability to normalise the recovered spectra by assigning which proportion of the optical loss was due to absorption, and which was due to broadband optical losses caused by disturbance to the resonant cavity mode by the flame. The spectrometer design was refined to include a second DFB laser which was tuned to a wavelength which appeared to be free from any absorption features, that were of the same order as the acetylene feature of interest. By alternately switching back to this laser the broadband optical loss could therefore be determined for each point in the spectrum, allowing for a point-by-point normalisation. Ring-down measurements were conducted at this wavelength at a range of positions above the surface of the burner for a range of different equivalence ratio flames. In agreement with what was observed based on the emission measurements undertaken in chapter 3 the ring-down time in all flames above $\phi = 1..77$ was shown to decrease from about $4-6\,$mm above the burner. This adds weight to the explanation that nascent soot particles begin to form in this region which exhibit such a low near infra-red absorption that their detection requires the high sensitivity that can be achieved using the cw-CRDS approach.

The refined design of the spectrometer also replaced the $LiNbO_3$ intensity modulator with a semiconductor optical amplifier, which increased the intensity of the light resonating within the cavity. This not only increased the signal to noise ratio of the ring-down trace, but the increase in the intensity of the light leaving the cavity increased the number of times that the trigger level was achieved and therefore doubled the measurement rate of the spectrometer.

The in-situ detection limit of the refined design was determined to be $1.2 \times 10^{-5}\text{cm}^{-1}$ (3σ) demonstrating a significant improvement over what is generally considered achievable using single pass measurement techniques under such conditions. A key benefit of using cw-CRDS over single path techniques is that it is immune to any noise caused by emission from the flame and that it provides a direct measurement of absorption without the complex calibration required by some other cavity based techniques.

6.1.5 Recovery of Acetylene Concentration Profiles

Although the sensitivity of the cw-CRDS spectrometer was sufficient to resolve the absorption spectra, through a range of flame conditions and measurement positions, the recovered spectra was highly complex showing a number of features which interfered with the p17e acetylene feature. When the spectra is compared to model spectra of acetylene from the HITRAN 2008 database and water from the HITEMP 2010 database, it is possible to assign some of the stronger interfering features as water but the majority of the weaker absorption features are a poor match to the model. In chapter 5 a number of post-processing approaches were applied to isolate the absorption due to acetylene from these unidentified features. The variation in the recorded spectra as the equivalence ratio of the flame was varied was limited to wavelengths at which, according to HITRAN, acetylene should have a contribution. The contribution from the unidentified and water features remained constant over this region. Therefore, an iterative approach was tested to subtract the features for which the absorption did not change with equivalence ratio. The result of this extraction was a closer match to the HITRAN 2008 model spectra for acetylene, although full width half maximum of the p17e feature was broader than that of the model spectra. This was understood caused by a poor understanding of the temperature dependence of the air broadening parameter at the flame temperature. To improve the quality of the fit, the air broadening parameter was included as a floating parameter in the model, the fitted value of which showed only minor variation across all the fitted spectra, whilst producing similar values for acetylene concentration. The final strategy applied to fitting the model spectra was to tightly limit the fit to a small wavelengths over the p17e feature with no extraction, making that the other contributions form a constant offset over this region. This approach produced acetylene concentrations which were lower than those determined from the extractive method however, the spectra were not effected from the poor SNR associated with the iterative extraction process. The lower concentration values were likely due to a reduction of the absorbance at the peak of the P17e feature, and therefore this approach may only provide an indication as to the difference in concentration at each position in the flame.

For all approaches to fitting the acetylene concentration was shown to increase with the flame equivalence ratio. This is in agreement with the evaluation of the soot volume fraction presented in chapter 3, which showed an increase in soot volume fraction with equivalence ratio. The shape of the concentration profiles appears to show that acetylene gradually drops as the measurement position is moved upward, indicating its consumption as the size of the poly-aromatic hydrocarbons increases, moving towards the creation of particulate. In all cases the change in acetylene concentration between the $\phi = 2.37$ and $\phi = 2.97$ flames is significantly lower than that to the lower equivalence ratio flames.

6.1.6 Summary of Conclusions

With reference to the aims of this project which were outlined in the introduction, and restated in section 6.1.1, the outcomes of this work are summarised in the following points:

1. A novel, and relatively simple, photoacoustic technique for in-situ measurement for the measurement of soot distribution profiles in a porous-plug flat-flame burner was presented.
2. A detailed evaluation of the porous-plug burner was undertaken which identified several regions of the flame which may limit the usefulness of the cw-CRDS technique.
3. The first applications of cw-CRDS to conduct in-situ flame measurements were demonstrated, which had a sufficiently high sensitivity to resolve the p17e absorption feature of acetylene.
4. A limitation of both the LII and photoacoustic measurement techniques was identified with respect to the measurement of nascent particles, however the potential to detect these particles with cw-CRDS was demonstrated.
5. Several strategies were tested to evaluate the acetylene concentration from the spectra recovered from the porous-plug burner flames, and concentration profiles were reported and compared for each strategy.

6.2 Further Work

6.2.1 High Temperature Spectroscopy

In chapter 5 recovered spectra at wavelengths around 1535 nm, from C_2H_4 flames supported on the porous-porous plug burner were presented. Despite the recorded spectra possessing a high SNR, it did not compare well with model spectra calculated using the

HITRAN 2008 and HITEMP 2010 databases, enabling only the stronger absorption features to be assigned and preventing the full model being accurately fitted to the recovered spectra. Several reasons were postulated for this lack of agreement, including the presence of other species which were not included in the model, and a poor understanding of the high temperature behaviour of the species that were included.

A method of improving the model would require high temperature absorption measurements to be undertaken on C_2H_2 and H_2O under tightly controlled and monitored conditions. Firstly, the spectra recorded in these experiments would highlight absorption features in the flame spectra which do not arise from the presence of C_2H_2 and H_2O. Secondly, the controlled high temperature spectra of C_2H_2 and H_2O can be fitted using the Voight function to gain a more accurate understanding of their temperature dependent parameters (such as: line strength, and broadening parameters), which would increase confidence in the recovered C_2H_2 concentration profiles.

6.2.2 Application of cw-CRDS to Low Pressure Flames

One of the limiting factors that was identified with the in-situ cw-CRDS absorption measurements was the high number of interfering features, which hindered the determination of species concentration. By reducing the ambient pressure surrounding the flame, the air broadening parameter, which was identified as being poorly understood at combustion temperatures, has much lower contribution to the absorption line-shape which serves to narrow and better isolate each absorption feature. In-conjunction with the high temperature spectroscopy outlined in section 6.2.1 this may better enable the concentration to be accurately determined. A further advantage of operating at low pressure is that the gradients of the flame become more spatially extended, which reduces the requirement such highly spatially resolved measurements.

6.2.3 Other Cavity Enhanced Techniques

In chapter 2 an overview of other techniques utilise a resonant optical cavity to increase the effective path-length for absorption measurements was presented. Unlike CRDS these other techniques use the reduction in the on-resonance transmission through the cavity to recover the absorption spectrum, rather than the lifetime of light within the cavity. Over the course of this work two such techniques have been identified as showing promise for making in-situ flame measurements: Integrated Cavity Output Spectroscopy (ICOS), and Cavity Enhanced Absorption Spectroscopy using Optical Feedback (OF-CEAS).

The simpler of the two techniques, ICOS, the cavity mode structure of the cavity is treated as a continuum when integrated over several scans of either the laser frequency, or the cavity length. It is therefore preferential that the laser is in resonance with each of the TEM_{mn} mode for an equal time, and for this reason mode-matching optics are not normally used in ICOS experiments. To further ensure the resonance time is equal across all cavity modes a rapid scan frequency is required, such that it becomes the limiting factor for the resonance time rather than the coherence length of the laser source or the mechanical stability of the cavity. In chapter 5 degradation of the mode-matching to the TEM_{00} mode, due to thermo-optical distortions caused by the flame, was identified as one of reasons for the reduction in the ring-down time of the cavity when taking measurements in-situ. As ICOS treats the mode spectrum as a quasi-continuum the effect of this degradation on the resulting spectra should be reduced, therefore ICOS may have a higher sensitivity for in-situ measurements. The disadvantage of ICOS is that there will be a reduction in the spatial resolution of the technique associated with the excitation of the higher transverse modes.

The second cavity enhanced technique, OF-CEAS, is a more complicated technique where the backwards propagating light leaking out from the input cavity mirror is fed back into the laser source. If the correct phase is maintained this feedback not only locks the laser to the cavity mode but also seeds the active medium of the laser, narrowing the line-width to only those frequencies that are resonant in the cavity, and thereby increasing the cavity transmission. Assuming that an adequate feedback intensity can be achieved with a flame intra-cavity to maintain the lock to the cavity mode, this increase in the on-resonance cavity transmission has the potential to compensate for the loss in coupling efficiency caused by the presence of the flame. The lock to the resonant cavity mode may also reduce the effect of any minor mechanical disturbances to the cavity. The main disadvantage to this technique is that it is limited to laser sources which respond favourably to optical feedback, typically c-QCLs, as feedback to some sources can result in frequency jitter of the output.

6.2.4 Photoacoustic Soot Detection With Fibre Lasers

Although the novel photoacoustic technique for soot measurement, presented in chapter 3, performed comparably with the more common laser induced incandescence (LII) technique the true potential of the technique could not be explored due to limitations of the laser source used. For a number of years doped fibre amplifiers have been used in the telecommunications industry to increase the output power of diode laser diodes, whilst preserving the high speed intensity modulation characteristics of the laser diode. An amplifier such as such as a Ytterbium Doped Fibre Amplifier (YDFA), which is readily commercially available, could be used to increase the output power of a 1064 nm DFB laser from ≈ 10 mW up to several Watts. If the intensity of the seed DFB laser is modulated then there will be an amplified modulation depth in the EDFA output.

Initial testing using a commercially available (Keopsys) YDFA has shown that modulation depths of up to 2 W are achievable using this approach, with an average output power of ≈ 1 W. This modulation depth is an order of magnitude greater then the high power diode originally used. A further advantage of the fibre amplifier approach is that it can achieve a faster modulation frequency (up to ≈ 1 MHz), which would further isolate the signal from ambient acoustic noise which typically occurs at low frequencies.

6.2.5 cw-Laser Induced Incandescence

In a recent publication [105] the potential to use cw-diode laser sources for LII was demonstrated. The lasers used in this example had a relatively low output power (175 mW) compared to the high power pulsed lasers which are typically used for such measurements. The fibre amplified diode laser, described in section 6.2.4 shows potential as a source for cw-LII. By The measurement of small and nascent soot particles has proven difficult using the pulsed approach to LII [106] as such particles are often sublimated due to the relatively high laser fluence. The fine control of the output power of the fibre amplified diode laser should allow for operation below the sublimation threshold, and therefore mitigate this difficulty.

References

[1] R. L. Vander Wal, K. A. Jensen, and M. Y. Choi, "Simultaneous laser-induced emission of soot and polycyclic aromatic hydrocarbons within a gas-jet diffusion flame," *Combustion and Flame*, vol. 109, no. 3, pp. 399–414, 1997.

[2] C. Schulz, A. Dreizler, V. Ebert, and J. Wolfrum, "Combustion Diagnostics," in *Springer Handbook of Experimental Fluid Mechanics*, pp. 1241–1315, Berlin, Heidelberg: Springer Berlin Heidelberg, 2007.

[3] T. C. Bond, S. J. Doherty, D. W. Fahey, P. M. Forster, T. Berntsen, B. J. DeAngelo, M. G. Flanner, S. Ghan, B. Kärcher, D. Koch, S. Kinne, Y. Kondo, P. K. Quinn, M. C. Sarofim, M. G. Schultz, M. Schulz, C. Venkataraman, H. Zhang, S. Zhang, N. Bellouin, S. K. Guttikunda, P. K. Hopke, M. Z. Jacobson, J. W. Kaiser, Z. Klimont, U. Lohmann, J. P. Schwarz, D. Shindell, T. Storelvmo, S. G. Warren, and C. S. Zender, "Bounding the role of black carbon in the climate system: A scientific assessment," *Journal of Geophysical Research: Atmospheres*, vol. 118, pp. 5380–5552, jun 2013.

[4] J. Hansen and L. Nazarenko, "Soot climate forcing via snow and ice albedos.," *Proceedings of the National Academy of Sciences of the United States of America*, vol. 101, pp. 423–8, jan 2004.

[5] X. Jiang, L. Zhang, F. Wang, Y. Liu, Q. Guo, and C. Wang, "Investigation of Carbon Black Production from Coal Tar via Chemical Looping Pyrolysis," *Energy & Fuels*, vol. 30, pp. 3535–3540, apr 2016.

[6] B. Magnussen and B. Hjertager, "On mathematical modeling of turbulent combustion with special emphasis on soot formation and combustion," *Symposium (International) on Combustion*, vol. 16, no. 1, pp. 719–729, 1977.

[7] G. Blanquart, P. Pepiot-Desjardins, and H. Pitsch, "Chemical mechanism for high temperature combustion of engine relevant fuels with emphasis on soot precursors," *Combustion and Flame*, vol. 156, pp. 588–607, mar 2009.

[8] H. Wang, "Formation of nascent soot and other condensed-phase materials in flames," *Proceedings of the Combustion Institute*, vol. 33, no. 1, pp. 41–67, 2011.

[9] Hartung, Hult, and Kaminski, "A flat flame burner for the calibration of laser thermometry techniques," *Measurement Science & Technology*, vol. 17, pp. 2485–2493, sep 2006.

[10] R. Farrow, R. Lucht, W. Flower, and R. Palmer, "Coherent anti-stokes raman spectroscopic measurements of temperature and acetylene spectra in a sooting diffusion flame: Colloquium on combustion diagnostics," *Symposium (International) on Combustion*, vol. 20, no. 1, pp. 1307–1312, 1985.

[11] S. Gersen, A. Mokhov, and H. Levinsky, "Extractive probe/TDLAS measurements of acetylene in atmospheric-pressure fuel-rich premixed methane/air

flames." 2005.

[12] Z. W. Sun, Z. S. Li, B. Li, Z. T. Alwahabi, and M. Aldén, "Quantitative C2H2 measurements in sooty flames usingmid-infrared polarization spectroscopy," *Applied Physics B*, vol. 101, pp. 423–432, oct 2010.

[13] S. Wagner, M. Klein, T. Kathrotia, U. Riedel, T. Kissel, a. Dreizler, and V. Ebert, "In situ TDLAS measurement of absolute acetylene concentration profiles in a non-premixed laminar counter-flow flame," *Applied Physics B*, vol. 107, pp. 585–589, mar 2012.

[14] M. Frenklach, "Reaction mechanism of soot formation in flames," *Physical Chemistry Chemical Physics*, vol. 4, pp. 2028–2037, may 2002.

[15] M. Frenklach, D. W. Clary, W. C. Gardiner, and S. E. Stein, "Detailed kinetic modeling of soot formation in shock-tube pyrolysis of acetylene," *Symposium (International) on Combustion*, vol. 20, pp. 887–901, jan 1985.

[16] A. D'Alessio, P. Minutolo, G. Gambi, and A. D'Anna, "Optical Characterization of Soot," *Berichte der Bunsengesellschaft für physikalische Chemie*, vol. 97, pp. 1574–1581, dec 1993.

[17] R. A. Dobbins and H. Subramaniasivam, "Soot Precursor Particles in Flames," pp. 290–301, Springer Berlin Heidelberg, 1994.

[18] M. M. CONSTANTINE and A. D. RICHARD, "Comparison of Soot Growth and Oxidation in Smoking and NonSmoking Ethylene Diffusion Flames," *Combustion Science and Technology*, vol. 66, pp. 1–16, jul 1989.

[19] C. M. MEGARIDIS and R. A. DOBBINS, "Morphological Description of Flame-Generated Materials," *Combustion Science and Technology*, vol. 71, pp. 95–109, may 1990.

[20] B. Hu and U. Koylu, "Size and Morphology of Soot Particulates Sampled from a Turbulent Nonpremixed Acetylene Flame," *Aerosol Science and Technology*, vol. 38, pp. 1009–1018, oct 2004.

[21] R. Dobbins, R. Fletcher, and H.-C. Chang, "The evolution of soot precursor particles in a diffusion flame," *Combustion and Flame*, vol. 115, no. 3, pp. 285–298, 1998.

[22] W. Merchan-Merchan, S. G. Sanmiguel, and S. McCollam, "Analysis of soot particles derived from biodiesels and diesel fuel air-flames," *Fuel*, vol. 102, pp. 525–535, 2012.

[23] K. Kohse-Hoinghaus and J. B. Jeffries, *Applied combustion diagnostics*. Taylor & Francis, 2002.

[24] S. Wagner, B. T. Fisher, J. W. Fleming, and V. Ebert, "TDLAS-based in situ measurement of absolute acetylene concentrations in laminar 2D diffusion flames," *Proceedings of the Combustion Institute*, vol. 32, pp. 839–846, jan 2009.

[25] C. Lou, C. Chen, Y. Sun, and H. Zhou, "Review of soot measurement in

hydrocarbon-air flames," *Science China Technological Sciences*, vol. 53, pp. 2129–2141, aug 2010.

[26] I. S. Burns, X. Mercier, M. Wartel, R. S. Chrystie, J. Hult, and C. F. Kaminski, "A method for performing high accuracy temperature measurements in low-pressure sooting flames using two-line atomic fluorescence," *Proceedings of the Combustion Institute*, vol. 33, no. 1, pp. 799–806, 2011.

[27] H. Michelsen, "Probing soot formation, chemical and physical evolution, and oxidation: A review of in situ diagnostic techniques and needs," *Proceedings of the Combustion Institute*, oct 2016.

[28] P. Desgroux, X. Mercier, and K. A. Thomson, "Study of the formation of soot and its precursors in flames using optical diagnostics," *Proceedings of the Combustion Institute*, vol. 34, no. 1, pp. 1713–1738, 2013.

[29] A. Hartlieb, B. Atakan, and K. Kohse-Höinghaus, "Effects of a sampling quartz nozzle on the flame structure of a fuel-rich low-pressure propene flame," *Combustion and Flame*, vol. 121, no. 4, pp. 610–624, 2000.

[30] E. Nordström, N.-E. Olofsson, J. Simonsson, J. Johnsson, H. Bladh, and P.-E. Bengtsson, "Local gas heating in sooting flames by heat transfer from laser-heated particles investigated using rotational CARS and LII," *Proceedings of the Combustion Institute*, vol. 35, no. 3, pp. 3707–3713, 2015.

[31] J. R. P. Bain, "Near Infrared Tunable Diode Laser Spectroscopy for Aero Engine Related Applications," 2012.

[32] W. Patrick Arnott, H. Moosmüller, C. Fred Rogers, T. Jin, and R. Bruch, "Photoacoustic spectrometer for measuring light absorption by aerosol: instrument description," *Atmospheric Environment*, vol. 33, pp. 2845–2852, aug 1999.

[33] I. Linnerud, P. Kaspersen, and T. Jaeger, "Applied Physics B Gas monitoring in the process industry using diode laser spectroscopy," *Appl. Phys. B*, vol. 67, pp. 297–305, 1998.

[34] T. P. J. Blaikie, J. A. Edge, G. Hancock, D. Lunn, C. Megson, R. Peverall, G. Richmond, G. A. D. Ritchie, and D. Taylor, "Comparison of breath gases, including acetone, with blood glucose and blood ketones in children and adolescents with type 1 diabetes," *Journal of Breath Research*, vol. 8, p. 046010, nov 2014.

[35] A. B. S. Alquaity, E.-t. Es-sebbar, and A. Farooq, "Sensitive and ultra-fast species detection using pulsed cavity ringdown spectroscopy," *Optics Express*, vol. 23, p. 7217, mar 2015.

[36] C. N. Banwell and M. McCash, E, *Fundamentals of Molecular Spectroscopy.* McGraw-Hill, 4th ed., 1994.

[37] N. Göran Blume and S. Wagner, "Broadband supercontinuum laser absorption spectrometer for multiparameter gas phase combustion diagnostics," *Optics Letters*, vol. 40, p. 3141, jul 2015.

[38] X. Mercier and P. Desgroux, “Cavity Ring-Down Spectroscopy for Combustion Studies,” in *Cavity Ring-Down Spectroscopy*, pp. 273–311, John Wiley & Sons, Ltd, 2009.

[39] D. Romanini, A. Kachanov, N. Sadeghi, and F. Stoeckel, “CW cavity ring down spectroscopy,” *Chemical Physics Letters*, vol. 264, pp. 316–322, jan 1997.

[40] J. L. Kinsey, “Laser-Induced Fluorescence,” *Annual Review of Physical Chemistry*, vol. 28, pp. 349–372, oct 1977.

[41] I. Burns, J. Hult, G. Hartung, and C. Kaminski, “A thermometry technique based on atomic lineshapes using diode laser LIF in flames,” *Proceedings of the Combustion Institute*, vol. 31, no. 1, pp. 775–782, 2007.

[42] Y. Hu, *Radical Concentration and Temperature Measurements in Sooting Flames by Cavity Ring-Down Spectroscopy and Laser-Induced Fluorescence.* PhD thesis, University of Strathclyde, 2015.

[43] D. E. Heard, J. B. Jeffries, G. P. Smith, and D. R. Crosley, “LIF measurements in methane/air flames of radicals important in prompt-NO formation,” *Combustion and Flame*, vol. 88, pp. 137–148, feb 1992.

[44] R. L. Vander Wal, “LIF-LII measurements in a turbulent gas-jet flame,” *Experiments in Fluids*, vol. 23, pp. 281–287, aug 1997.

[45] T. Shimizu, H. Nakamura, T. Tezuka, S. Hasegawa, and K. Maruta, “OH and CH ₂ O Laser-Induced Fluorescence Measurements for Hydrogen Flames and Methane, <i>n</i> -Butane, and Dimethyl Ether Weak Flames in a Micro Flow Reactor with a Controlled Temperature Profile,” *Energy & Fuels*, p. acs.energyfuels.6b02325, jan 2017.

[46] R. Hadef, K. P. Geigle, W. Meier, and M. Aigner, “Soot characterization with laser-induced incandescence applied to a laminar premixed ethyleneair flame,” *International Journal of Thermal Sciences*, vol. 49, no. 8, pp. 1457–1467, 2010.

[47] A. C. Eckbreth and R. J. Hall, “CARS thermometry in a sooting flame,” *Combustion and Flame*, vol. 36, pp. 87–98, 1979.

[48] J. M. Brown, *Molecular spectroscopy.* Oxford University Press, 1998.

[49] B. P. Straughan and S. Walker, *No Title.* Chapman and Hall Ltd., 1976.

[50] J. M. J. M. Hollas, *Modern spectroscopy.* Wiley, 2004.

[51] L. Rothman, I. Gordon, a. Barbe, D. Benner, P. Bernath, M. Birk, V. Boudon, L. Brown, a. Campargue, J.-P. Champion, K. Chance, L. Coudert, V. Dana, V. Devi, S. Fally, J.-M. Flaud, R. Gamache, a. Goldman, D. Jacquemart, I. Kleiner, N. Lacome, W. Lafferty, J.-Y. Mandin, S. Massie, S. Mikhailenko, C. Miller, N. Moazzen-Ahmadi, O. Naumenko, a.V. Nikitin, J. Orphal, V. Perevalov, a. Perrin, a. Predoi-Cross, C. Rinsland, M. Rotger, M. Šimečková, M. Smith, K. Sung, S. Tashkun, J. Tennyson, R. Toth, a.C. Vandaele, and J. Vander Auwera, “The HITRAN 2008 molecular spectroscopic database,” *Journal of*

Quantitative Spectroscopy and Radiative Transfer, vol. 110, pp. 533–572, jun 2009.

[52] J. Tennyson, Y. Ponomarev, V. Perevalov, L. Rothman, I. Gordon, R. Barber, H. Dothe, R. Gamache, A. Goldman, V. Perevalov, S. Tashkun, and J. Tennyson, "HITEMP, the high-temperature molecular spectroscopic database," *Journal of Quantitative Spectroscopy and Radiative Transfer*, vol. 111, no. 15, pp. 2139–2150, 2010.

[53] X. Zhou, *DIODE-LASER ABSORPTION SENSORS FOR COMBUSTION CONTROL*. PhD thesis, Stanford University, 2005.

[54] A. McLean, C. Mitchell, and D. Swanston, "Implementation of an efficient analytical approximation to the Voigt function for photoemission lineshape analysis," *Journal of Electron Spectroscopy and Related Phenomena*, vol. 69, pp. 125–132, sep 1994.

[55] S. W. M. Klein and T. K. U. Riedel, "In situ TDLAS measurement of absolute acetylene concentration profiles in a non-premixed laminar counter-flow flame," pp. 585–589, 2012.

[56] K. K. Lehmann, G. Berden, and R. Engeln, "An Introduction to Cavity Ring-Down Spectroscopy," in *Cavity Ring-Down Spectroscopy*, pp. 1–26, John Wiley & Sons, Ltd, 2009.

[57] A. O'Keefe and D. A. G. Deacon, "Cavity ring-down optical spectrometer for absorption measurements using pulsed laser sources," *Review of Scientific Instruments*, vol. 59, no. 12, p. 2544, 1988.

[58] J. M. Herbelin, J. A. McKay, M. A. Kwok, R. H. Ueunten, D. S. Urevig, D. J. Spencer, and D. J. Benard, "Sensitive measurement of photon lifetime and true reflectances in an optical cavity by a phase-shift method," *Applied Optics*, vol. 19, p. 144, jan 1980.

[59] T. Laurila, I. S. Burns, J. Hult, J. H. Miller, and C. F. Kaminski, "A calibration method for broad-bandwidth cavity enhanced absorption spectroscopy performed with supercontinuum radiation," *Applied Physics B*, vol. 102, pp. 271–278, feb 2011.

[60] A. O'Keefe, J. J. Scherer, and J. B. Paul, "cw Integrated cavity output spectroscopy," *Chemical Physics Letters*, vol. 307, no. 5, pp. 343–349, 1999.

[61] D. S. Baer, J. B. Paul, M. Gupta, and A. O'Keefe, "Sensitive absorption measurements in the near-infrared region using off-axis integrated cavity output spectroscopy," p. 167, International Society for Optics and Photonics, sep 2002.

[62] *Mathematical Description of Premixed Laminar Flat Flames*, pp. 29–38. Berlin, Heidelberg: Springer Berlin Heidelberg, 2006.

[63] R. Barlow, A. Karpetis, J. Frank, and J.-Y. Chen, "Scalar profiles and NO formation in laminar opposed-flow partially premixed methane/air flames," *Combustion and Flame*, vol. 127, no. 3, pp. 2102–2118, 2001.

[64] S. Cheskis, “Quantitative measurements of absolute concentrations of intermediate species in flames,” *Progress in Energy and Combustion Science*, vol. 25, no. 3, pp. 233–252, 1999.

[65] N. Kastelis and E. Zervas, “Analysis of flat burners used to study gaseous pollutants emitted from combustion of hydrocarbons,”

[66] Y. YAN, T. QIU, G. LU, M. Hossain, G. Gilabert, and S. LIU, “Recent Advances in Flame Tomography,” *Chinese Journal of Chemical Engineering*, vol. 20, pp. 389–399, apr 2012.

[67] T. U. of Adelaide, “International Sooting Flame (ISF) Workshop,” 2015.

[68] F. MIGLIORINI, S. DEIULIIS, F. CIGNOLI, and G. ZIZAK, “How flat is the rich premixed flame produced by your McKenna burner?,” *Combustion and Flame*, vol. 153, pp. 384–393, may 2008.

[69] J. Dunn, *Investigation of Premixed Sooting Flames by Combined Laser Induced Incandescence and Laser Induced Fluorescence.* PhD thesis, 2014.

[70] D. R. Snelling, K. A. Thomson, G. J. Smallwood, and Ö. L. Gülder, “Two-dimensional imaging of soot volume fraction in laminar diffusion flames,” *Applied Optics*, vol. 38, p. 2478, apr 1999.

[71] H. Guo, J. A. Castillo, and P. B. Sunderland, “Digital camera measurements of soot temperature and soot volume fraction in axisymmetric flames,” *Applied Optics*, vol. 52, p. 8040, nov 2013.

[72] L. Zheng and Y. Zhang, “High Speed Digital Imaging for Flame Studies: Potentials and Limitations,” *Energy Procedia*, vol. 66, pp. 237–240, 2015.

[73] R. C. Johnson, “The Structure and Origin of the Swan Band Spectrum of Carbon,” *Philosophical Transactions of the Royal Society of London A: Mathematical, Physical and Engineering Sciences*, vol. 226, no. 636-646, 1927.

[74] M. Klassen, Y. Sivathanu, and J. Gore, “Simultaneous emission absorption measurements in toluene-fueled pool flames: Mean and RMS Properties,” *Combustion and Flame*, vol. 90, no. 1, pp. 34–44, 1992.

[75] K. A. Thomson, Ö. L. Gülder, E. J. Weckman, R. A. Fraser, G. J. Smallwood, and D. R. Snelling, “Soot concentration and temperature measurements in co-annular, nonpremixed CH4/air laminar flames at pressures up to 4 MPa,” *Combustion and Flame*, vol. 140, no. 3, pp. 222–232, 2005.

[76] F. Cignoli, S. De Iuliis, V. Manta, and G. Zizak, “Two-dimensional two-wavelength emission technique for soot diagnostics,” *Applied Optics*, vol. 40, p. 5370, oct 2001.

[77] S. Schraml, S. Dankers, K. Bader, S. Will, and A. Leipertz, “Soot temperature measurements and implications for time-resolved laser-induced incandescence (TIRE-LII),” *Combustion and Flame*, vol. 120, no. 4, pp. 439–450, 2000.

[78] Z.-G. Yuan, “The Filtered Abel Transform and Its Application in Combustion

Diagnostics,” 2003.

[79] Edwards and J.B., “Combustion: the formation and emission of trace species,” 1977.

[80] A. C. Eckbreth, *Laser diagnostics for combustion temperature and species.* Gordon and Breach Publishers, 1996.

[81] A. Elia, P. M. Lugarà, C. Di Franco, and V. Spagnolo, “Photoacoustic techniques for trace gas sensing based on semiconductor laser sources.,” *Sensors (Basel, Switzerland)*, vol. 9, pp. 9616–28, jan 2009.

[82] A. Petzold and R. Niessner, “Photoacoustic soot sensor for in-situ black carbon monitoring,” *Applied Physics B Laser and Optics*, vol. 63, pp. 191–197, aug 1996.

[83] A. G. Bell, “On the production and reproduction of sound by light,” *American Journal of Science*, vol. s3-20, pp. 305–324, oct 1880.

[84] R. W. Terhune and J. E. Anderson, “Spectrophone measurements of the absorption of visible light by aerosols in the atmosphere,” *Optics Letters*, vol. 1, p. 70, aug 1977.

[85] C. Schulz, B. Kock, M. Hofmann, H. Michelsen, S. Will, B. Bougie, R. Suntz, and G. Smallwood, “Laser-induced incandescence: recent trends and current questions,” *Applied Physics B*, vol. 83, pp. 333–354, may 2006.

[86] F. Migliorini, K. A. Thomson, and G. J. Smallwood, “Investigation of optical properties of aging soot,” *Applied Physics B*, vol. 104, pp. 273–283, aug 2011.

[87] H. Bladh, N.-E. Olofsson, T. Mouton, J. Simonsson, X. Mercier, A. Faccinetto, P.-E. Bengtsson, and P. Desgroux, “Probing the smallest soot particles in low-sooting premixed flames using laser-induced incandescence,” *Proceedings of the Combustion Institute*, vol. 35, no. 2, pp. 1843–1850, 2015.

[88] S. Ezekiel and R. Weiss, “Laser-Induced Fluorescence in a Molecular Beam of Iodine,” *Physical Review Letters*, vol. 20, pp. 91–93, jan 1968.

[89] J. J. Nikkari, J. M. Di Iorio, and M. J. Thomson, “In Situ Combustion Measurements of CO, H_2O, and Temperature with a 1.58-μm Diode Laser and Two-Tone Frequency Modulation,” *Applied Optics*, vol. 41, p. 446, jan 2002.

[90] J. Hodgkinson and R. P. Tatam, “Optical gas sensing: a review,” *Measurement Science and Technology*, vol. 24, p. 012004, jan 2013.

[91] “From pulsed to continuous wave cavity ring-down spectroscopy.”

[92] B. E. A. Saleh and M. C. Teich, *Fundamentals of Photonics.* Wiley Series in Pure and Applied Optics, New York, USA: John Wiley & Sons, Inc., aug 1991.

[93] M. A. Porras, J. Alda, and E. Bernabeu, “Complex beam parameter and ABCD law for non-Gaussian and nonspherical light beams.,” *Applied optics*, vol. 31, pp. 6389–402, oct 1992.

[94] M. Vogel, “Principles of Lasers, 5th edn., by O. Svelto,” *Contemporary Physics*,

vol. 53, p. 173, mar 2012.

[95] H. Kogelnik and T. Li, "Laser beams and resonators.," *Applied optics*, vol. 5, pp. 1550–67, oct 1966.

[96] H. Huang and K. Lehmann, "Noise in cavity ring-down spectroscopy caused by transverse mode coupling," *Optics Express*, vol. 15, p. 8745, jul 2007.

[97] D.-H. Lee, Y. Yoon, B. Kim, J. Lee, Y. Yoo, and J. Hahn, "Optimization of the mode matching in pulsed cavity ringdown spectroscopy by monitoring non-degenerate transverse mode beating," *Applied Physics B: Lasers and Optics*, vol. 74, pp. 435–440, apr 2002.

[98] J. H. van Helden, R. Peverall, and G. A. D. Ritchie, "Cavity Enhanced Techniques Using Continuous Wave Lasers," in *Cavity Ring-Down Spectroscopy*, pp. 27–56, John Wiley & Sons, Ltd, 2009.

[99] B. J. Orr and Y. He, "Rapidly swept continuous-wave cavity-ringdown spectroscopy," *Chemical Physics Letters*, vol. 512, pp. 1–20, aug 2011.

[100] H. Huang and K. K. Lehmann, "CW cavity ring-down spectroscopy (CRDS) with a semiconductor optical amplifier as intensity modulator," *Chemical Physics Letters*, vol. 463, pp. 246–250, sep 2008.

[101] J. H. Miller, A. R. Awtry, M. E. Moses, A. D. Jewell, and E. L. Wilson, "Measurements of hydrogen cyanide and its chemical production rate in a laminar methane/air, non-premixed flame using cw cavity ringdown spectroscopy," *Proceedings of the Combustion Institute*, vol. 29, no. 2, pp. 2203–2209, 2002.

[102] K. Duffin, *Wavelength modulation spectroscopy with tunable diode lasers : a calibration-free approach to the recovery of absolute gas absorption line-shapes*. PhD thesis, University of Strathclyde, 2007.

[103] W. Johnstone, A. J. McGettrick, K. Duffin, A. Cheung, and G. Stewart, "Tunable Diode Laser Spectroscopy for Industrial Process Applications: System Characterization in Conventional and New Approaches," *IEEE Sensors Journal*, vol. 8, pp. 1079–1088, jul 2008.

[104] S. Gersen, A. Mokhov, and H. Levinsky, "Extractive probe/TDLAS measurements of acetylene in atmospheric-pressure fuel-rich premixed methane/air flames," *Combustion and Flame*, vol. 143, pp. 333–336, nov 2005.

[105] D. R. Snelling, R. A. Sawchuk, G. J. Smallwood, and K. Thomson, "Measurement of soot concentration and bulk fluid temperature and velocity using modulated laser-induced incandescence," *Applied Physics B*, vol. 119, pp. 697–707, jun 2015.

[106] H. Bladh, N.-E. Olofsson, T. Mouton, J. Simonsson, X. Mercier, A. Faccinetto, P.-E. Bengtsson, and P. Desgroux, "Probing the smallest soot particles in low-sooting premixed flames using laser-induced incandescence," *Proceedings of the Combustion Institute*, vol. 35, no. 2, pp. 1843–1850, 2015.

Publications

Journal publications

Humphries, G. S., Dunn, J., Hossain, M. M., Lengden, M., Burns, I. S., & Black, J. D. (2015). *A simple photoacoustic method for the in situ study of soot distribution in flames.* Applied Physics B, 119(4), 709715.

Humphries, G. S., Burns, I. S., & Lengden, M. (2015). *Application of Continuous-Wave Cavity Ring-Down Spectroscopy to Laminar Flames.* IEEE Photonics Journal, 8(1), 110.

Conference publciations

(Poster) Humphries GS, Lengden M, & Burns IS. *Application of Cavity Ring-Down Spectroscopy to Laminar Flames* Gordon Research Conference: Laser Diagnostics in Combustion. August 9-14, 2015

(Poster) Humphries GS, Dunn J, Hossain MM, Lengden M, Black J, & Burns IS *A Photoacoustic Detection Scheme for Soot Measurement* Gordon Research Conference: Laser Diagnostics in Combustion. August 9-14, 2015

(Presentation) Humphries GS, Dunn J, Hossain MM, Lengden M, Black J, & Burns IS *Novel Diode Laser Techniques for Trace Species and Particulate Measurement: In Situ cw-CRDS and Photoacoustic Soot Detection* Gordon Research Seminar: Laser Diagnostics in Combustion. August 8-9, 2015.

(Paper) Humphries GS, Lengden M, Burns IS, & Black J *Novel in-situ optical measurement techniques for combustion applications* OSA Advanced Photonics. 27 June1 July 2015.

(Paper) Lea-Langton AR, Atiku FA, Bartle KD, Jones JM, Pourkashanian M, Williams A, Burns I, & Humphries G. *Mechanism of the formation of smoke from the combustion of wood.* 9th Mediterranean Combustion Symposium. June 7-11 2015.

(Poster) Humphries GS, Lengden M, & Burns IS *Development of a continuous-wave cavity ring-down spectrometer for the study of acetylene in sooting flames* 35th International Symposium on Combustion. August 3-8 2014.

(Poster) Black J, Humphries GS, Dunn J, Lengden M, & Burns IS *Development of a Photoacoustic Detection Scheme for Soot Measurement* 35th International Symposium on Combustion. August 3-8 2014.

(Presentation) Black J, Humphries GS, Dunn J, Lengden M, & Burns IS *Photoacoustic Soot Measurement: Comparison with LII* 6th international Workshop and Meeting on Laser-Induced Incandescence. June 8-11 2014.

(Presentation) Humphries GS, Lengden M, & Burns IS *Development of a continuous-wave cavity ring-down spectrometer for the study of acetylene in sooting flames* Joint meeting of the British and Scandinavian-Nordic Sections of the Combustion Institute.

March 27-28 2014.

(Poster) Humphries GS, Burns IS, & Lengden M *Development of a continuous wave cavity ring down spectrometer for combustion diagnostics* FLAIR. May 5-9 2014.